

Department of Precision and Microsystems Engineering

Rider Control Identification in Bicycling

P.D.L. de Lange

Report no : EM 11.040
Coach : Dr. A.L. Schwab
Professor : Prof. Dr. D.J. Rixen
Specialisation : Engineering Mechanics
Type of report : Thesis
Date : 2 December 2011



Rider Control Identification in Bicycling

A preliminary analysis

P.D.L. de Lange

Master of Science Thesis

Rider Control Identification in Bicycling

A preliminary analysis

MASTER OF SCIENCE THESIS

For the degree of Master of Science in Precision and Microsystems
Engineering at Delft University of Technology

P.D.L. de Lange

November 16, 2011

Faculty of Mechanical, Maritime and Materials Engineering (3mE) · Delft University of
Technology



Copyright © Faculty of Mechanical Engineering (ME)
All rights reserved.

Abstract

Following in the wake of the increased bicycle popularity, bicycle research arose in the late 19th century. Early research, regarding the dynamic behavior of an uncontrolled bicycle, resulted in the Carvallo (1899) and more general Whipple (1899) model. In the past years, extensive research has been done to validate these uncontrolled bicycle models. However, the bicycle is normally accompanied by a rider, for which the combined rider/bicycle dynamics are less understood. The goal of this research is to identify the active rider contribution during stabilization tasks in bicycling. This knowledge may be used to develop better and more user-specific bicycles in the future.

The equations governing the combined rider/bicycle system subjected to an external disturbance are derived in the first chapter. Here, the bicycle is modeled according to the linearized Whipple model, where the passive rider dynamics are already included. After a process of trial and error, a flexible rider model structure is chosen, which interacts with the bicycle through steering torque. To be more specific, the rider model allows for proportional, integral, derivative and 2nd order derivative linear feedback on both the roll and steering angle and is limited by activation dynamics and transport delays.

An experimental dataset from our colleagues of the UC Davis is used to obtain a preliminary rider model. First a non parametric FIR model is derived, which serves as a platform for subsequent parametric modeling. The parametric models are fitted by minimizing the sum of errors squared between the non parametric and parametric steering angle responses, resulting in a set of optimized parameters. The resulting parametric model, which consists of 8 parameters, accounts for 97% of the variance of the non parametric model output. The parameter may be reduced from 8 up to 4 parameters, while the variance accounted for only lowers with 3%.

The following important observations are made from the parametric model results:

- The steer into the fall principle is observable in the positive roll angle and rate feedback for all measurements.
- The roll angle, roll rate, steering rate and integral action are the key contributors and cannot be removed without causing a major drop of the VAF.

- The integrative steering action controls the heading by applying counter steering.

The identification results are used to set up a future frequency domain rider identification experiment. The experiment should be performed at forward velocities of 2, 3, . . . , 7 m/s, since the dynamic behavior is velocity dependent. A disturbance input signal has also been designed, and should be applied as a generalized roll torque to the system. A randomly appearing multisine input signal is created, with a bandwidth of 0.2 to 4 Hz, and where the input power is scaled such that its absolute value does not exceed the 40 Nm. The measurement time is set to 163.84 s at a sampling frequency of 200 Hz. A simulation study indicates that the parameters can be estimated with an error of less than 3% relative to the true parameters.

Next, a number of perturbator designs are presented. The goal of these designs is to apply a desired perturbation spectrum as a generalized roll torque to the rider/bicycle configuration. 4 perturbator designs are presented, namely; the swing, sliding mass, lateral accelerator and simple rope perturbator. The designs are evaluated by the following criteria; active system contribution, passive system contribution, rider interaction, implementability and cost. Here, the sliding mass perturbator shows the best overall score and is recommended for further development.

Apart from the rider identification, some errors in bicycle literature were encountered. To be more specific, the models presented in van Lunteren and Stassen (1970) and Stassen and Lunteren (1973) were found to contain sign errors. After correcting for these sign errors, the models were implemented in Matlab, but were found to be unstable.

Table of Contents

Preface	ix
1 Introduction	1
2 System Description	3
2-1 Bicycle equations	3
2-1-1 Bicycle equations	3
2-1-2 Uncontrolled dynamic behavior	5
2-1-3 Bicycle stability	5
2-1-4 Passive rider	7
2-1-5 Rider lean	7
2-1-6 Control forms	8
2-1-7 State Space representation	8
2-1-8 Transfer function representation	9
2-1-9 Summary	9
2-2 Rider	9
2-2-1 Input/output structure	10
2-2-2 Rider model structure	11
2-2-3 Co-contraction	13
2-2-4 Summary	13
2-3 External input	14
2-4 General control description	14
2-4-1 Block definitions	14
2-4-2 Closed loop transfer function	15
2-4-3 Summary	16

3	Experimental Data Analysis	17
3-1	Experiment description	17
3-1-1	Data description	19
3-1-2	Bicycle and passive rider measurements	19
3-2	Summary	22
4	System Identification	23
4-1	Theory	23
4-1-1	System description	24
4-1-2	Time domain expressions	24
4-1-3	Frequency domain expressions	25
4-1-4	Nonparametric Linear models	26
4-1-5	Parametric linear models	27
4-1-6	Model evaluation	28
4-2	Application	29
4-2-1	Non Parametric Modeling	29
4-2-2	Parametric Modeling	35
4-3	Analysis	48
4-3-1	Eigenvalue analysis	48
4-3-2	Observations	48
4-3-3	Non-linear scaling check	50
4-4	Summary	51
5	Experiment Design	53
5-1	Goal	53
5-2	Closed loop identification methods	54
5-3	Frequency domain identification method	55
5-4	Measurement settings	55
5-5	Input signal design	56
5-5-1	Random multi sine	57
5-5-2	Spatial excitation	57
5-5-3	Spectral excitation	57
5-5-4	Input power	58
5-5-5	Input signal design	60
5-6	Measurement Considerations	60
5-6-1	A priori measurements	60
5-6-2	Environment	60
5-6-3	Task instruction	60
5-6-4	Number of trials and subjects	62
5-6-5	Detection of non linearities	62
5-7	Expected parameter accuracy	63
5-8	Simulation	63
5-9	Summary	67

6	Perturbator Design	69
6-1	Design of a swing perturbator	71
6-1-1	Equations of Motion	71
6-1-2	Analysis	72
6-1-3	Summary	75
6-2	Design of a sliding mass perturbator	77
6-2-1	Equations of Motion	77
6-2-2	Analysis	78
6-2-3	Summary	79
6-3	Lateral accelerator	81
6-3-1	Equations of Motion	81
6-3-2	Analysis	82
6-3-3	Summary	84
6-4	Design of a rope perturbator	84
6-4-1	Analysis	85
6-4-2	Summary	85
6-5	Comparison	85
6-5-1	Overview of example calculations	86
6-5-2	Design criteria	86
6-5-3	Comparison table	88
6-6	Summary	88
7	Discussion	89
7-1	General control description	89
7-2	Experimental Results	89
7-3	Parameter Estimation	90
7-4	Parametric Results	92
7-5	Experiment Design	93
7-6	Perturbator Design	93
8	Conclusions and Recommendations	95
8-1	Conclusions	95
8-1-1	Literature analysis	95
8-1-2	System description	96
8-1-3	Rider control	96
8-1-4	Experiment Design	97
8-1-5	Perturbator design	97
8-2	Recommendations	97

A	Additional rider model analysis	101
A-1	Lunteren and Stassen controller	101
A-1-1	Control model	101
A-1-2	Reformulation of the rider model	106
A-1-3	Conclusions	108
A-2	LQR controller	108
A-2-1	Implementation	109
A-2-2	Experimental Results	110
B	Input signal design	111
B-1	White noise	111
B-2	Sine sweep	112
B-3	Random phase multisine	112
B-4	Crested multisine	112
B-5	Comparison	113
B-6	Results	113
C	Analysis of a Double Inverted Pendulum on a Cart	115
C-1	Accelerating in the fall	116
C-2	Lean action analysis	117
C-3	Conclusions	118
D	Parameter covariance	119
D-1	Defintions	119
D-2	Covariance definition	119
D-3	Matlab output defintions	120
D-4	Expressing covariance in terms of Matlab output	120
D-4-1	Hessian method	121
D-4-2	Jacobian method	122
E	The Human Controller	123
E-1	Neuromuscular system	123
E-1-1	Sensory system	123
E-1-2	Central nervous system	126
E-1-3	Muscular system	126
E-2	Control methods	127
E-2-1	Compensatory control	127
E-2-2	Pursuit	127
E-2-3	Precognitive control	127
E-3	Summary	128

F Bicycle Simulator	129
F-1 Setup	129
F-2 Software	129
F-2-1 Setting up the Simulink model	130
F-2-2 3D bicycle visualization	130
F-2-3 Compilation to real time C-code	130
F-2-4 Matlab GUI	131
F-3 Results	131
F-4 Discussion	132
F-5 Conclusion	132
Bibliography	133

Preface

The MSc thesis that is lying before you is the result of 7 months of fruitful bicycle research, performed at the Delft University of Technology, 3ME. As with every project, the work and writing of my research has gone through of ups and downs. Especially in the beginning, where it was difficult to get the project start rolling, since months of labour were spent on simulation studies with little result. Fortunately, our friends and colleagues of the UC Davis were more than willing to share their experimental data, after which our own research moved on very rapidly. Without this data, we would be months or maybe even years behind. So again, thanks for sharing, we owe you one guys!

There are numerous people who supported me in various ways throughout my graduation, for which I like to thank a number of people in particular. First, I'd like to thank my supervisors Arend Schwab and Riender Happee. I think we formed an excellent multidisciplinary team, where I experienced our numerous meetings to be of great value. Special thanks to Arend, since it was a pleasure to work with him in both a professional and personal sense. I also like to thank Daniel Rixen, Erwin de Vlugt, Matteo Corno and Jodi Kooijman for their valuable support.

I also like to thank Jason Moore, Luke Dale Peterson, Ron Hess and Mont Hubbard of the UC Davis, where I did my internship in bicycle research prior to my graduation. This was an unforgettable experience, where I particularly like to thank Jason Moore for all the hospitality he provided.

Besides working on my thesis I enjoyed many coffee breaks I've shared with fellow students. Here, I'd like to thank the illustrious mister P. Li, who kept us refuelled at all time.

To my parents; it was a long but scenic road, which has enriched me greatly, both personally and in my development as a future engineer. All along my journey along this winding road, you have always been supportive and encouraging. Having experienced such an active interest is indeed a great privilege. Thank you.

Chapter 1

Introduction

The bicycle originates from the 19th century and has evolved over the years to the variety of bicycles we know today. Clearly, the bicycle has become a very popular means of transport. This popularity is expected to last, because of the ongoing need for consumer mobility.

Following in the wake of the increased bicycle popularity, bicycle research arose in the late 19th century. Early research, regarding the dynamic behavior of an uncontrolled bicycle, resulted in the Carvallo (1899) and more general Whipple (1899) model. The latter is recently reformulated into the canonical Whipple model by Meijaard et al. (2007), which is accompanied by experimental results from Kooijman et al. (2008) and serves as a benchmark for future bicycle research.

However, the Whipple model only describes the uncontrolled behavior of a bicycle, whereas the bicycle normally is accompanied by a rider. The combined bicycle/rider dynamics are less understood, for which the rider identification forms the main subject of this thesis. If this succeeds, we will have the complete picture consisting of both rider and bicycle. This deeper knowledge can be used to design user-specific bicycles. For example; elder people may find a need for a more stable bicycle. However, before all of this, the following research question needs to be answered:

- How does the rider control the bicycle? -

This is still a very broad question, for which we need to introduce some additional boundaries. Both Weir (1972) and Doyle (1988) describe the inner loop roll stabilization to be the essential bicycle skill, which serves as a base for high level control actions such as cornering, obstacle avoidance, etc. In addition, Weir also describes the steering torque to be the main control method. Therefore, we will limit ourselves to the case of roll stabilization through rider enforced steering torque, where the upper body movement is constrained.

This thesis starts of with a general control description, describing the combined bicycle/rider dynamics and also how an external force can be incorporated within these equations. Next, an experimental dataset is presented in chapter 3, where the combined rider/bicycle system

subjected to an external disturbance is measured. This dataset allows for system identification, which is the subject of chapter 4, where a preliminary model of the human rider action is obtained. This model is then used for designing future experiments, which is described in chapter 5. Here, the measurement settings and input signal are designed for a frequency domain experiment. Next, a perturbator is designed in chapter 6, which should be capable of physically realizing the input signal. An overall discussion is given in chapter 7, which is followed by the conclusions and recommendations (chapter 8). The thesis ends with a number of appendices, which provides some supplementary material.

System Description

In this chapter we will set up a frame work which will form the base for subsequent analysis. First the bicycle equations are introduced and converted to state space description. Secondly a frame work for potential rider models is introduced, for which a number of parametric candidate models will be discussed in more detail. Finally the two separate models are combined into the general control description, which allows for easy simulation, manipulation and identification of the system.

2-1 Bicycle equations

In this section a model for the bicycle will be presented and discussed. The model describes the dynamic behavior of the uncontrolled bicycle, which is described in more detail in Meijaard et al. (2007). Here, the following model assumptions are made:

- rigid bodies
- symmetric about vertical plane
- knife-edge wheels
- point contact, no side slip
- flat level road
- no friction or propulsion

The bicycle configuration with is shown in figure 2-1.

2-1-1 Bicycle equations

The linearized Whipple bicycle equations are known to give an accurate description of the bicycle dynamics (Kooijman et al., 2008). The linearization also results in a first-order decoupling of the forward dynamics and the lateral (roll and steer) dynamics.

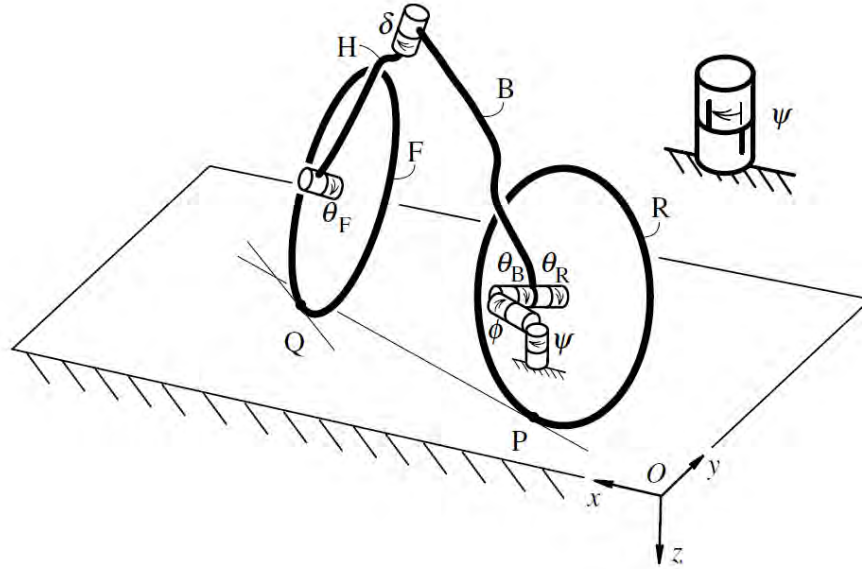


Figure 2-1: Configuration of the bicycle and dynamic variables. The configuration space is spanned by the following 7 variables; x and y -coordinates of the rear contact point, yaw angle ψ , frame pitch angle θ_B , roll angle ϕ , steering angle δ and rear wheel pitch angle θ_R . Taken over from Meijaard et al. (2007).

First linear equation

The first equation describes the change in angular rear wheel rate $\dot{\theta}_R$;

$$\left[r_R^2 m_T + I_{Ryy} + \left(\frac{r_R}{r_F} \right)^2 I_{Fyy} \right] \ddot{\theta}_R = T_{\theta_R}, \quad (2-1)$$

with; total bicycle mass m_T , rear wheel radius r_R , front wheel radius r_F , axial rear wheel moment of inertia I_{Ryy} , axial front wheel moment of inertia I_{Fyy} and propulsive rear wheel torque T_{θ_R} . The velocity of the bicycle is given by: $v = -r_R \dot{\theta}_R$. From the equations we observe that the velocity remains constant in the absence of a rear wheel torque. This is a nice property, since the roll and steer equations change as a function of the forward velocity, which will be discussed next.

Roll and steer equations

Next the linearized roll and steer equations are given by:

$$\mathbf{M}\ddot{\mathbf{q}} + v\mathbf{C}_1\dot{\mathbf{q}} + [g\mathbf{K}_0 + v^2\mathbf{K}_2] \mathbf{q} = \mathbf{f}, \quad (2-2)$$

where $\mathbf{q} = [\phi, \delta]^T$ and $\mathbf{f} = [T_\phi, T_\delta]^T$. Here the equations are written as explicit functions of the forward velocity v and gravity g . The components of the system matrices are determined by the physical parameters of the bicycle, which are omitted here, but can be found in Meijaard et al. (2007). The roll and steer dynamics can be excited through roll (T_ϕ) and steer (T_δ) torque.

Heading and real wheel contact location functions

Optionally, the derivatives of the heading ψ and real wheel contact coordinates x_p and y_p can be expressed in terms of the state variables as:

$$\dot{\psi} = \frac{v\delta + c\dot{\delta}}{w} \cos \lambda, \quad (2-3)$$

$$\dot{x}_p = v \cos \psi, \quad (2-4)$$

$$\dot{y}_p = v \sin \psi, \quad (2-5)$$

where c is the trail distance and w the wheel base. Notice that these functions do not appear in the forward and lateral equations of motion. This is due to the translational symmetry of the system, e.g. the system is invariant of global translation and orientation (heading). The actual heading and position expressions are non-linear can be obtained through numerical integration of equations 2-3, 2-4 and 2-5.

2-1-2 Uncontrolled dynamic behavior

The uncontrolled dynamic behavior of the bicycle ($\mathbf{f} = \mathbf{0}$) is a function of the physical parameters, gravitational acceleration and forward velocity of the bicycle. The dynamics of bicycles are best understood by calculating and analyzing the eigenvalues and vectors of the system matrices. By doing so, the system dynamics are decoupled in the time domain (eigenvalues) and spatial domain (eigenvectors). A good description of the uncontrolled bicycle dynamics for the benchmark case is given by Meijaard et al. (2007). Here three important eigenmodes are identified; the castering, capsize and weave mode, of which the latter two are most interesting concerning bicycle stability. The eigenvalues of the benchmark bicycle are shown in figure 2-2 and indicate stability for a certain forward speedrange; $v_w < v < v_c$.

2-1-3 Bicycle stability

The problem of stabilizing the bicycle is very similar to stabilizing an inverted pendulum on a cart. Whenever the pendulum starts to fall over, the cart needs to accelerate in the direction of the fall in order to restabilize the system. In a passive (e.g. non actuated) inverted pendulum on a cart system, there is no passive mechanism of accelerating in the fall and thus the uncontrolled system is unstable. For the case of the uncontrolled bicycle, these mechanisms do exist, as will be explained next.

Let's assume the lateral acceleration of the total center of mass is equal to the rear wheel lateral acceleration. This lateral acceleration relative to the bicycle (denoted by the apostrophe) is given by:

$$\ddot{y}_p' = v\dot{\psi} = \frac{v^2}{w} \delta \cos \lambda + \frac{vc}{w} \dot{\delta} \cos \lambda. \quad (2-6)$$

The first term, which is proportional to the steering angle, is the dominant term at higher forward velocity ($v > 1$ m/s). From this equation, we observe that the bicycle can be stabilized by steering into the direction of fall. By doing so, the support line (PQ) is being moved back under the total center of mass, thereby stabilizing the system.

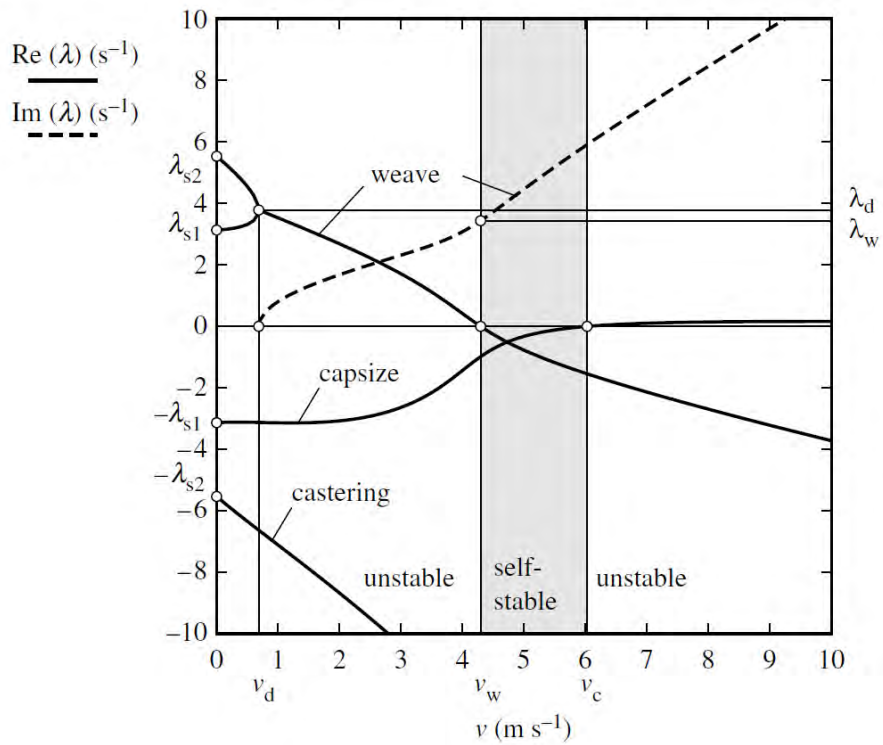


Figure 2-2: Eigenvalues λ of the benchmark bicycle plotted as a function of the forward velocity v . The uncontrolled bicycle is stable between the weave v_w and capsize v_c speed. At lower velocities the oscillatory weave mode becomes unstable, whereas at higher velocity the capsize mode becomes unstable. The castering mode is stable across the entire speed range of $0 < v < 10$ m/s². Reprinted from Meijaard et al. (2007).

There are three possible passive mechanisms which stabilize the bicycle by coupling falling by creating a coupling between falling (rolling) and steering. The effects produced by these mechanisms are called; caster, gyroscopic and mass distribution effects. The latter was recently demonstrated by Kooijman et al. (2011), where it is shown that a bicycle without gyroscopic and caster effects can be stabilized by proper mass distribution.

2-1-4 Passive rider

This section describes how the passive (lumbered) rider characteristics interact with the system. Here the rider is not completely passive, but uses some level of muscle activation to maintain a certain (passive) posture on the bicycle. The presence of such a passive rider adds extra inertia to the system, affecting the dynamics of the total system (rider + bicycle). There are several models to include the passive rider properties within the system dynamics. Two of these methods will be described in this section.

Rigid rider

The dynamics of the bicycle can be extended by adding a rigid rider to the equations. The simplest way is to model the rider as a rigid body which is rigidly connected to the frame. By doing so, the rider is effectively modeled as a hands free rigid rider, introducing extra inertia terms (mainly affecting roll dynamics) to the equations.

Passive rider

A more sophisticated way of modeling passive hands-on rider models to the bicycle equations is given by Schwab et al. (2011). Here the riders upper body movement is determined kinematically as a function of the configuration of the bicycle. By doing so the configuration space remains the same, but the introduction of a passive rider does introduce additional inertia and stiffness to the system. The main body of the rider adds to the roll inertia terms of the system, whereas the inertia of the arms mainly attributes to the inertia corresponding to steering. Two distinctive rider positions are identified; forward upper body position with bend arms or upright upper body position with stretched arms (figure 2-3). It is shown that adding a hands-on passive rider model can dramatically change the eigenvalues in comparison with the rigid rider model.

2-1-5 Rider lean

The rigid and passive rider models do affect the dynamics, but not the configuration space of the bicycle model. In other words, the structure of the equations stay the same, but the coefficients change. These rigid and passive rider models do not allow for rider lean, while in reality it is possible to control the bicycle by upperbody leaning action. This rider lean action can be modelled by introducing an extra degree of freedom in the bicycle equations, namely rider lean which will be indicated by γ . This degree of freedom is modelled as a rotational joint near the seat post, with the axis of rotation facing forwards (x -direction). As a result, the rider lean also introduces a corresponding lean torque T_γ . A detailed description

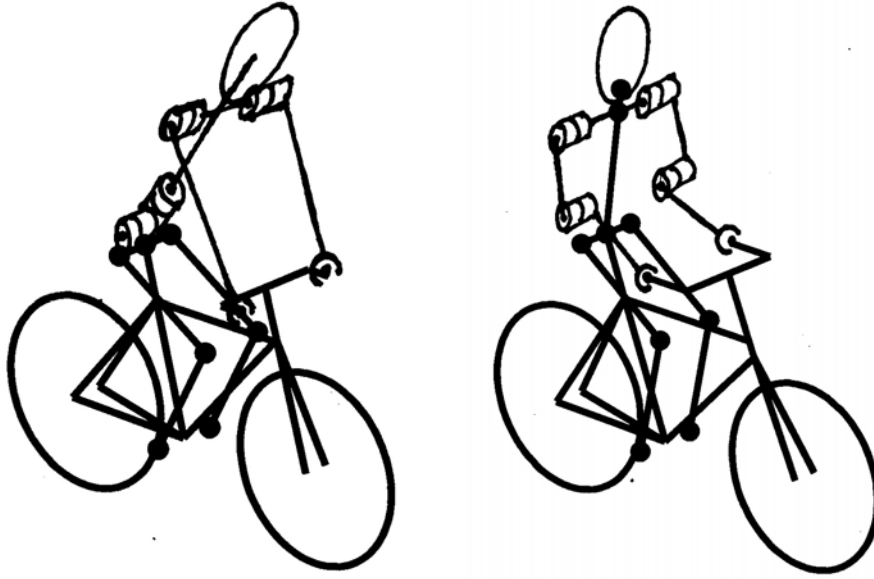


Figure 2-3: Left; stretched arm rider position. Right; bend arm rider position.

of incorporating lean action in the bicycle equations can be found in Schwab et al. (2011). However for now we will omit the rider lean action and limit ourselves to the roll and steer equations.

2-1-6 Control forms

For control purposes it is convenient to express the bicycle equations either in state space form or as a set of transfer functions.

2-1-7 State Space representation

The state space representation is give by:

$$\dot{\mathbf{x}} = \mathbf{A}\mathbf{x} + \mathbf{B}\mathbf{f} \quad (2-7)$$

$$\mathbf{y} = \mathbf{C}\mathbf{x} + \mathbf{D}\mathbf{f} \quad (2-8)$$

Here the state is chosen to be: $\mathbf{x} = [\dot{\phi}, \dot{\delta}, \phi, \delta]^T$, input $\mathbf{f} = [T_\phi, T_\delta]^T$ and output $\mathbf{y} = [\phi, \delta]^T$. The system matrix \mathbf{A} , input gain matrix \mathbf{B} , observer matrix \mathbf{C} and direct feed-through matrix \mathbf{D} are given by:

$$\begin{aligned} \mathbf{A} &= \begin{bmatrix} -\mathbf{M}^{-1}v\mathbf{C}_1 & -\mathbf{M}^{-1}(g\mathbf{K}_0 + v^2\mathbf{K}_2) \\ \mathbf{I} & \mathbf{0} \end{bmatrix}, & \mathbf{B} &= \begin{bmatrix} \mathbf{M}^{-1} \\ \mathbf{0} \end{bmatrix}, \\ \mathbf{C} &= \begin{bmatrix} \mathbf{0} & \mathbf{I} \end{bmatrix}, & \mathbf{D} &= \begin{bmatrix} \mathbf{0} \end{bmatrix}. \end{aligned} \quad (2-9)$$

2-1-8 Transfer function representation

The state space equations can also be expressed as a set of transfer functions $\mathbf{H}_{yf}(s)$ by making use of:

$$\mathbf{H}_{yf}(s) = \mathbf{C} (s\mathbf{I} - \mathbf{A})^{-1} \mathbf{B} + \mathbf{D}, \quad (2-10)$$

such that:

$$\mathbf{y}(s) = \mathbf{H}_{yf}(s)\mathbf{f}(s), \quad (2-11)$$

where the s denotes the Laplace argument. Finally we end by introducing the reference error \mathbf{z} . Since we are interested in roll stabilization, this simply becomes $\mathbf{z} = -\phi$, resulting in the following transfer function:

$$\mathbf{z}(s) = \mathbf{H}_{zf}(s)\mathbf{f}(s), \text{ where } \mathbf{H}_{zf}(s) = -[0, 0, 1, 0] \mathbf{H}_{yf}(s) \quad (2-12)$$

2-1-9 Summary

At a constant forward velocity the dynamic behavior of the bicycle is governed by the coupled lean and steer equations. In this case there are two inputs which influence the dynamic behavior of the system; 1.) by applying steering torque or 2.) by applying roll torque. The dynamic behavior of the bicycle is dependent on the bicycle parameters, forward velocity and gravity. The bicycle can be stabilized by steering into the fall. Passiver rider contributions affect the coefficients of the bicycle equations but not the structure itself. An additional degree of freedom may be introduced, describing the rider lean angle relative to the bicycle. For control purposes, it is convenient to transform the linear roll and steer equations to state space form or as a set of transfer functions.

2-2 Rider

In this section we will introduce a model structure describing the rider action. Such a model is desired, since it will allow for simulations of the combined/rider bicycle system. First, several rider models from literature were implemented and investigated, such as the optimal controller and the Lunteren and Stassen Model, which are both described in section A. Later on, we also obtained an experimental data set from our colleagues of the UC Davis. This section will mainly focus on the experimental model, since this experimental data set reduced the need for a literature based model. However, a great deal of time and energy is spend in understanding some of the models described in literature, for which a detailed analysis is given in appendix A.

Before moving on we'd like to point out that finding the right model structure is a iterative process, which requires a number of identification and parameter estimation cycles as described in chapter 4. Therefore, rider model presented in this section is the heuristic result of numerous and often unsuccessful iterations. The following parametric models were tried but proved to be unsuccessful in the sense that the model errors were rather large:

- Simple optimal controller
- Full state feedback controller
- Intuitive controller

Due to time limitations, these results are not included in this thesis. Next, we will introduce the resulting rider model, which will be used throughout this research.

2-2-1 Input/output structure

We start off with introducing a 'general' rider model structure. This structure is still general in the sense that no specific parametrization are defined, but the input/output structure is fixed. Here, we define a linear input and output structure of the rider model, where the parameters are assumed to be a function of the forward velocity v , since the bicycle dynamics are known to change with the forward velocity.

Rider input

The rider input is defined as the information on which the rider takes appropriate action. For example the rider output may depend explicitly variables like; forward velocity, bicycle configuration, age and even alcohol pro-millage, since these variables probably affect the steering capabilities of the rider. However, to keep things simple, we only consider the bicycle configuration \mathbf{y} and forward velocity v to be the input variables for the rider model.

Rider output

The rider output will act as an input on the bicycle model. According to Kooijman and Schwab (2008) the roll angle is mainly controlled by steering torque control, whereas the upper-body lean action is insignificant. Moreover, during the experiments described in chapter 3, this upper-body lean is restrained by a harness connected rigidly to the bicycle. In addition the knees are also connected to the bicycle frame through a set of magnets. All together, this makes it very unlikely that the rider uses other control means than the steering control. The bicycle model, described in section 2-1, consists of two inputs; roll torque T_ϕ , and steering torque T_δ . Since the rider is only expected to control the bicycle through steering action, we will omit the roll action.

Concludingly, the rider output only affects the generalized steering torque of the bicycle. This rider contribution to the generalized steering torque will be denoted by $T_{\delta,u}$, where the subscript u indicates the rider contribution.

Input/output definitions

Concludingly, the rider model structure will be of the following form:

$$\mathbf{u}(s) = \mathbf{K}(s, \boldsymbol{\theta}(v))\mathbf{y}(s) \quad (2-13)$$

with controller \mathbf{K} , which is a function of the velocity dependent parameters $\boldsymbol{\theta}(v)$ and defines a linear mapping between rider input $\mathbf{y} = [\phi, \delta]^T$ and output $\mathbf{u} = [T_{\delta, u}]^T$. Figure 2-4 shows a block scheme of this model structure.

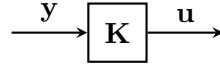


Figure 2-4: Block diagram of the general rider input/output structure, with controller $\mathbf{K} = \mathbf{K}(s, \boldsymbol{\theta}(v))$, input $\mathbf{y} = [\phi, \delta]^T$ and output $\mathbf{u} = [T_{\delta, u}]^T$.

Since the rider only outputs steering torque, the rider output can be incorporated within the bicycle equations in terms of the generalized forces \mathbf{f} , according to:

$$\mathbf{f}_u = \mathbf{H}_{fu} \mathbf{u} \quad , \quad \text{with} \quad \mathbf{H}_{fu} = \begin{bmatrix} 0 \\ 1 \end{bmatrix}. \quad (2-14)$$

2-2-2 Rider model structure

Now that we have defined the general input/output structure, we are ready to specify the internal control structure of \mathbf{K} . In addition we know that the rider model is limited by the inherent human limitations such as neuromuscular lag and time delay. We will start of by presenting a gain model, after which models for the human limitations are introduced.

Sensory feedback gains

Next we introduce a number of sensory feedback gains, which act linearly on the bicycle configuration output. We assume the rider to be capable of sensing and applying proportional, integrative, first and second order derivative action. These assumptions may be modeled mathematically according to:

$$K_\phi(s) = k_{\phi p} + k_{\phi i} s^{-1} + k_{\phi d} s + k_{\phi dd} s^2, \quad (2-15)$$

$$K_\delta(s) = k_{\delta p} + k_{\delta i} s^{-1} + k_{\delta d} s + k_{\delta dd} s^2, \quad (2-16)$$

with roll angle feedback K_{phi} and steer angle feedback K_δ . The gains k with subscript p , i , d and dd indicate proportional, integral, first and second order derivative gains respectively.

Next we will shortly analyze the sensory system of the rider. These available sensory systems regarding human movement control are described by Herman van der Kooij (2008). Table 2-1 indicates which variables may be observed by the sensory system.

In this table, a number of required feedback variables are still missing, including: $\int \phi dt$, $\dot{\phi}$, $\int \delta dt$ and $\dot{\delta}$. However, according to McRuer and Jex (1967) the human controller is capable of differentiating and integrating sensory feedback. By doing so, the human controller potentially has access to all of the required feedback variables. In addition, from equation 2-3 we observe that the heading is strongly related to the steering angle integral, which means that the rider may observe this variable directly through the use of vision.

On the other hand, the accuracy of these sensory systems may also be reduced by sensory noise, limited bandwidth, etc. It goes beyond the scope of this report to treat all these

Sensory system	Measured quantities	Bicycle variables
Muscle spindles:	position, velocity	$\delta, \dot{\delta}$
Golgi tendon organs:	force	T_δ
Vestibular:	acceleration, vertical angle	$\phi, \ddot{\phi}$
Vision:	position, velocities, horizon, etc.	$\phi, \delta, v, x, y, \psi$

Table 2-1: Sensory systems regarding human movement control and observed variables.

limitations in detail, so it remains questionable whether the rider is truly capable of sensing all of the required feedback variables.

More information about the human sensory system can be found in appendix E.

Rider limitations

According to McRuer and Jex (1967), the human controller is inherently limited by neuromuscular lag and time delays. Here neuromuscular dynamics are modeled using shoulder muscle parameters according to de Vlugt et al. (2003) and Happee et al. (2009), which yields:

$$G_{nm}(s) = \frac{\omega_c^2}{s^2 + 2\zeta\omega_c + \omega_c^2}, \quad (2-17)$$

with cutoff frequency $\omega_c = 2.17 \cdot 2\pi$ rad/s and damping coefficient $\zeta = \sqrt{2}$. This system acts as a critically damped second order filter with a cutoff frequency equal to ω_0 .

Next the transport delays result in an effective time delay. This delay is modeled according to de Vlugt et al. (2003), Happee et al. (2009) using shoulder muscle parameters, which yields:

$$G_\tau(s) = e^{-\tau_d s}, \quad (2-18)$$

with time delay $\tau_d = 0.03$ s.

Combined model

Finally the human limitations and gain model are combined to form a rider model according to equation 2-13. By combining equations 2-17, 2-18 and 2-16 we form:

$$\mathbf{K}(s) = G_{nm}(s)G_\tau(s) \begin{bmatrix} K_\phi(s) & K_\delta(s) \end{bmatrix} \quad (2-19)$$

The complete rider model is presented as a blockdiagram in figure 2-5.

Parameterization

Notice that the model given by equation 2-19 still needs to be parameterized. A natural choice would be to define the unknown gains as the parameters. In this case the parameter vector simply becomes:

$$\boldsymbol{\theta} = [k_{\phi p}, k_{\phi i}, k_{\phi d}, k_{\phi dd}, k_{\delta p}, k_{\delta i}, k_{\delta d}, k_{\delta dd}]^T \quad (2-20)$$

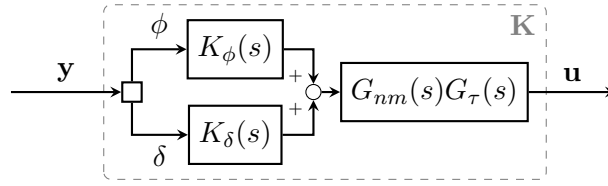


Figure 2-5: Block diagram of the inner control structure of \mathbf{K} , with roll and steering angle feedback gains K_ϕ and K_δ , timedelay G_τ , neuromuscular lag G_{nm} , input $\mathbf{y} = [\phi, \delta]^T$ and output $\mathbf{u} = [T_{\delta, u}]^T$.

These parameters will be determined later on by fitting the combined rider/bicycle model onto an experimental dataset. Later on, in section 4-2-2, we will try to reduce the number of parameters through parameter reduction techniques. As stated before, these parameters are assumed to be a function of the forward velocity, so actually $\boldsymbol{\theta} = \boldsymbol{\theta}(v)$.

2-2-3 Co-contraction

According to de Vlugt et al. (2003), the human operator may also use co-contraction as a possible control mechanism. Co-contraction is generated by contracting muscles of opposite functionality, which are called antagonists. By doing so, the human controller is able to effectively generate stiffness and damping to the system. This type of control is open loop and requires no feedback, therefore it does not suffer from neuromuscular lag and delay. In the case of bicycling, this co-contraction may be applied to the steering angle to steering torque control, and could be modelled according to:

$$T_{\phi, cc} = (k_{\delta p, cc} + k_{\delta d, cc} s) \delta, \quad (2-21)$$

with co-contraction steering torque $T_{\phi, cc}$, stiffness $k_{\delta p, cc}$ and damping $k_{\delta d, cc} s$. Since the co-contraction control is not limited by neuromuscular lag and transport delays, it provides a good mechanism for control of high frequency force perturbations during position tasks.

As an explorative side step, the co-contraction was added to the steering angle control of equation 2-19, for which a full system identification cycle is performed (similar as described in chapter 4). Here, the resulting parameter vector could not be uniquely identified, since $k_{\delta p, cc}$, $k_{\delta p}$ and $k_{\delta d, cc}$, $k_{\delta d}$ were dependent on each other. This resulted in huge unrealistic gain pairs of opposite sign, with little effect since they were mainly cancelling each other. In short, adding the co-contraction parameters to the parametric rider model proved to be troublesome and therefore is not recommended.

In addition, since we will only apply a roll torque perturbation, the steering action presumably requires feedback control instead of co-contraction control. Concludingly, we will not include co-contraction control into the rider model.

2-2-4 Summary

In this section we have introduced a general input/output structure for the rider model. In addition we also presented an internal model with proportional, integrative and first and second

order derivative feedback on the bicycle output configuration. This model also includes human limitations, such as neuromuscular lag and transport delay. Co-contraction is not included in the rider model. The rider model is summarized in figure 2-5, where a block diagram of the complete rider model is shown.

2-3 External input

In addition to the rider input, external forces may also act on the system. By using the principle of virtual power, these forces can be incorporated into the equations of motion as a generalized external force \mathbf{f}_w . Suppose we have an arbitrary force \mathbf{w} acting on point \mathbf{x} of the bicycle. This point can be expressed in terms of the generalized coordinates \mathbf{q} according to $\mathbf{x}(\mathbf{q})$. Next we set up the virtual power balance according to:

$$[\delta\dot{\mathbf{q}}]^T \mathbf{f}_w = [\delta\dot{\mathbf{x}}]^T \mathbf{w} , \quad (2-22)$$

where δ represents the variational operator. Next we take the partial derivative of \mathbf{x} with respect to \mathbf{q} , which yields:

$$[\delta\dot{\mathbf{q}}]^T \mathbf{f}_w = [\delta\dot{\mathbf{q}}]^T \left[\frac{\partial \dot{\mathbf{x}}}{\partial \dot{\mathbf{q}}} \right]^T \mathbf{w} . \quad (2-23)$$

Since the virtual velocity vector can take any value compatible with the constraints, the following equations should hold:

$$\mathbf{f}_w = \mathbf{H}_{fw} \mathbf{w} , \text{ with } \mathbf{H}_{fw} = \left[\frac{\partial \dot{\mathbf{x}}}{\partial \dot{\mathbf{q}}} \right]^T . \quad (2-24)$$

2-4 General control description

According to Skogestad and Postlethwaite (2005) almost any plant and controller can be described according to the block scheme presented in figure 2-6. In this section we will combine and rewrite the bicycle/rider dynamics into this generalized control form. This model separates the unknown human controller \mathbf{K} from the known plant \mathbf{P} which contains the bicycle equations (including passive rider contribution). The general plant has two inputs, namely; external input \mathbf{w} and control output \mathbf{u} and two outputs; reference error \mathbf{z} and control input \mathbf{y} . All the analysis is done in the Laplace domain, so for convenience the Laplace operator s will be dropped throughout the subsequent analysis.

2-4-1 Block definitions

Next, we will define the blocks of the general control description. The rider controller \mathbf{K} is already defined in the rider section, so we only need to define the generalized plant \mathbf{P} . Lets start off by partitioning the generalized plant in terms of input/output contributions according to:

$$\mathbf{P} = \begin{bmatrix} \mathbf{P}_{zw} & \mathbf{P}_{zu} \\ \mathbf{P}_{yw} & \mathbf{P}_{yu} \end{bmatrix} , \quad (2-25)$$

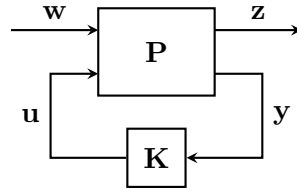


Figure 2-6: Block diagram of the general control description, with known bicycle dynamics \mathbf{P} , unknown controller \mathbf{K} , disturbance input \mathbf{w} , error output $\mathbf{z} = -\phi$, control input \mathbf{y} and control output \mathbf{u} .

such that we can write:

$$\mathbf{z} = \mathbf{P}_{zw}\mathbf{w} + \mathbf{P}_{zu}\mathbf{u} , \quad (2-26)$$

$$\mathbf{y} = \mathbf{P}_{yw}\mathbf{w} + \mathbf{P}_{yu}\mathbf{u} . \quad (2-27)$$

Let us compare this with the bicycle equations, where the force input is a summation of the external force and rider force, according to:

$$\mathbf{f} = \mathbf{f}_w + \mathbf{f}_u \quad (2-28)$$

By combining equations 2-11, 2-12 and 2-28 we derive:

$$\mathbf{z} = \mathbf{H}_{zf}\mathbf{H}_{fw}\mathbf{w} + \mathbf{H}_{zf}\mathbf{H}_{fu}\mathbf{u} , \quad (2-29)$$

$$\mathbf{y} = \mathbf{H}_{yf}\mathbf{H}_{fw}\mathbf{w} + \mathbf{H}_{yf}\mathbf{H}_{fu}\mathbf{u} . \quad (2-30)$$

From this we observe that:

$$\mathbf{P}_{zw} = \mathbf{H}_{zf}\mathbf{H}_{fw} ,$$

$$\mathbf{P}_{zu} = \mathbf{H}_{zf}\mathbf{H}_{fu} ,$$

$$\mathbf{P}_{yw} = \mathbf{H}_{yf}\mathbf{H}_{fw} ,$$

$$\mathbf{P}_{yu} = \mathbf{H}_{yf}\mathbf{H}_{fu} .$$

2-4-2 Closed loop transfer function

Next we will derive the closed loop transfer function from \mathbf{w} to \mathbf{z} and \mathbf{y} . Lets start off by writing out input \mathbf{u} in terms of \mathbf{w} :

$$\begin{aligned} \mathbf{u} &= \mathbf{K}\mathbf{y} , \\ &= \mathbf{K}(\mathbf{P}_{yw}\mathbf{w} + \mathbf{P}_{yu}\mathbf{u}) , \\ &= (\mathbf{I} - \mathbf{K}\mathbf{P}_{yu})^{-1} \mathbf{K}\mathbf{P}_{yw}\mathbf{w} . \end{aligned} \quad (2-31)$$

Substituting 2-31 into 2-27 yields the following closed loop transferfunctions:

$$\mathbf{z} = \left[\mathbf{P}_{zw} + \mathbf{P}_{zu}(\mathbf{I} - \mathbf{K}\mathbf{P}_{yu})^{-1} \mathbf{K}\mathbf{P}_{yw} \right] \mathbf{w} , \quad (2-32)$$

$$\mathbf{y} = \left[\mathbf{P}_{yw} + \mathbf{P}_{yu}(\mathbf{I} - \mathbf{K}\mathbf{P}_{yu})^{-1} \mathbf{K}\mathbf{P}_{yw} \right] \mathbf{w} . \quad (2-33)$$

For which the second equation will prove to be the most useful, therefore we introduce the shorthand notation:

$$\mathbf{y} = \mathbf{G}\mathbf{w} \quad , \quad \mathbf{G} = \left[\mathbf{P}_{yw} + \mathbf{P}_{yu}(\mathbf{I} - \mathbf{K}\mathbf{P}_{yu})^{-1} \mathbf{K}\mathbf{P}_{yw} \right] . \quad (2-34)$$

This result can be used to simulate output of the system by applying some disturbance signal $\mathbf{w}(t)$ to the system. They also allow for stability analysis, which can be achieved by analyzing the poles of these transfer functions. If the poles all lie in the negative real plane, then the closed loop system is stable.

2-4-3 Summary

In this section we introduced the concept of a general control description. The resulting model describes the dynamics of the combined system, while the known plant and unknown controller are still separated. This general description will prove to be useful in subsequent analysis.

Experimental Data Analysis

Thanks to the excellent work of our colleagues Jason Moore and Luke Dale Peterson under supervision of Prof. Mont Hubbard of the UC Davis, we obtained a large experimental dataset regarding rider identification in bicycling. In this chapter the experiment, by which the data set is generated, is explained briefly and the measured variables are introduced. The dynamic properties of the bicycle and passive rider are also measured, which can be combined into the linearized mass, damping and stiffness matrices. In succeeding chapters, these measurements and bicycle properties will be used for system identification and parametric modeling of the human controller.

3-1 Experiment description

The goal of their experiment is similar to ours, namely to identify human rider control in bicycling. In order to achieve this goal, a measurement bicycle is constructed, which is fully equipped with a number of sensors to measure the state, rider input, etc. In addition, a perturbation mechanism is also created, which is used to excite the system. These perturbations are applied by laterally pulling a rope, which is attached just below the seat of the rider. The following constraints are also build in to the measurement bicycle:

- The upper body lean is constrained by rigidly fixing the upper body with a harness to the bicycle frame.
- The bicycle is electrically driven, so the rider does not need to exert pedaling power and thus eliminates the need for lower limb movement.
- The knees are also fixed to the bicycle frame, which prevents the lateral knee movement described in Kooijman and Schwab (2008)

Two different kinds of experiments are performed; lateral line tracking and roll stabilization of which only the latter is used for further analysis, since the goal of our research is about



Figure 3-1: Photo of the measurement bicycle which is used for rider identification in bicycling. Source: picasaweb.google.com/moorepants.

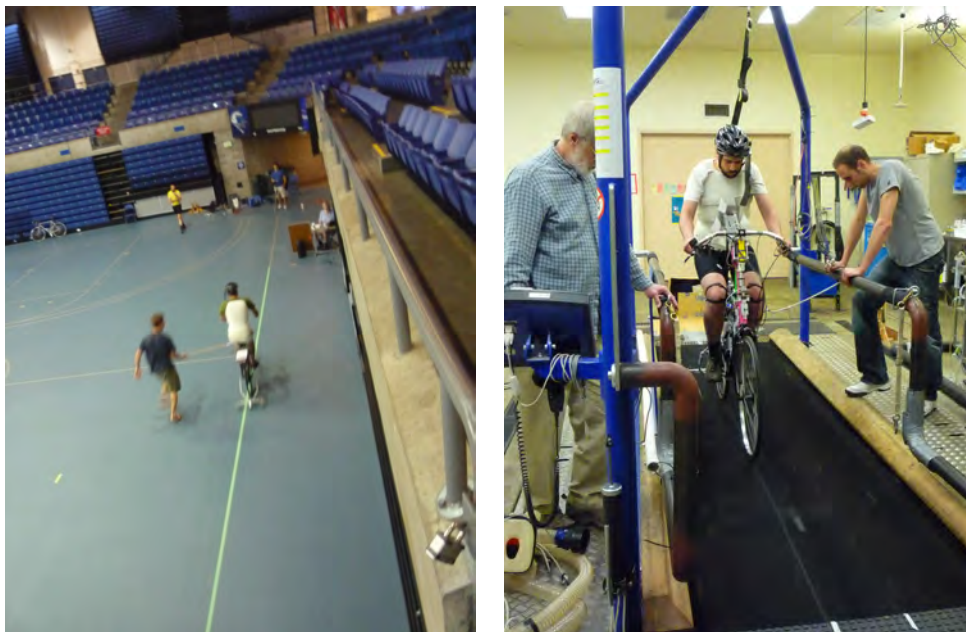


Figure 3-2: Left; perturbation run performed on the pavilion floor. Right; balance exercise performed on a horse treadmill. Source: picasaweb.google.com/moorepants.

Variable	Symbol	Units	Notes
Forward velocity	v	[m/s]	-
Roll angle	ϕ	[rad]	-
Steering angle	δ	[rad]	-
Roll rate	$\dot{\phi}$	[rad/s]	-
Steering rate	$\dot{\delta}$	[rad/s]	-
Disturbance force	w	[N]	-
Steering torque	T_δ	[Nm]	Still contains some errors

Table 3-1: Variables which are measured during the experiments in Davis, California.

RunID	Rider	v (m/s)	T (s)	Environment	Datetime	Task description
105	Jason	3.2	60	Horse treadmill	24-Feb-2011 18:28:23	Line tracking with disturbance
280	Luke	2.1	90	Horse treadmill	30-Aug-2011 15:38:43	Balance with Disturbance
282	Luke	4.3	90	Horse treadmill	30-Aug-2011 16:07:59	Balance with Disturbance
285	Luke	7.4	90	Horse treadmill	30-Aug-2011 16:20:52	Balance with Disturbance

Table 3-2: Run number used for further data analysis. Notice that the rider and task of the first entry is different from the other three.

stabilizing the bicycle. The experiments are performed in two environments; on a horse treadmill and at the pavilion floor (figure 3-2). The horse treadmill proved to be more suitable for the perturbation experiments, since it is more easy to perturb a stationary positioned bicycle by pulling the rope. A downside of this environment is the rather narrow track, resulting in a stressful and unnatural overly concentrated way of bicycling. The treadmill perturbation experiments are performed at forward velocities of 2, 3, 4 and 7 m/s with a measurement time of $T = 60 - 90$ seconds, each of them is repeated a number of times. After the experiments the dimensions and inertial properties of the bicycle are measured in order to obtain the dynamic model. The passive rider contribution is also included in the model, which are determined according to Yeadon and Morlock (1989).

3-1-1 Data description

Table 3-1 shows the variables that were obtained for each experiment. Four trials are chosen for further analysis, which are shown in table 3-2. The corresponding data for these trials is publicly available and may be downloaded from: <http://biosport.ucdavis.edu/research-projects/bicycle/instrumented-bicycle>. These 4 trials are chosen, because they showed a clear input/output relationship, which allows for system identification. Here, the first run is performed with a different rider and task description than the other three, which may make it hard to compare with each other. Figure 3-3 shows a typical measurement of the roll angle, steering angle and input force.

3-1-2 Bicycle and passive rider measurements

Next the dynamic properties of the bicycle and passive rider are measured according to Moore et al. (2010). These measurements include frame dimensions, inertial properties of

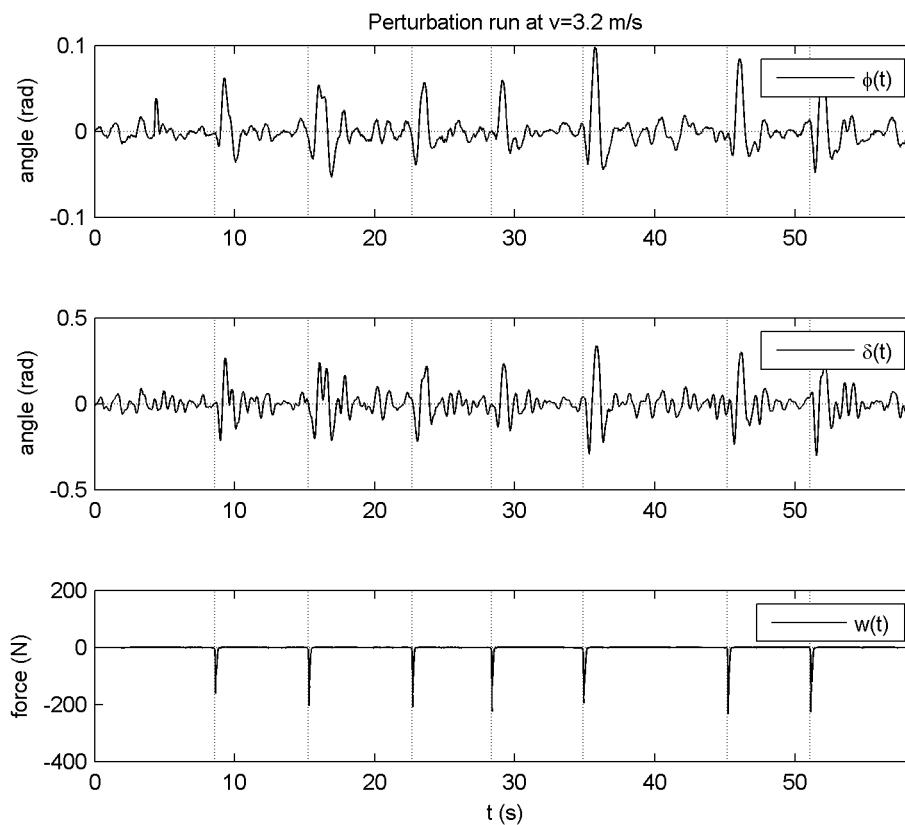


Figure 3-3: Measurements of the roll angle ϕ (top), steering angle δ (middle) and disturbance w (bottom) for a forward velocity of 3.2 m/s.

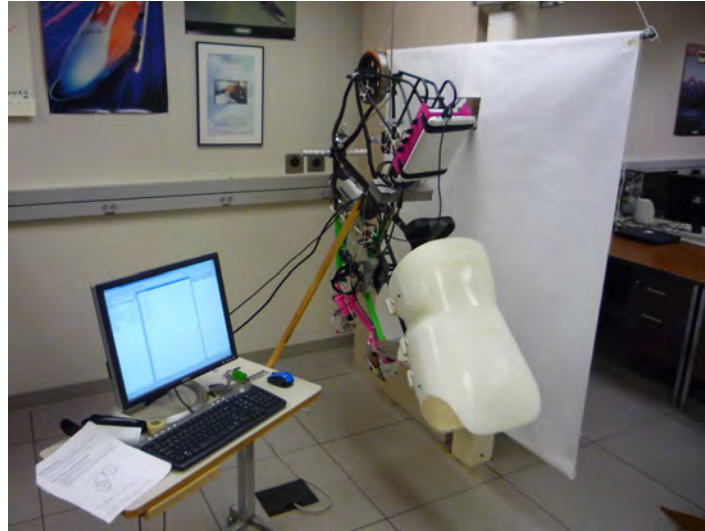


Figure 3-4: Inertial measurement of the bicycle frame by using a known torsional spring.

the separate bicycle parts (frame, steering fork, front and rear wheel) and passive dynamic properties of the human rider according to Yeadon and Morlock (1989). Figure 3-4 shows a typical inertial measurement performed on the bicycle frame. Here, a torque spring with a known stiffness is used to estimate the moment of inertia around this torque axis by measuring the eigenfrequency. The bicycle/rider measurements can be combined to derive the mass, damping and stiffness matrices of the bicycle equations introduced in chapter 2. During the experiments the body lean angle was fixed using an upper body harness fixed to the bicycle, resulting in $\gamma = 0$. This fixation effectively reduces the configuration space to $\mathbf{q} = [\phi, \delta]^T$. The measured bicycle and estimated rider properties result in the following coefficient matrices:

$$\mathbf{M}_0 = \begin{bmatrix} 131.5085 & 2.6812 \\ 2.6812 & 0.2495 \end{bmatrix},$$

$$\mathbf{K}_0 = \begin{bmatrix} -116.19 & -2.7633 \\ -2.7633 & -0.94874 \end{bmatrix},$$

$$\mathbf{K}_2 = \begin{bmatrix} 0 & 102.02 \\ 0 & 2.5001 \end{bmatrix},$$

$$\mathbf{C}_1 = \begin{bmatrix} 0 & 42.748 \\ -0.31806 & 1.6022 \end{bmatrix}.$$

The transfer function which maps the external force to the generalized force is calculated using multi-body software (Autolev) and given by:

$$\mathbf{H}_{fw} = \begin{bmatrix} 0.91 \\ 0.014408 \end{bmatrix}, \quad (3-1)$$

From this we observe that the external force mainly excites the roll torque input and not so much of the steering torque input. This makes sense, because the rope is attached under the rider seat and is pulled in a lateral direction, which mainly causes a roll torque. This data

can be combined into a reduced generalized plant model \mathbf{P} according to:

$$\begin{bmatrix} z \\ \mathbf{y} \end{bmatrix} = \begin{bmatrix} \mathbf{P}_{zw} & \mathbf{P}_{zu} \\ \mathbf{P}_{yw} & \mathbf{P}_{yu} \end{bmatrix} \begin{bmatrix} w \\ u \end{bmatrix}, \quad (3-2)$$

with external input w , controller input $\mathbf{y} = [\phi, \delta]^T$, error output $z = -\phi$ and controller output $u = T_{\delta,u}$. This description will be used in the next chapter, where we combine the known system dynamics and measurements to obtain a model for the rider action.

3-2 Summary

In this chapter we have introduced an experimental dataset, which is obtained by our colleagues of the UC Davis. The dataset includes a number of perturbation runs, which are of particular interest when identifying rider behavior. Many of these perturbation runs were performed on a rather small horse treadmill, which seemed to result in a stressful and overly concentrated way of bicycling. A number of variables are measured during these experiments, including; roll angle, steering angle and the external disturbance. The first run at $v = 3.2$ m/s is performed by a different rider and with a different task description than the other runs. In addition the dynamic properties of the bicycle and passive rider are also measured, resulting in the known system dynamics. Next, these measurements and known system dynamics will be used for identifying rider control in bicycling.

System Identification

In this chapter we will use the experimental data set, described in the previous chapter, to identify the underlying models. In order to achieve this, we will turn ourselves to system identification methods. First some of the basic theory of system identification will be covered, after which a specific application is given for the bicycle case. Finally some analysis is performed on these identification results.

4-1 Theory

According to Ljung (1987) the system identification procedure requires the following three basic entities:

1. Data record of input and output signals.
2. Model structure; a set of candidate models.
3. Criterium; a rule by which candidate models can be assessed to the data.

The input and output data will be follow from the experiment. This experiment should be set up such that the data record is highly informative. This concept of an informative dataset is explained in more detail in section 5-5 and follows from a careful experiment design. Here, choices should be made concerning which variables should be measured and where and what inputs signals should be applied.

The model structure is the set of models which are fitted onto the data record. These models offer a parametric mapping from input to output data. Dependent of the model, these parameters are determined using linear methods, or by parameter optimization algorithms. In section 4-2-2 the specific model structure will be discussed in more detail.

These models will be evaluated by a criterium, for which often the least squares selection rule is used. This selection rule is discussed in section 4-1-5.

4-1-1 System description

Next we introduce some of the basis system description theory of system identification. The theory presented here, is mainly based on Ljung (1987) and will be about linear systems, which are subjected to additive random disturbances. Here, the input/output data is modeled according to the block diagram shown in figure 4-1. This type of systems is described by:

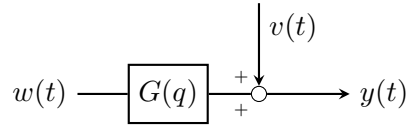


Figure 4-1: System description, with; output $y(t)$, input $w(t)$, disturbance $v(t)$ and system $G(q)$.

$$y(t) = G(q)w(t) + v(t) , \quad (4-1)$$

with output $y(t)$, input $w(t)$, disturbance $v(t)$ and model $G(q)$. The q operator acts as a discrete shifting function, such that $q^{-k}w(t) = w(t - k)$. This is a convenient description, because it separates the deterministic input related contribution $G(q)w(t)$ from the stochastic contribution $v(t)$. The stochastic contribution may be split up into a deterministic noise filter $H(q)$ and underlying stochastic process $e(t)$, such that:

$$v(t) = H(q)e(t) . \quad (4-2)$$

The system identification challenge; for a given dataset, consisting of input $u(t)$ and output $y(t)$, we like to identify the underlying input $G(q)$ and noise model $H(q)$. For the linear case, these models describe a linear mapping between input and output according to:

$$G(q) = \sum_{k=1}^{\infty} g(k)q^{-k} , \quad (4-3)$$

$$H(q) = 1 + \sum_{k=1}^{\infty} h(k)q^{-k} , \quad (4-4)$$

The latter being normalized, such that $H(0) = 1$. These models basically describe convolution operators, which map the inputs to the output. Throughout the succeeding analysis, it will be assumed that the stochastic input $e(t)$ is a white noise signal with zero mean $\mu_e = 0$ and variance λ .

The linear system description presented in this section will form the base for all subsequent analysis. Both time and frequency identification methods will expand on this description.

4-1-2 Time domain expressions

First we introduce some definitions, which are useful when working with time domain data. The auto covariance of some arbitrary signal $s(t)$ and cross covariance of arbitrary signals

$s(t)$ and $w(t)$ are defined as:

$$R_s(\tau) = \lim_{N \rightarrow \infty} \sum_{t=1}^N s(t)s(t-\tau), \quad (4-5)$$

$$R_{sw}(\tau) = \lim_{N \rightarrow \infty} \sum_{t=1}^N s(t)w(t-\tau). \quad (4-6)$$

where τ represents a time shift. If the cross covariance between two signals is zero, than it is said that the signals uncorrelated, which means they are independent of each other. This is a useful tools, since the $v(t)$ and $u(t)$ are often found to be uncorrelated. In addition, since the zero mean white noise input $e(t)$ is uncorrelated for $\tau \neq 0$, it can be shown that:

$$R_v(\tau) = \lambda \sum_{k=0}^{\infty} h(k)h(k-\tau) \quad (4-7)$$

4-1-3 Frequency domain expressions

Next, we introduce the frequency domain expressions by applying a discrete Fourier transformation (DFT). For an arbitrary signal $s(t)$ of length N the transformation yields:

$$S_N(\omega) = \frac{1}{\sqrt{N}} \sum_{t=1}^N s(t)e^{-i\omega t} \quad (4-8)$$

For which the inverse discrete Fourier transformation (IDFT) is given by:

$$s(t) = \frac{1}{\sqrt{N}} \sum_{k=1}^N S_N(2\pi k/N) e^{i2\pi kt/N} \quad (4-9)$$

The Fourier transformation of the auto and cross covariance functions are called the cross and auto spectral density, which are given by:

$$\Phi_s(\omega) = \sum_{\tau=-\infty}^{\infty} R_s(\tau)e^{-i\omega\tau}, \quad (4-10)$$

$$\Phi_{sw}(\omega) = \sum_{\tau=-\infty}^{\infty} R_{sw}(\tau)e^{-i\omega\tau}. \quad (4-11)$$

By taking the DFT of the cross covariance of the disturbance spectrum R_v , it can be shown that:

$$\Phi_v(\omega) = \lambda \left| H(e^{i\omega}) \right|^2. \quad (4-12)$$

Similar to 4-7 this is a usefull expression, since the noise cancels out, leaving only the variance λ and noise model $H(e^{i\omega})$. Later on we will use this result to obtain a noise model.

4-1-4 Nonparametric Linear models

Next we introduce some nonparametric linear model structures. These structures are not confined to a limited parameter space, instead they contain many parameters and are able to model about any linear model. This makes them widely applicable, however there are certain limitations on these models. Most importantly, the described nonparametric model structures require $v(t)$ and $w(t)$ to be independent, so: $R_{vw} = 0$. This is generally not the case when identifying closed loop configurations, where the noise is correlated with the input due to the feedback. Solutions to closed loop estimators do exist however, but for now we will focus on the open loop case where $R_{vw} = 0$.

These non parametric model structures exist for both time and frequency domain data. The frequency domain models are strictly correct, only for the case when the input is periodic and where all the transients have died out, whereas the time domain models require the input and output signals prior to $t = 0$ to be zero. The choice of method thus depend on the type of data generated.

Time domain method

Starting of with equations 4-1 and 4-3 and by projecting the input $w(t)$ onto the output we derive:

$$R_{yw}(\tau) = \sum_{k=1}^{\infty} g(k)q^{-k}R_w(k - \tau) + R_{vw}(\tau) , \quad (4-13)$$

It is assumed that the system has stable dynamics ($\sum_{k=1}^{\infty} |g(k)| < \infty$ and $\sum_{k=1}^{\infty} |h(k)| < \infty$) and that the input $w(t)$ is uncorrelated with the stochastic disturbance $v(t)$, resulting in $R_{vw} = 0$. Since the system is stable, impulse response will gradually die out, and therefore can be estimated by applying an finite observation length. Suppose the input $u(t)$ is independent of the noise $v(t)$ and we have a finite dataset of length N , and the impulse response is well described withing m samples. Finally we have a finite dataset of N samples. In this case, the system can be approximated by:

$$\hat{R}_{yw}^N(\tau) = \sum_{k=1}^m \hat{g}_N(k)q^{-k}\hat{R}_w^N(k - \tau) , \quad (4-14)$$

where superscript N denotes the finite observation length approximations of the covariance functions. The solution to this problem is similar to the FIR model, which is treated in section 4-2.

Frequency domain method

Starting of with equation 4-14 and by transformation to the frequency domain, we may obtain:

$$\hat{\Phi}_{yw}^N(\omega) = \hat{G}_N(e^{i\omega})\hat{\Phi}_w^N(\omega) , \quad (4-15)$$

which can be solved easily for $\hat{G}_N(e^{i\omega})$ according to:

$$\hat{G}_N(e^{i\omega}) = \frac{\hat{\Phi}_{yw}^N(\omega)}{\hat{\Phi}_w^N(\omega)} , \quad (4-16)$$

The frequency domain conversion can be done very efficiently by making use of the Fast Fourier transformation algorithm (FFT). And since convolution becomes multiplication in the frequency domain, the unknown transfer functions may be obtained far more efficiently compared to time domain methods. A DFTF conversion assumes the input to be periodic, which is not the case for the current data set. However, by applying proper windowing techniques, periodicity may be imposed on the dataset. In addition, frequency averaging may be used to reduce the noise at the cost of decreasing the frequency resolution.

Finally the estimated transfer function may be used to estimate the disturbance spectrum, according to:

$$\hat{\Phi}_v^N(\omega) = \hat{\Phi}_y^N(\omega) - |\hat{G}_N(e^{i\omega})|^2 \hat{\Phi}_w^N(\omega) . \quad (4-17)$$

4-1-5 Parametric linear models

The set of data, which is described by equation 4-1, may be modelled similar according to:

$$y(t, \theta) = G(q, \theta)w(t) + H(q, \theta)e(t) , \quad (4-18)$$

where $y(t, \theta)$ denotes the modeled output and θ denotes the parameter vector. There are two different kind of models which can be identified.

- Black-box model structures (non-physical)
- Model structures with physical parameters

Examples of black box models include; ARX, ARMAX, OE, BOX-Jenkins, etc. Whereas the physical models may be obtained by first principles. For this research the latter is most interesting, since we are interested in finding a physical explanation for human rider action. In either case, we want to determine the parameters, such that they minimize a some objective function $V_N(\theta)$. This can be reformulated into an optimization problem, for which an optimal parameter vector can be found according to:

$$\hat{\theta}_N = \arg \min_{\theta} V_N(\theta) , \quad (4-19)$$

where $\hat{\theta}_N$ denotes the optimal solution and $V_N(\theta)$ denotes the criterium function, which is subject of minimization. For time domain estimation, a common criteria function would be the following quadratic criteria:

$$V_N(\theta) = \frac{1}{N} \sum_{t=1}^N \frac{1}{2} e^2(t, \theta) \quad (4-20)$$

where the error is defined to be difference between the measured $y(t)$ and modeled output $y(t, \theta)$:

$$e(t, \theta) = y(t) - y(t, \theta) , \quad (4-21)$$

For the case of frequency domain identification, a commonly used sum of squares criteria would be:

$$V_N(\theta) = \frac{1}{N} \sum_{k=1}^N \left| \hat{G}_N(e^{i\omega_k}) - G_N(e^{i\omega_k}, \theta) \right|^2 \frac{\hat{\Phi}_u^N(\omega_k)}{\hat{\Phi}_v^N(\omega_k)}, \quad (4-22)$$

which is frequency domain counterpart to the time domain criteria function (equation 4-20). Again, this criteria is a sum of errors squared, weighted by the signal to noise ratio. The minimization of is often non linear in the parameters and requires complex optimization algorithms. More in depth information about optimization methods can be found in Papalambros and Wilde (2000).

4-1-6 Model evaluation

Suppose we model structure appears to be correct and that we have found the solution $\hat{\theta}_N$ to the optimization problem presented in equation 4-22. Let us next evaluate quality of the fit and parameter uncertainty. A common criterium of analyzing the fitting quality is the Variance Accounted For (VAF), which is defined as the normalized difference between modeled output and measured output.

$$\text{VAF} = 1 - \frac{\sum_{t=1}^N |y(t) - \hat{y}(t, \theta)|^2}{\sum_{t=1}^N |y(t)|^2}, \quad (4-23)$$

where a VAF score of 1 means a perfect fit. In addition we can get estimate the parameter uncertainty by analyzing the parameter sensitivity and noise levels. The parameter covariance can either be obtained from numerical optimization output or analytically. It can be shown that for a quadratic error criterium the parameter covariance can be estimated as:

$$\text{cov } \hat{\theta} = \hat{\lambda}_N \left[\frac{1}{N} \sum_{t=1}^N \psi(t, \hat{\theta}_N) \psi^T(t, \hat{\theta}_N) \right]^{-1}, \quad (4-24)$$

with variance $\hat{\lambda}_N$ and model sensitivity $\psi(t, \hat{\theta}_N)$, which are defined as:

$$\hat{\lambda}_N = \frac{1}{N} \sum_{t=1}^N e^2(t, \hat{\theta}_N), \quad (4-25)$$

$$\psi(t, \hat{\theta}_N) = -\frac{d}{d\theta} e(t, \hat{\theta}_N) = \frac{d}{d\theta} y(t, \hat{\theta}_N). \quad (4-26)$$

Appendix D describes how this result can be related to the Matlab optimization output.

Finally we present the analytic parameter covariance for the frequency domain, which will be used later on during the experiment design described in chapter 5. The analytic parameter covariance expressed in the frequency domain is given by:

$$\text{cov } \hat{\theta}_N = \frac{1}{N} \left[\sum_{k=1}^N G_{,\theta}^T(e^{i\omega_k}, \theta) \frac{\hat{\Phi}_w^N(\omega_k)}{\hat{\Phi}_v^N(\omega_k)} G_{,\theta}(e^{i\omega_k}, \theta) \right]^{-1}, \quad (4-27)$$

where $G_{,\theta}(e^{i\omega}, \theta)$ denotes the partial derivative of G with respect to the parameters θ after which it is substituted with $\hat{\theta}_N$. From this result we observe that the covariance decreases

with proportional to $1/N$ as the number of samples increases. In addition, it is dependent on the signal-to-noise ratio and parameter sensitivity of the parametric model.

The standard error of the mean (sem) can be obtained by taking the square root of the diagonal terms of the parameter covariance expression. These values indicate the uncertainty of the parametric fitting, where a lower standard error of the mean corresponds to better parameter accuracy.

4-2 Application

Next the theory is applied onto the dataset presented in the previous chapter. Here we are interested in determining the closed loop unknown human controller contribution \mathbf{K} . However, we first will focus on obtaining a non parametric open loop model from w to \mathbf{y} . After that, we use our knowledge of the known bicycle equations to estimate the parametric rider model. This parametric model is then optimized by using parameter reduction techniques, which reduce the number of parameters. The analysis is performed for forward velocities of $v = 2.1, 3.1, 4.3$ and 7.4 m/s, resulting in a set of parametric models, which are discussed in the next section.

4-2-1 Non Parametric Modeling

We start off by obtaining a nonparametric model for the input correlated data. Here we have two options; frequency or time domain modeling. Since the input is non periodic and consists of an number of impulses, we choose the impulse response representation, so $\mathbf{G} = \mathbf{G}(q)$.

Notice that our system \mathbf{G} described in equation 2-34 has one input $w(t)$ and two outputs, namely $\phi(t)$ and steering angle $\delta(t)$. This makes it effectively an MISO model, which we may split up into two SISO models according to:

$$\mathbf{G}(q) = \begin{bmatrix} G_\phi(q) \\ G_\delta(q) \end{bmatrix}, \quad (4-28)$$

such that $\phi(t) = G_\phi(q)w(t)$ and $\delta(t) = G_\delta(q)w(t)$.

Let's start off by reintroducing the impulse response representation of G (equation 4-3), which may be rewritten into:

$$G(q) = \sum_{k=1}^m g(k)q^{-k} + \sum_{k=m+1}^{\infty} g(k)q^{-k}. \quad (4-29)$$

This impulse response function is of infinite length, which means we will never be fully able to estimate it, since our dataset is of finite time. Fortunately, if the system G is asymptotically stable, then the impulse response is expected to die out over time. In this case, the model may be approximated by simply taking the first m samples, according to:

$$\hat{G}(q) = \sum_{k=1}^m \hat{g}(k)q^{-k}, \quad (4-30)$$

which is known as a FIR model and represents an impulse response function of finite length.

Obtaining the FIR coefficients

The unknown coefficient of this FIR model may be estimated by using the measured input $w(t)$ and output $y(t)$ data. The output data is either represents $y(t) = \phi$ corresponding to $G_\phi(q)$ or $y(t) = \delta(t)$ corresponding to $G_\delta(q)$. We assume a finite discrete normalized time; $t = 1, 2, 3, \dots, n$, such that:

$$\begin{aligned} y(t) &= \sum_{k=1}^m \hat{g}(k)q^{-k}w(t) + v(t) , \\ &= \sum_{k=1}^m \hat{g}(k)w(t - k) + v(t) . \end{aligned} \quad (4-31)$$

From the experiment we know that no input outside the measurement interval $\{1 < t < n\}$ is applied, which can be expressed as: $w(t) = 0$ for $t < 1$ and $t > n$. The summations may be written out into matrix notion, resulting in:

$$\mathbf{y} = \mathbf{F}\mathbf{x} + \boldsymbol{\epsilon} , \quad (4-32)$$

where:

$$\begin{aligned} \mathbf{y} &= [y(1) \quad \dots \quad y(n)]^T , \\ \mathbf{x} &= [\hat{g}(1) \quad \dots \quad \hat{g}(m)]^T , \\ \mathbf{F} &= \begin{bmatrix} w(1-1) & \dots & w(1-m) \\ \vdots & \ddots & \vdots \\ w(n-1) & \dots & w(n-m) \end{bmatrix} , \\ \boldsymbol{\epsilon} &= [\epsilon(1) \quad \dots \quad \epsilon(n)]^T . \end{aligned}$$

Since we are interested in finding a model that represents the measured output as accurate as possible, we are interested in finding an optimal parameter vector \mathbf{x} such that a certain error function is minimized. In engineering, a common criteria is the following sum of least squares criterium:

$$\begin{aligned} V(\mathbf{x}) &= \frac{1}{2}\boldsymbol{\epsilon}^T \boldsymbol{\epsilon} , \\ &= \frac{1}{2}(\mathbf{F}\mathbf{x} - \mathbf{y})^T (\mathbf{F}\mathbf{x} - \mathbf{y}) , \\ &= \frac{1}{2}(\mathbf{x}^T \mathbf{F}^T \mathbf{F}\mathbf{x} - \mathbf{x}^T \mathbf{F}^T \mathbf{y} - \mathbf{y}^T \mathbf{F}\mathbf{x} + \mathbf{y}^T \mathbf{y}) . \end{aligned} \quad (4-33)$$

For which an optimal solution can be found by solving the following optimization problem:

$$\hat{\mathbf{x}} = \arg \min_{\mathbf{x}} V(\mathbf{x}) , \quad (4-34)$$

with optimal solution $\hat{\mathbf{x}}$. This problem can be solved analytically by setting the partial derivative of the criterium V with respect to the parameters \mathbf{x} to zero:

$$\frac{\partial V}{\partial \mathbf{x}} = \mathbf{F}^T \mathbf{F}\hat{\mathbf{x}} - \mathbf{F}^T \mathbf{y} = \mathbf{0} . \quad (4-35)$$

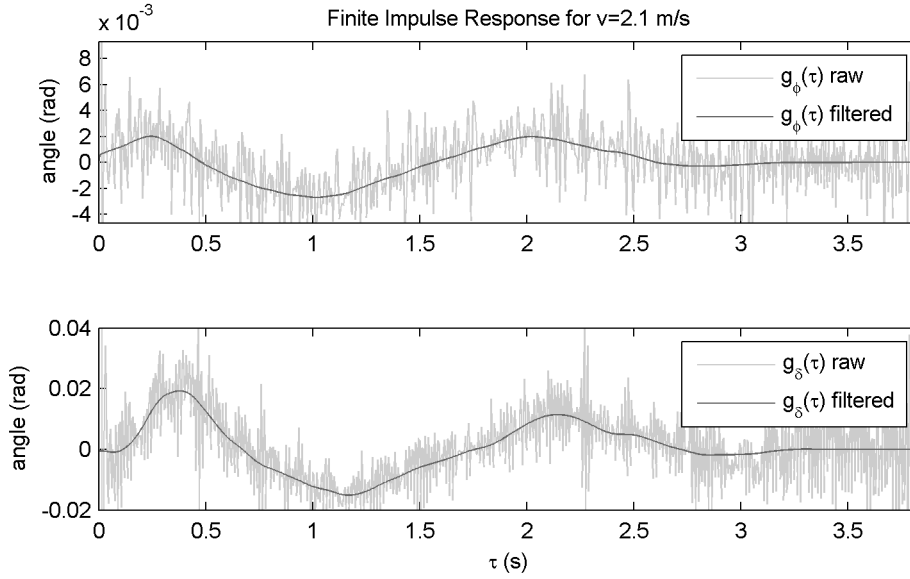


Figure 4-2: Impulse response model for the roll angle δ (top) and steering angle δ (bottom) for a forward velocity of $v = 2.1$ m/s. The raw FIR model is smoothed using a low pass filtering with a cutoff frequency of 10 Hz.

Solving for $\hat{\mathbf{x}}$ requires the matrix $\mathbf{F}^T\mathbf{F}$ to non singular. Under this assumption the optimal solution (in a least square sense) becomes:

$$\hat{\mathbf{x}} = (\mathbf{F}^T\mathbf{F})^{-1} \mathbf{F}^T\mathbf{y} . \quad (4-36)$$

This solution is implemented in Matlab and applied to the actual measurements. After experimenting with different finite impulse lengths, the oscillations are found to die out after $m = 768$ samples, which corresponds to finite response length of 3.84 seconds. The FIR models are smoothed by applying a low pass 8th order Butter-worth filter with a cutoff frequency of 10 Hz. The resulting models are discussed in the succeeding section.

Results

The FIR resulting FIR models are shown in figure; 4-2, 4-3, 4-4 and 4-5. These non parametric models will serve as a base for future parametric modeling.

Obtaining the noise model

Next, we can use these results to estimate the disturbance $v(t)$. By making use of equation 4-1, we obtain:

$$\hat{\mathbf{v}}(t) = \mathbf{y}(t) - \hat{\mathbf{G}}_N(q)w(t) , \quad (4-37)$$

where $\hat{\mathbf{v}}(t) = [v_\phi(t), v_\delta(t)]^T$ is the estimated disturbance and $\hat{\mathbf{G}}_N(q) = [\hat{G}_\phi(q), \hat{G}_\delta(q)]^T$ represents the obtained non parametric impulse response model from input $w(t)$ to output $\mathbf{y}(t)$.

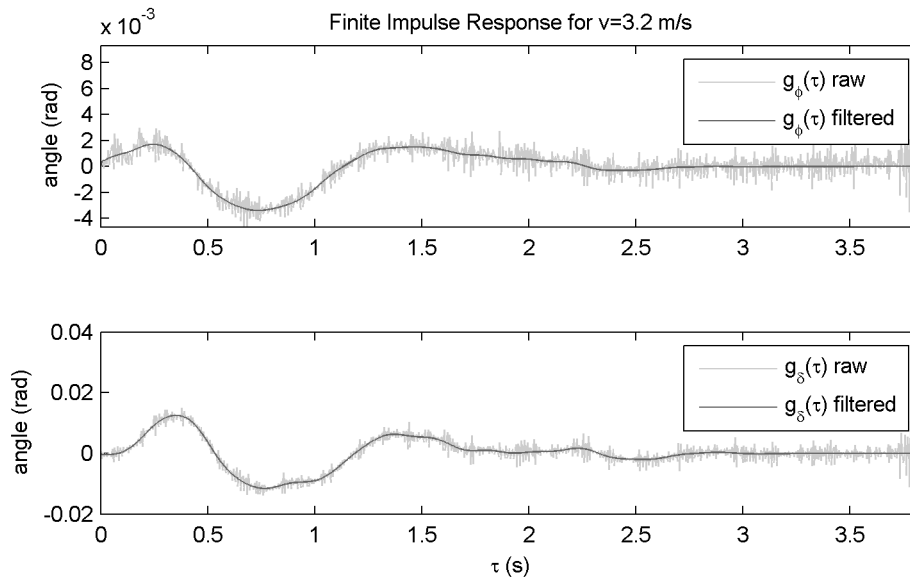


Figure 4-3: Impulse response model for the roll angle δ (top) and steering angle δ (bottom) for a forward velocity of $v = 3.2\text{m/s}$. The raw FIR model is smoothed using a low pass filtering with a cutoff frequency of 10 Hz.

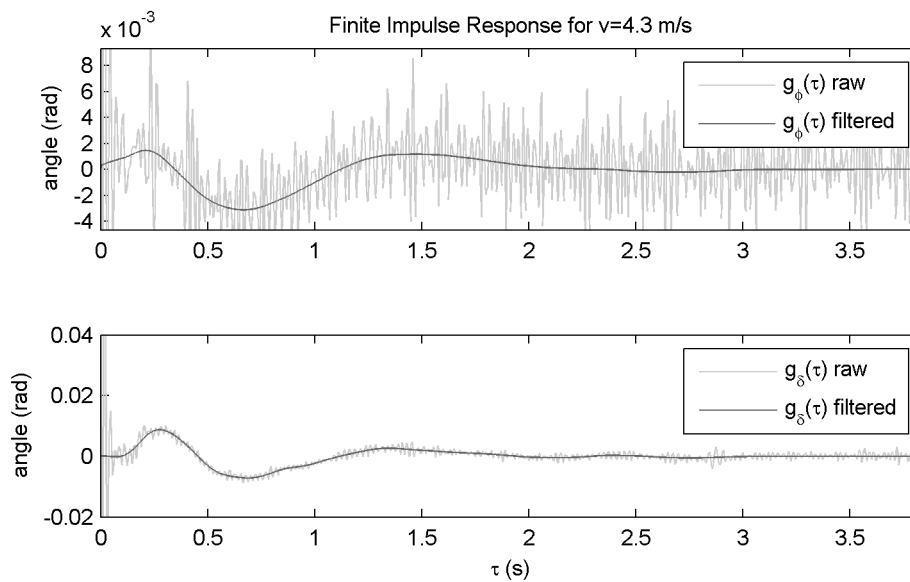


Figure 4-4: Impulse response model for the roll angle δ (top) and steering angle δ (bottom) for a forward velocity of $v = 4.3\text{m/s}$. The raw FIR model is smoothed using a low pass filtering with a cutoff frequency of 10 Hz.

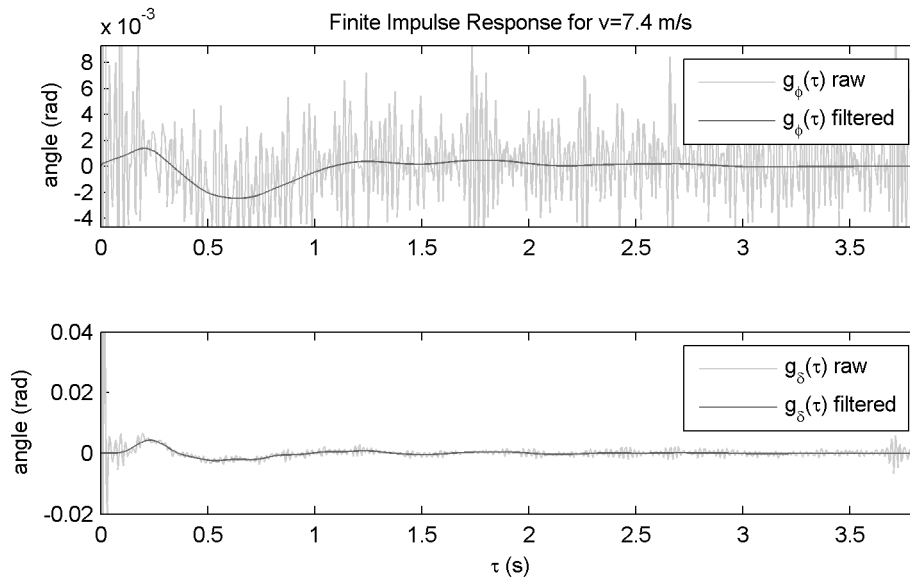


Figure 4-5: Impulse response model for the roll angle δ (top) and steering angle δ (bottom) for a forward velocity of $v = 7.4$ m/s. The raw FIR model is smoothed using a low pass filtering with a cutoff frequency of 10 Hz.

The decomposition of the measured data into the deterministic input related component and stochastic component is shown in figure 4-6. This noise model will turn out to be useful for designing a frequency domain experiment, which is discussed in the next chapter.

Some observations

When analyzing figure 4-2, 4-3, 4-4 and 4-5 a number of observations can be made:

- The high frequency noise is merely an artifact of the deconvolution process and does not originate from the rider/bicycle system itself.
- The 4th and 5th peak in both the roll and steering angle response, do not seem to be very likely and may be caused by noise.
- The signal to noise ratio for the case $v = 2.1$ m/s is very low, resulting in an unreliable FIR model.
- The signal to noise ratio of the steering angle response is generally of better quality than the roll angle response.
- The overall shape of the roll and steering angle responses are similar, but the amplitudes and time characteristics differ.
- The amplitude of the oscillation decreases as the forward velocity increases.
- The impulse response seems to damp out more quickly as the forward velocity increases.

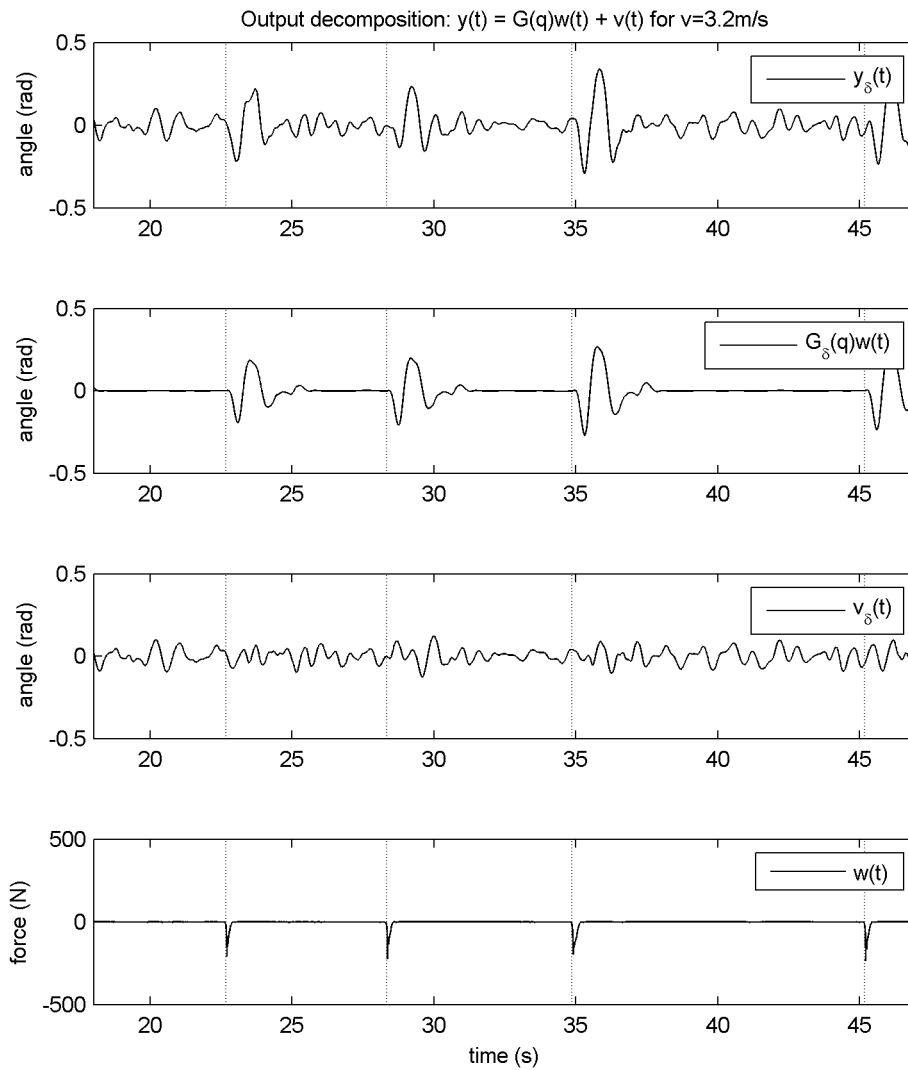


Figure 4-6: Output decomposition of the steering angle output $y(t)$ in terms of input related component $G(q)w(t)$ and remnant component $v(t)$ for a forward velocity of $v = 3.2\text{m/s}$.

The poor signal to noise ratio for lower velocities is something to remember, when designing an identification experiment. Here, more and longer measurements are advised to increase the signal to noise ratio.

4-2-2 Parametric Modeling

Next, the non parametric results will be used to estimate the parameters of the parametric model structure described in 2. We start of by reintroducing the parametric model structure, where the human controller is subject of identification. Secondly, we will formulate and solve the optimization problem, resulting in a set of parameters. Next, parameters space is reduced, such that only the important parameters remain.

Model Structure

Next we will use the general control structure presented in presented in chapter 2. By combining equations 2-34 and 2-19 we obtain the following parametric model structure:

$$\mathbf{y}(\boldsymbol{\theta}) = \mathbf{G}(\boldsymbol{\theta})\mathbf{w} , \quad \mathbf{G}(\boldsymbol{\theta}) = \left[\mathbf{P}_{yw} + \mathbf{P}_{yu} (\mathbf{I} - \mathbf{K}(\boldsymbol{\theta})\mathbf{P}_{yu})^{-1} \mathbf{K}(\boldsymbol{\theta})\mathbf{P}_{yw} \right] , \quad (4-38)$$

with bicycle dynamics \mathbf{P}_{yw} and \mathbf{P}_{yu} , human controller $\mathbf{K}(\boldsymbol{\theta})$, disturbance input $\mathbf{w} = w$ and output $\mathbf{y} = [\phi, \delta]^T$. Notice that only the human controller model is unknown, while the bicycle dynamics are known since they are determined a priori. To refresh our memory we shortly reintroduce the parametric human control model, which is described in section 2-2. The human controller is presented in equation 2-19, which yields:

$$\mathbf{K}(s) = G_{nm}(s)G_{\tau}(s) \begin{bmatrix} K_{\phi}(s) & K_{\delta}(s) \end{bmatrix} ,$$

with neuromuscular lag G_{nm} and time delay $G_{\tau} = e^{-s\tau_d}$ and where the roll and steering angle feedback is modeled according to equation 2-16:

$$\begin{aligned} K_{\phi}(s) &= k_{\phi p} + k_{\phi i} s^{-1} + k_{\phi d} s + k_{\phi dd} s^2 , \\ K_{\delta}(s) &= k_{\delta p} + k_{\delta i} s^{-1} + k_{\delta d} s + k_{\delta dd} s^2 . \end{aligned}$$

Here, the gains k are defined as the model parameters $\boldsymbol{\theta}$.

Parameter Estimation

Next, we will focus on the actual parameter estimation. We start of by introducing the error criterium, which we like to minimize by adjusting the parameters. Notice that our model has only one input and two outputs, which makes it a SIMO system. Let us rewrite the general control description into two separate SISO systems according to:

$$\mathbf{G}(\boldsymbol{\theta}) = \begin{bmatrix} G_{\phi}(\boldsymbol{\theta}) \\ G_{\delta}(\boldsymbol{\theta}) \end{bmatrix} . \quad (4-39)$$

We could choose to incorporate both outputs in the criterium by assigning weighting values to the separate output error criterium and sum these up. However, since the rider directly

excites the steering dynamics, it is expected that the steering angle contains the most direct information concerning rider action. In addition, the raw FIR model of the roll angle response contains a lot of noise, which makes it less reliable. Therefore, we choose to neglect the roll output and build the criterium function around the steering angle. In this case, a logical sum of squares output error criterium function would be:

$$V_N(\boldsymbol{\theta}) = \frac{1}{N} \sum_{t=1}^N \left[\left(\hat{G}_\delta(q) - G_\delta(q, \boldsymbol{\theta}) \right) w(t) \right]^2, \quad (4-40)$$

where the difference between the nonparametric and parametric models is weighted by the input signal w . The initial parameter vector $\boldsymbol{\theta}_0$ is determined by a random search method, for which the lowest criterium score is further optimized by using the `lsqnonlin` function. This function is specialized in minimizing non linear least square optimization problems and makes use of the trust region method. More information this method in particular and optimization in general can be found in Papalambros and Wilde (2000). The resulting fittings will be presented in the next subsection. The parameter optimization results in a optimal parameter vector set according to:

$$\hat{\boldsymbol{\theta}}_N = \arg \min_{\boldsymbol{\theta}} V(\boldsymbol{\theta}), \quad (4-41)$$

The parametric modeling is performed for several cases, where the forward velocity takes the following values: 2.1, 3.2, 4.3 and 7.4 m/s. A great number of initial parameter configurations where tried, but the models all turned out to be unstable. After evaluating and experimenting with various configurations, it turned out that the presence of time delay was causing these instabilities. Even for tiny time delays $\tau_d = 10^{-6}$, the system destabilized, where the undelayed system is perfectly stable.

This instability in the closed loop response is probably caused by the inverted rider term: $(\mathbf{I} - \mathbf{K}\mathbf{P}_{yu})^{-1}$, which is observed in equation (2-34). This inversion of the time delay, effectively results in a time preview, which mixes up causality and causes unstable behavior.

The problem is circumvented in two ways by:

1. Ignoring the time delay by setting it to zero.
2. Approximate the time delay by applying a second order Padé approximation.

the first case is achieved by simply setting $\tau_d = 0$ and the second by estimating the time delay according to:

$$e^{-\tau_d s} \approx \frac{1 + \frac{1}{2}z + \frac{1}{12}z^2}{1 - \frac{1}{2}z + \frac{1}{12}z^2}, \quad \text{with } z = -\tau_d s. \quad (4-42)$$

While the approximating seems valid for lower frequencies in the frequency domain (figure 4-7), the impulse response shows is poorly estimated (figure 4-8). Since the data is generated by a number of input impulses, the approximation should be evaluated critically.

After fixing the time delay problems, we also encountered some problems with obtaining a stable model for the $v = 2.1$ m/s case. Various parametric configurations where tried, but none of them led to a stable system response. This may be caused by the following causes:

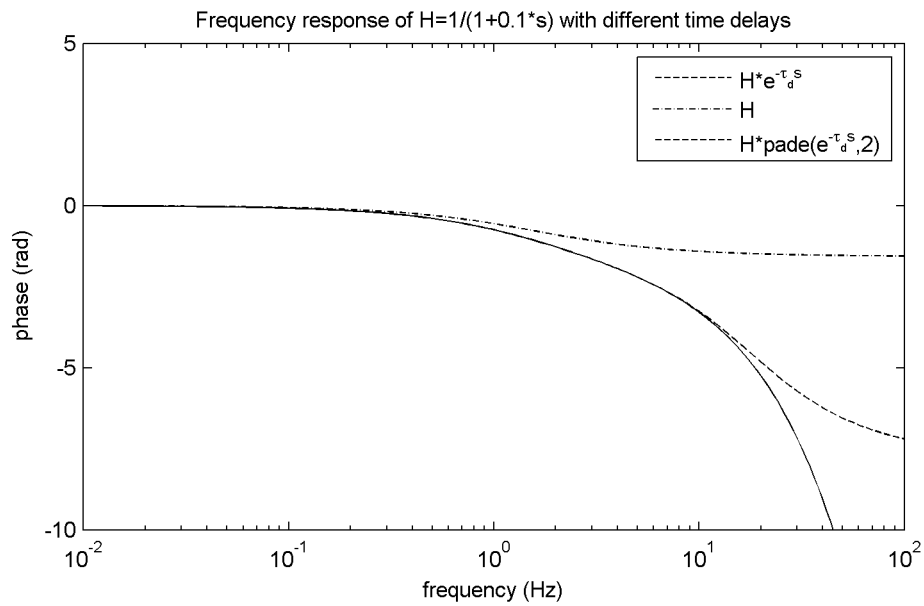


Figure 4-7: Frequency response of simple first order low pass filter $H(s) = 1/(1 + 0.1s)$ with different configurations for the time delay.

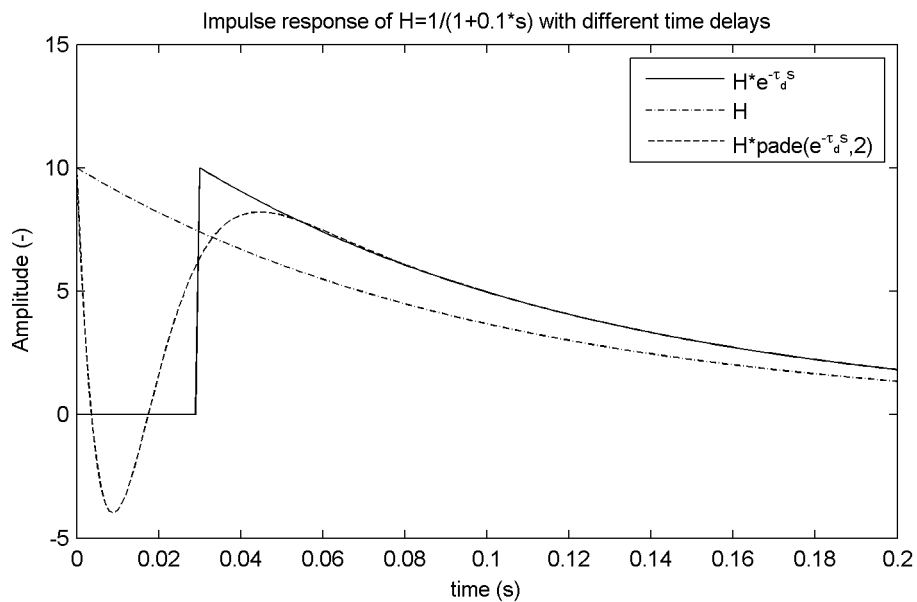


Figure 4-8: Impulse response of simple first order low pass filter $H(s) = 1/(1 + 0.1s)$ with different configurations for the time delay.

- The FIR model for $v = 2.1$ m/s is of poor quality, which affects the parametric modeling, because it is based on the nonparametric results.
- The uncontrolled system dynamics are highly unstable at low forward velocities. Here the unstable oscillatory weave mode dominates the system dynamics, which may be hard to control.

Next, we analyze the parametric results that did work out. Figure 4-9 shows the time domain results for the parametric results for forward velocities of 3.2, 4.3 and 7.4 m/s. Table 4-1 shows the obtained parameter values for the case when τ_d is set to zero. Figure 4-10 shows the impulse response functions for both the roll and steering angle response. From figure 4-9 we see that the measured steering response characteristics are being well matched by the model response. Although the parametric model is fitted purely onto the steering angle responses, we observe from figure 4-10 that the general characteristics of the roll angle response are also fitted reasonably well. The three models show high VAF values of above 96%, which is quite impressive. The largest errors occur at the second and highest peak of the impulse response, for which the parametric model peak is lower than the nonparametric model.

Remark; at this point we haven't taking into account the parameter uncertainty, which may explain for major differences between measurements, where similarities where expected. Therefore these results are considered to be preliminary and still unreliable. In the next subsection we will use the parameter covariance to further reduce our parametric model while maintaining high VAF values.

Parameter Reduction

Next, we will try to reduce the parameter space, while maintaining high VAF values. To check whether there is a redundancy in these parameters, we will eliminate the parameters one by one. Typically, we are looking for a minimum set of parameters, without causing a big drop in the VAF value.

One way to achieve this would be to try eliminating the parameter one by one for each reduction step, after which the parameter that causes the smallest drop in VAF will be permanently eliminated. The process is then repeated until there are no parameters left or until the VAF drops dramatically. However, a full reduction sequence (in the case of 8 parameters) would require $8! = 40320$ optimizations, which is rather a lot since it may require manual operations.

A more efficient method would be to first eliminate the parameter that affects the error criterium the least. It can be shown that this is the same as eliminating the parameter with the largest variance, which already introduced in section 4-1-6 and derived in D. The parameter covariance is normalized first, by introducing a set of normalized parameters according to:

$$\hat{\theta}_i = \theta_i / \hat{\theta}_i^N, \quad (4-43)$$

where $\hat{\theta}_i^N$ is the fixed optimum parameter and θ_i is the non-normalized parameter. So at the found optimum, the normalized parameters are all equal to 1 and dimensionless. This makes the indices of the parameter covariance comparable with each other and allows for reduction techniques. The diagonal terms of the covariance matrix represent the auto variance, which

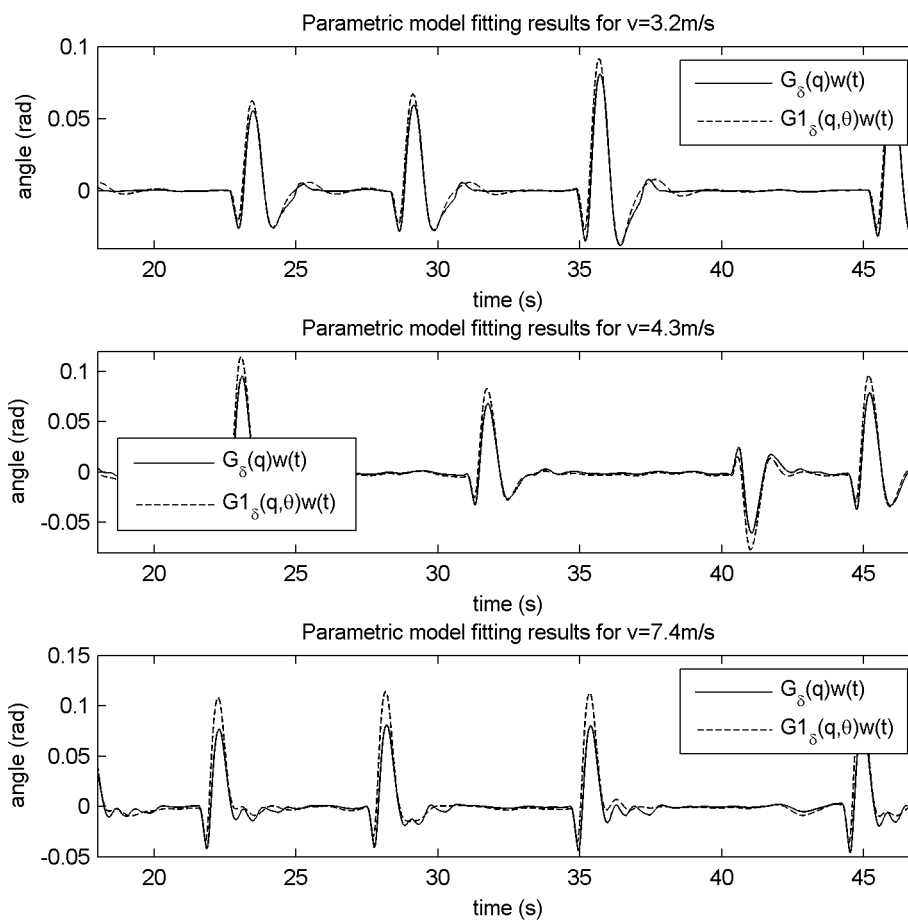


Figure 4-9: Parametric model results for $\tau = 0$

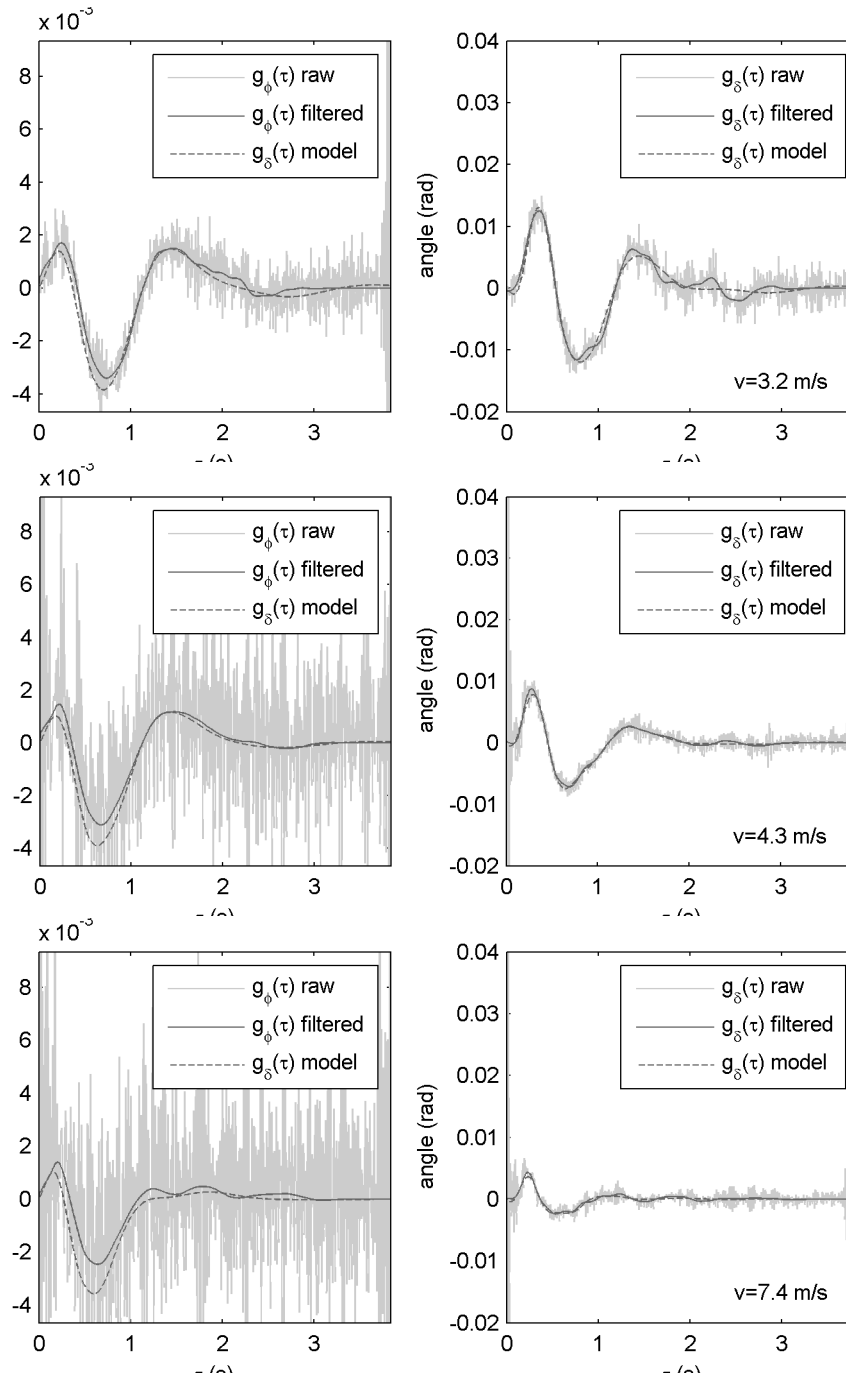


Figure 4-10: Parametric model impulse responses projected onto the FIR model for $\tau = 0$

is a measure for parameter uncertainty. A large auto variance means that the parameter is poorly estimated. In this case, the corresponding parameter forms a suitable candidate for elimination, since it contributes relatively little to the error criterion function defined in equation 4-40.

Next we will present a reduction scheme, which is based on the normalized parameter auto variance. For each reduction step, the parameter with the largest auto variance is eliminated by setting it to zero. The parameter optimization described in section 4-2-2 is then repeated for the reduced set of parameters. Next, the parameter covariance matrix for the reduced set of parameters is estimated, after which another parameter is eliminated. This process is repeated until the VAF drops dramatically (below 50%), since the results do not make sense anymore.

Figures 4-11, 4-12, 4-13 and 4-14 show the iterative normalized parameter covariance results. The corresponding parameters and VAF values are presented in table 4-1. These results will be discussed in the next section.

Remark; the covariance theory assumes an error which is according to a white noise distribution. However, since we removed the noise at an early stage (non-parametric modeling) these assumptions do not hold and result in an underestimation of the true parameter covariance. This is not an issue for the parameter reduction, since only the relative covariance is of importance here and not the absolute (underestimated) covariance. Later on we will derive the unbiased covariance for the frequency domain by using a separate noise model and analytic parameter sensitivity expressions.

Finally, we present the impulse response function for the reduced parametric model at $v = 3.2$ m/s, for which the specific gain contributions are calculated. These results are shown in figure 4-15 and will be discussed in the next section.

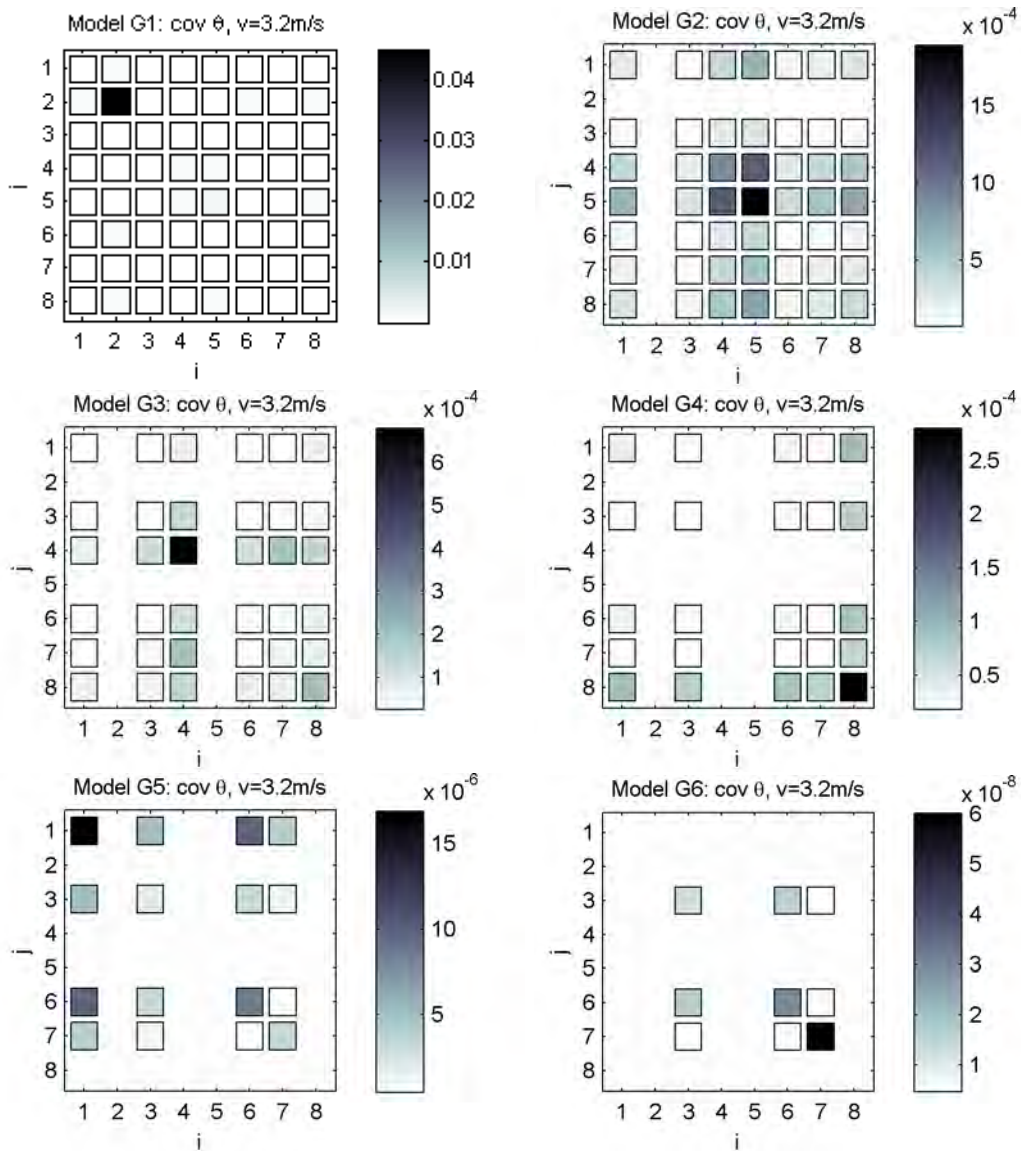


Figure 4-11: Subsequent parameter covariance matrices after iterative parameter reduction. The parametric model is based on a forward velocity of $v = 3.2$ m/s and the time delay is set to $\tau_d = 0$. The parameter space is reduced by one for each iteration until the VAF value drops down dramatically.

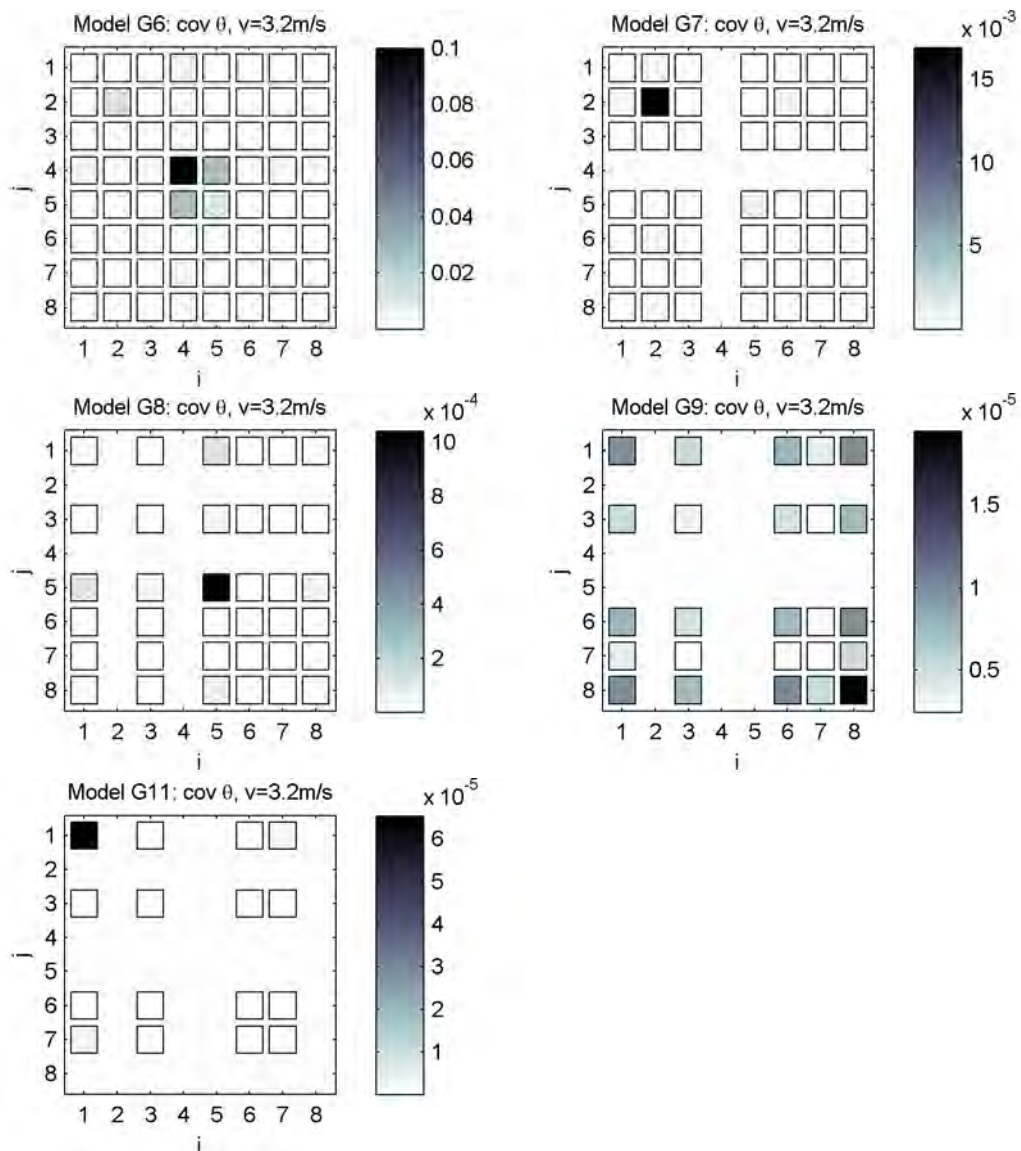


Figure 4-12: Subsequent parameter covariance matrices after iterative parameter reduction. The parametric model is based on a forward velocity of $v = 3.2$ m/s and the time delay is estimated using a 2nd order Pade approximation. The parameter space is reduced by one for each iteration until the VAF value drops down dramatically.

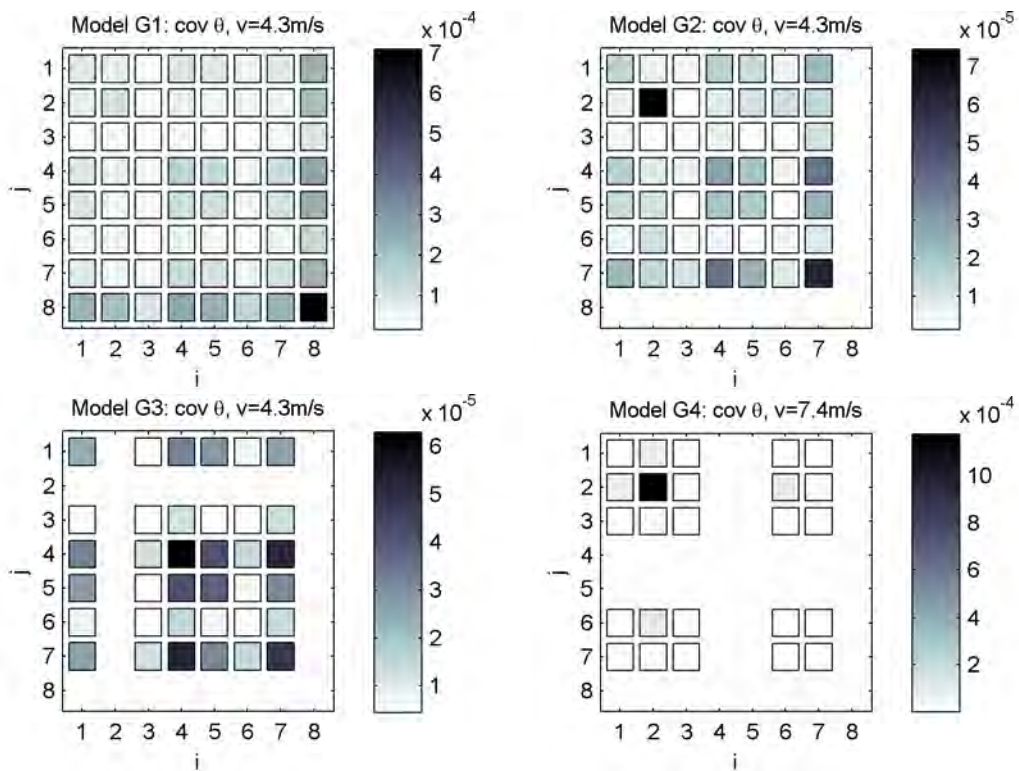


Figure 4-13: Subsequent parameter covariance matrices after iterative parameter reduction. The parametric model is based on a forward velocity of $v = 4.3$ m/s and the time delay is set to $\tau_d = 0$. The parameter space is reduced by one for each iteration until the VAF value drops down dramatically.

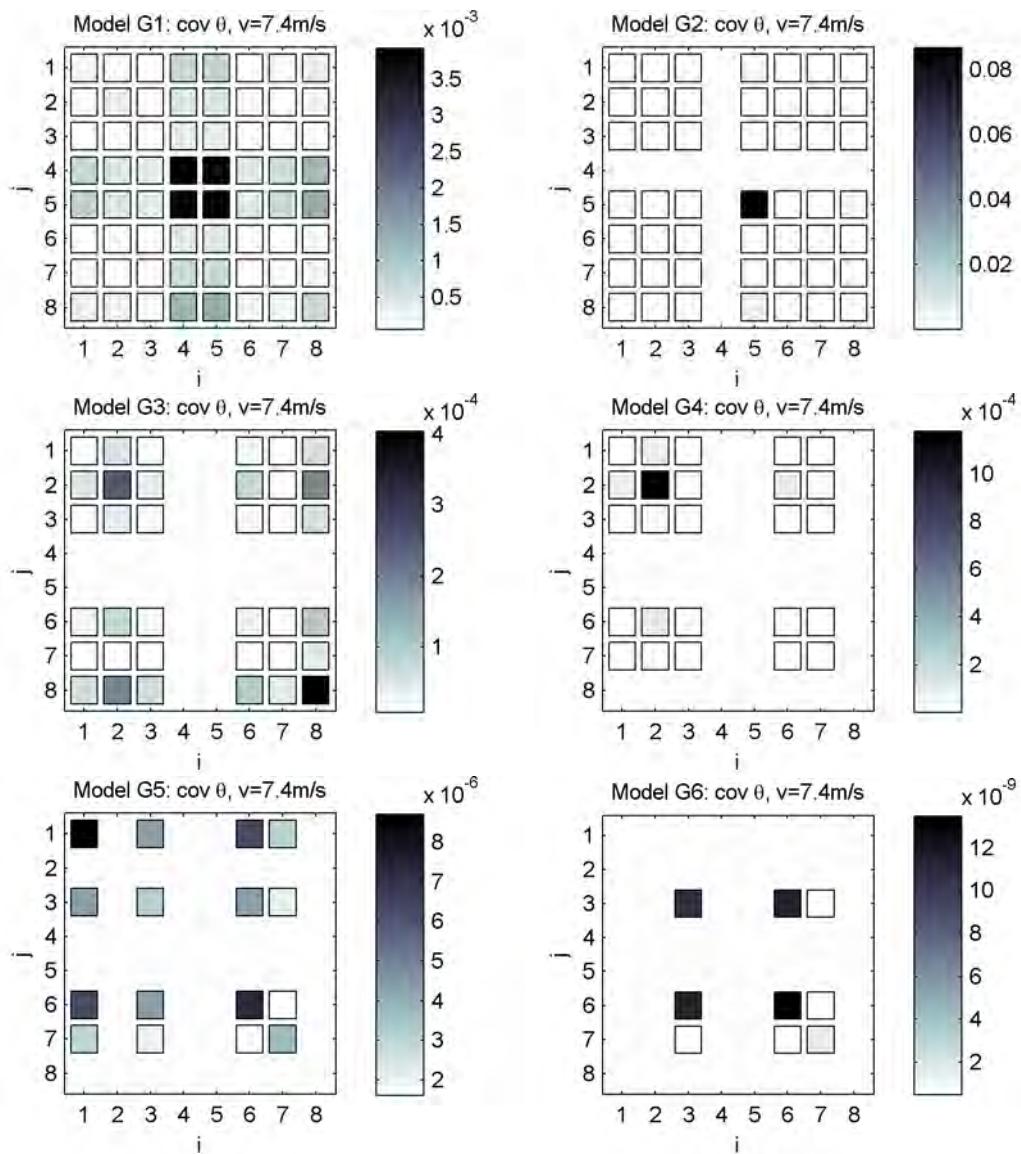


Figure 4-14: Subsequent parameter covariance matrices after iterative parameter reduction. The parametric model is based on a forward velocity of $v = 7.4$ m/s and the time delay is set to $\tau_d = 0$. The parameter space is reduced by one for each iteration until the VAF value drops down dramatically.

Model	τ_d	$k_{\phi p}$	$k_{\phi i}$	$k_{\phi d}$	$k_{\phi dd}$	$k_{\delta p}$	$k_{\delta i}$	$k_{\delta d}$	$k_{\delta dd}$	VAF
$\mathbf{K}(s, \theta(v = 3.2))$	0.00	81.41	-7.68	57.99	-1.98	-8.10	182.73	-6.98	-0.21	97.56
	0.00	79.48		57.50	-2.00	-8.19	177.40	-6.99	-0.20	97.56
	0.00	54.66		50.20	-0.87		147.99	-5.30	-0.13	97.33
	0.00	52.18		43.51			131.94	-3.97	-0.14	97.09
	0.00	36.81		32.99			89.45	-3.25		94.24
	0.00			32.80			90.91	-1.72		0.00
	0.03	67.32	-11.18	48.26	0.13	-2.69	151.70	-4.99	-0.27	97.73
	0.03	69.15	-9.87	49.03		-3.41	153.84	-5.18	-0.27	97.73
	0.03	66.53		48.41		-3.38	147.06	-5.17	-0.27	97.71
	0.03	57.92		49.67			146.22	-5.22	-0.24	97.52
0.03	-18.19		53.42			350.97	-3.47		0.00	
$\mathbf{K}(s, \theta(v = 4.3))$	0.00	44.93	-56.22	39.65	1.16	16.25	277.79	-3.10	-0.05	99.31
	0.00	29.98	-40.27	33.78	1.60	21.72	222.31	-2.05		99.26
	0.00	29.58		33.79	1.26	17.08	195.40	-2.74		98.75
	0.00	299.44		0.87		-54.16	-446.57	-16.06		0.00
$\mathbf{K}(s, \theta(v = 7.4))$	0.00	97.95	-128.03	58.78	-0.63	-30.42	1424.31	-14.10	-0.19	96.15
	0.00	77.81	-108.86	51.84		-1.34	1230.16	-11.43	-0.13	96.12
	0.00	76.54	-108.23	51.83			1226.80	-11.44	-0.12	96.11
	0.00	62.40	-42.25	42.19			886.86	-10.34		95.25
	0.00	59.20		41.56			816.11	-10.56		95.06
	0.00			68.98			1372.49	-19.47		0.00

Table 4-1: Overview of parametric modeling results, with controller \mathbf{K} , parameter vector θ , forward velocity v (m/s), time delay τ_d (s), roll proportional gain $k_{\phi p}$ (Nm/rad), roll integrative gain $k_{\phi i}$ (Nm/s rad), roll derivative gain $k_{\phi d}$ (Nm s/rad), roll 2nd derivative gain $k_{\phi dd}$ (Nm s²/rad), steer proportional gain $k_{\delta p}$ (Nm/rad), steer integrative gain $k_{\delta i}$ (Nm/s rad), steer derivative gain $k_{\delta d}$ (Nm s/rad), steer 2nd derivative gain $k_{\delta dd}$ (Nm s²/rad) and Variance Accounted For VAF (%). The marked rows represent the selected reduced parametric models, which are used for further analysis. The marked rows indicate the reduced parametric models which are used for further analysis.

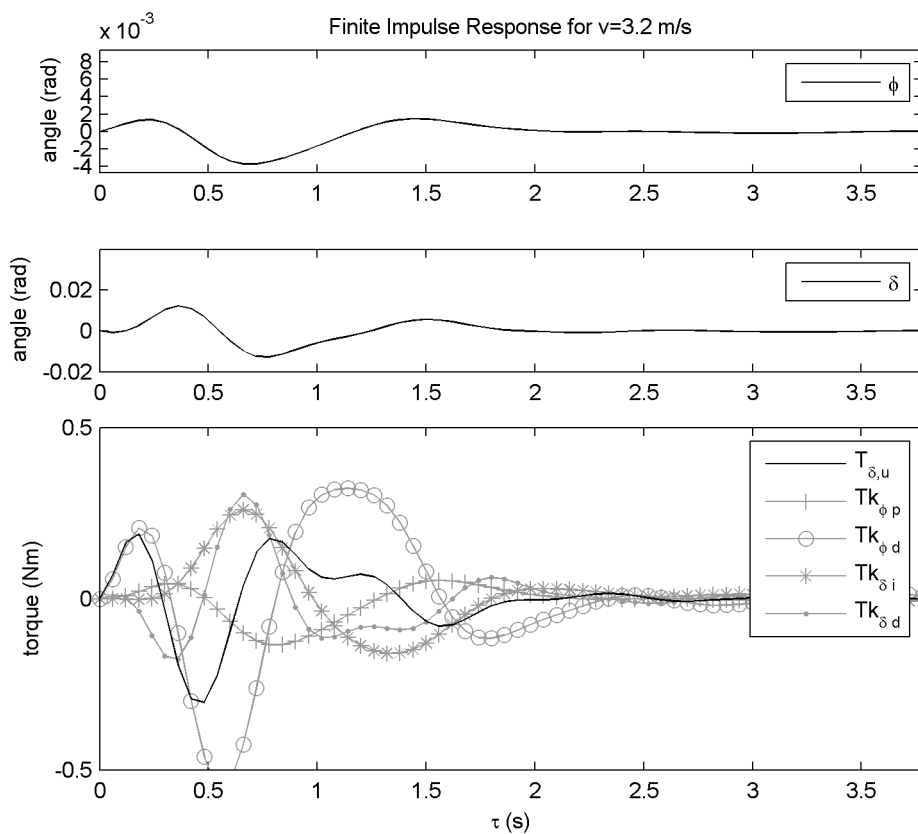


Figure 4-15: Impulse response of the parametric model. Top: roll angle response. Middle: steering angle response. Bottom: steering torque response, decomposed into the separate gain parameter contributions.

4-3 Analysis

In this section the resulting parametric models are further analyzed. First an eigenvalue analysis is performed for the reduced rider models where the time delay is omitted ($t_d = 0$ s). In addition, some observations concerning the parametric results are made, for which possible explanations are introduced and discussed.

4-3-1 Eigenvalue analysis

The eigenvalues for the selected reduced parametric models are all calculated and shown in table 4-2. The positive part of the resulting eigenvalues are all negative, which indicates stability. Further more we observe that the state has increased from 4 to 7 dimensions. Here, one state is added due to the integrative feedback action on the steering angle. The other two states are added due to the neuromuscular activation dynamics G_{nm} , which acts as an second order low pass filter on the controller output.

	$\mathbf{K}(s, \boldsymbol{\theta}(v = 3.2))$	$\mathbf{K}(s, \boldsymbol{\theta}(v = 4.3))$	$\mathbf{K}(s, \boldsymbol{\theta}(v = 7.4))$
λ	-22.76	-25.08	-36.57
	-1.70 -11.53 <i>i</i>	-2.31 -13.12 <i>i</i>	-2.18 -17.86 <i>i</i>
	-1.70 11.53 <i>i</i>	-2.31 13.12 <i>i</i>	-2.18 17.86 <i>i</i>
	-1.40 -5.25 <i>i</i>	-1.88 -5.76 <i>i</i>	-1.93 -7.26 <i>i</i>
	-1.40 5.25 <i>i</i>	-1.88 5.76 <i>i</i>	-1.93 7.26 <i>i</i>
	-1.16 -2.60 <i>i</i>	-0.99 -2.99 <i>i</i>	-1.27 -2.91 <i>i</i>
	-1.16 2.60 <i>i</i>	-0.99 2.99 <i>i</i>	-1.27 2.91 <i>i</i>

Table 4-2: Closed loop eigenvalues $\lambda = \text{eig}(\mathbf{G}(s, \boldsymbol{\theta}))$ for the selected reduced parametric models, where τ_d is set to zero.

4-3-2 Observations

When analyzing the parametric results, the a number of observations are made, for which possible explanations are discussed. However, again we'd like to point out, that the parameter uncertainty is underestimated, therefore no hard conclusions should be made concerning the exact parameters. However the reduced parameters models seem to converge seemingly well, making them the most interesting to compare between different measurements. When analyzing table 4-1 the following observations can be made:

- The steer into the fall principle is observable in the positive roll angle and rate feedback for all measurements. From figure 4-15 we observe that the roll perturbation only results in a initial roll velocity. Therefore, the roll rate feedback dominates the initial response, which is key to stabilizing the system. At $t = 0.2$ s the roll angle reaches an initial peak, for which the roll feedback gain start to kick in. The combined roll angle and rate feedback result in the stabilizing steer into the fall mechanism, which is also described in section 2-1-3.

- The roll angle, roll rate, steering rate and integral action are the key contributors and cannot be removed without causing a major drop of the VAF value for any case. Removal of any of these parameters results in instability, which is no feasible result, since the measured bicycle/rider configuration is observed to be stable.
- Parameter reduction affects the parameter values relatively to the unreduced parameters, but all the signs remain conserved. This is probable due to the off-diagonal terms observed in the parameter covariance matrices, which indicate parameter dependency. If a parameter is removed, the dependent parameters may fill up the empty parameter space, which may explain for the parameter variations through the reduction steps. This might be solved by introducing an orthogonal parameters set, for which the least contributing parameters can be eliminated, without affecting the other parameters due to orthogonality.
- The integrative steer action acts as a negative super-spring (integral of spring force over time) on the steering angle. Analysis of the bicycle equations shows that this time integral of the steering angle is roughly proportional to the heading angle. This can be shown integration of equation 2-3, which describes the heading rate of the bicycle:

$$\dot{\psi} = \frac{v\delta + c\dot{\delta}}{w} \cos(\lambda) . \quad (4-44)$$

for which the heading is obtained through integration over time and can be approximated by elimination of the relatively small steering rate terms:

$$\psi = \int \frac{v\delta + c\dot{\delta}}{w} \cos(\lambda) dt , \quad (4-45)$$

$$\psi \approx \frac{v}{w} \cos(\lambda) \int \delta dt \quad (4-46)$$

From this we observe that steering integral action acts proportionally to the heading angle. As the heading angle increases, the rider exerts more steering torque in the same direction. By doing so, the rider effectively applies a counter steering action mechanism, resulting in a turn in the other direction. Concludingly, the steering integral action acts as controller on the heading angle. This heading control is necessary, since the experiment was performed on a rather narrow horse treadmill, allowing only for little changes in heading and lateral displacement.

- The parameter reduction method increases the VAF/number-of-parameters ratio significantly. However, reducing the parameter space too much leads to instability, resulting in near zero VAF values. Apparently, the remaining parameters are crucial to bicycle stability.
- The presence of time delay only results in a minor increase of VAF. However, it does affect the value of the estimated parameters significantly. When comparing the reduced set of parameters, shown in table 4-1 and measured at $v = 3.2\text{m/s}$ (same experiment) for both cases, we observe changes of up to 30% between similar parameters. Apparently the absence of time delay, is being compensated by adjusting the parameters.

These parametric results will prove to be useful in subsequent analysis, where a frequency domain experiment will be set up.

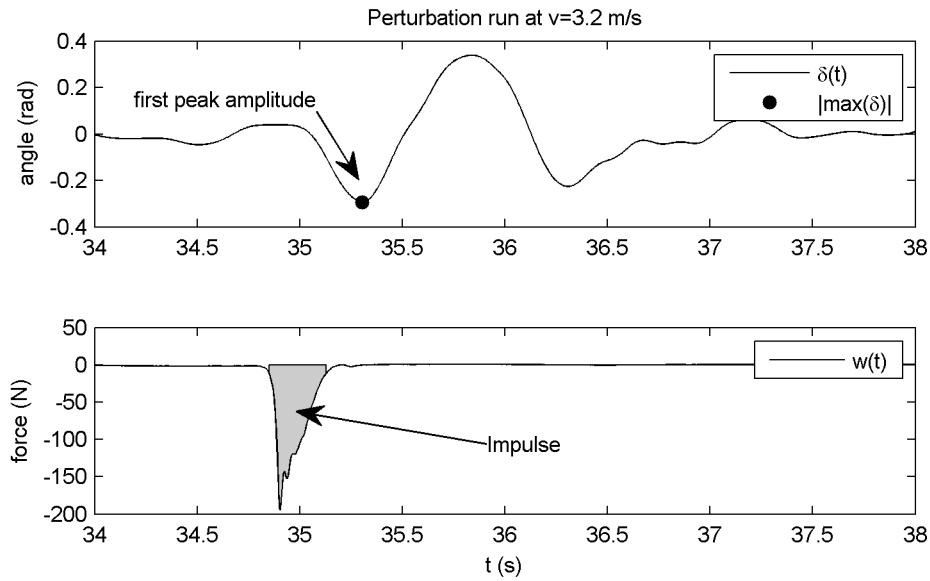


Figure 4-16: Resulting first peak output response of the steering angle due to perturbation impulse. The net impulse is estimated by calculating the shaded area of the force perturbation.

4-3-3 Non-linear scaling check

Next, we will check whether the system output scales linearly with the input power. This is done by analyzing the ratio between the net impulse and corresponding steering angle peak response for each separate perturbation. First, we obtain a measure of the net impulse by numerical integration of the force for each impulse. Next, we derive the first peak amplitude of the corresponding steering angle response. A simple Matlab algorithm is written to automatically perform these operations, for which an example result is shown in figure 4-16. The resulting first peak response versus net impulse is shown in figure 4-17. The check is also performed for other forward velocities, for which the results looked more or less the same. From this initial check, it appears that the linear scaling approximation holds reasonably well. However, since the noise levels are rather high, more experiments with varying input amplitudes are recommended.

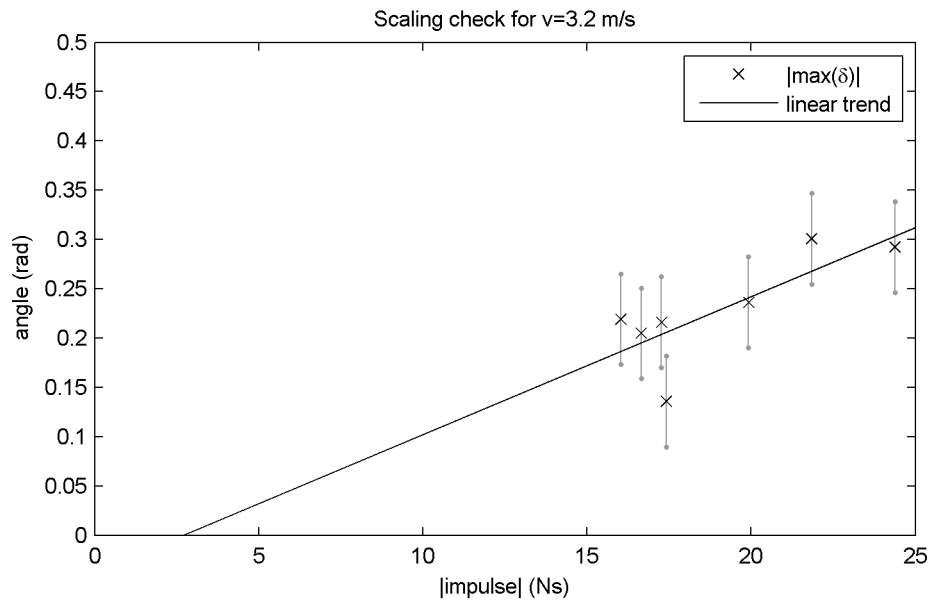


Figure 4-17: Resulting first peak output response of the steering angle versus net impulse. The standard deviation of the output response is indicated with the gray vertical lines and indicates uncertainty. For a linear system this relationship should scale linearly, which appears to be roughly the case. Notice that the trend line does not fully intersect with the origin, which may either be due to noise or non linearity.

4-4 Summary

First, a limited amount of system identification theory is presented, which focuses mainly on linear time and frequency domain methods. The output data can be decomposed using nonparametric techniques into a part which can be linearly correlated to the input and an uncorrelated part called the the remnant. These nonparametric results are often used as a noise reduced model, which may serve as a base for parametric model identification. The parametric model identification requires a data set, model structure and error criterium, for which a optimal parameter set can be found using optimization algorithms.

Next, nonparametric methods are applied onto the obtained experimental dataset, which is introduced in the previous chapter. The analysis is performed for different forward velocities of 2.1, 3.2, 4.3 and 7.4 m/s. A non parametric FIR model is chosen to obtain the noise reduced input related response, and is obtained for both the roll and steering angle response with the force disturbance being the input. The obtained roll responses where of all of poor quality, rendering these useless for subsequent analysis. Fortunately, the impulse response models for the steering angle response where of much better quality. The shape of FIR responses shows a lot of similarity, but the amplitude and time characteristics seem to change as a function of the forward velocity v . In addition, a noise model is also obtained, which will prove to be useful in subsequent chapters.

Finally, the nonparametric models serve as a noise reduced base for the parametric models presented in chapter 2. These models are fitted by minimizing the sum of errors squared between the non parametric and parametric steering angle responses. There where stability

issues with the time delay, which is solved by setting it either to zero or by Pade approximation. After fixing the stability issue, the resulting VAF values are around 97% for different forward velocities, which is quite good. The parameter space is reduced by eliminating the least contributing parameters. By doing so, the parameter space is reduced from 8 up to 4 parameters, while the VAF only drops from 97.56 to 94.24 % for the $v = 3.2$ m/s case. When analyzing the reduced parameter results we make the following observations:

- The steer into the fall principle is observable in the positive roll angle and rate feedback for all measurements.
- The roll angle, roll rate, steering rate and integral action are the key contributors and cannot be removed without causing a major drop of the VAF.
- The integrative steering action controls the heading by applying counter steering.

The nonparametric and parametric results will prove to be useful in subsequent analysis, where a frequency domain experiment is set up.

Experiment Design

Now that we have obtained a model of the rider action, we can start setting our own frequency domain experiment. This frequency domain experiment allows for frequency domain methods, which provides certain advantages over time domain methods. For example, exciting the system by using multi sine perturbations allows for specific control of the input bandwidth and power.

This chapter starts by stating the goal of experiment design. Next, a number of possible closed loop identification methods are presented. Secondly, the measurement settings are determined, which include settings such as the measurement time and sampling frequency. Thirdly, a multisine input signal will be defined in terms of spectral and spatial excitation. The next section focuses on some important issues concerning man machine identification experiments. Finally, a simulation study is set up to check whether the designed experiment is truly informative enough.

5-1 Goal

The goal of experiment design is to generate an informative dataset on which system identification procedures are applied. The dataset is said to be informative when the characteristics of the system subject to identification are well observable in the generated data. Since we are interested in parametric modeling, we like to estimate these parameters as accurate as possible. This means a low (normalized) parameter variance matrix, which is a measure for the accuracy of the estimated parameters with respect to the true parameters. The inverse of this parameter covariance matrix is known as the Fisher information matrix. So minimizing the parameter covariance is equal to maximizing the information matrix. The volume of the information matrix is given by its determinant, which is a measure for the available information. In short; creating an informative experiment is done by maximizing the determinant of the information matrix. Or in terms of the covariance; by minimizing the determinant of the normalized parameter covariance. More information on this subject can be found in Ljung (1987).

5-2 Closed loop identification methods

Next we analyze closed loop identification methods according to Ljung (1987). Lets start of by reintroducing the general control block description from chapter 2, which is shown in figure 5-1. From this we observe that the 'unknown' human controller \mathbf{K} acts as a closed

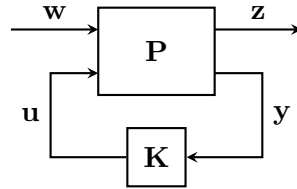


Figure 5-1: Block diagram of the general control description, with known bicycle dynamics \mathbf{P} , unknown controller \mathbf{K} , disturbance input \mathbf{w} , error output $\mathbf{z} = -\phi$, control input \mathbf{y} and control output \mathbf{u} .

loop regulator, which requires closed loop methods for the identification process. According to Ljung (1987), there are three possible methods for estimating a closed loop regulator, namely:

1. The Direct Approach: Apply the basic prediction error method in a straightforward manner: use the rider input \mathbf{y} and output \mathbf{u} in the same way as for open loop operation, ignoring any possible feedback, and not using the external input \mathbf{w} .
2. The Indirect Approach: Identify the closed loop system from external input \mathbf{w} to output \mathbf{y} , and retrieve from that the open loop system, making use of the known bicycle dynamics.
3. The Joint Input-Output Approach: Consider \mathbf{y} and \mathbf{u} as outputs of a system driven by \mathbf{w} (if measured) and noise. Recover knowledge of both the system \mathbf{P} and regulator \mathbf{K} from this joint model.

Method 2 only requires measurement of the external input \mathbf{w} and bicycle output \mathbf{y} in combination with knowledge of the bicycle dynamics. Fortunately, the bicycle equations are well established, which makes this method easy to implement. However, since this method estimates the parameters indirectly, the parameters sensitivity is generally poorer compared to direct methods, such as method 1 and 3. While these direct methods are more sensitive in the parameters, these also require measurement of both the rider input \mathbf{u} and output \mathbf{y} . Method 1 can be used to estimated the controller \mathbf{K} directly, without knowledge of the external input \mathbf{w} . Method 3 can be used to estimate both the system \mathbf{P} and controller \mathbf{K} , whenever the external input \mathbf{w} is known.

Methods 1 and 3 require rider output \mathbf{u} , for which measurements are experienced to be troublesome (van den Ouden, 2011). On the other hand, we have a pretty solid model of the bicycle dynamics \mathbf{P} , which is required by method 2. Despite the reduced parameter sensitivity, the indirect approach (method 2) is chosen, because of the relative easy implementation. Later on, we will quantify the parameter observability, to assure our experiment is informative enough.

Concludingly, method 2 is the preferred method, where \mathbf{y} and \mathbf{w} are obtained from experiment and \mathbf{P} should be determined a priori.

5-3 Frequency domain identification method

In this section a frequency domain identification method is proposed. The identification procedure will split up into a non parametric model identification and parameteric model identification. The approach is method will be similar to the one described in section 4-2, but now we introduce frequency domain methods in stead of time domain methods. Since the rider action is presumably observable in the steering angle response, we will perform the identification onto the steering angle response only, so $G = G_\delta$.

Next, we shorly restate the most important frequency domain expressions, which are already introduced in chapter 4. Lets start of with the non parametric frequency domain response, which is given by:

$$\hat{G}_N(e^{i\omega}) = \frac{\hat{\Phi}_{yw}^N(\omega)}{\hat{\Phi}_w^N(\omega)}. \quad (5-1)$$

In this case, the estimated transfer function can be used to estimate the disturbance spectrum, according to:

$$\hat{\Phi}_v^N(\omega) = \hat{\Phi}_y^N(\omega) - |\hat{G}_N(e^{i\omega})|^2 \hat{\Phi}_w^N(\omega). \quad (5-2)$$

These results serve as an base for the parametric modeling, for which the common frequency domain criterium is given by:

$$V_N(\theta) = \frac{1}{N} \sum_{k=1}^N \left| \hat{G}_N(e^{i\omega_k}) - G_N(e^{i\omega_k}, \theta) \right|^2 \frac{\hat{\Phi}_u^N(\omega_k)}{\hat{\Phi}_v^N(\omega_k)}, \quad (5-3)$$

which corresponds to a optimization problem for which an optimal parameter can be found according to:

$$\hat{\theta}_N = \arg \min_{\theta} V_N(\theta), \quad (5-4)$$

and for which the parameter covariance yields:

$$\text{cov } \hat{\theta}_N = \frac{1}{N} \left[\sum_{k=1}^N G_{,\theta}^T(e^{i\omega_k}, \theta) \frac{\hat{\Phi}_w^N(\omega_k)}{\hat{\Phi}_v^N(\omega_k)} G_{,\theta}(e^{i\omega_k}, \theta) \right]^{-1}. \quad (5-5)$$

This covariance expression is something which we like to minimize, since a smaller covariance results in to a more accurate set of parameters.

5-4 Measurement settings

The measurement settings consist of the sampling frequency f_s and measurement time T . Together they determine the number of measured samples N according to:

$$N = T/F_s \quad (5-6)$$

From a computational point of view, it would be nice if N would be some power of 2, since that allows for the most efficient IFFT.

The measurement frequency forms an upper bound for the maximum observable frequency, which is simply calculated as:

$$f_n = f_s/2, \quad (5-7)$$

where the upper bound f_n is called the Nyquist frequency. As a rule of thumb, this frequency should be 10 times higher than the highest system dynamics of interest. Since the fastest human control dynamics are roughly around 3 Hz, the sampling frequency should be at least 60 Hz. However, since storage capacity is not a real issue anymore, we set the sampling frequency to 200 Hz, which definitely should be high enough.

The measurement time determines the frequency resolution and also the accuracy of the measurements. When analyzing the covariance expression stated in equation 5-5, we observe that the covariance is proportional to $1/N$. Since T is proportional to N , the covariance indeed decreases for longer measurements. However, longer measurements are also more sensitive to time varying systems. These time variant behavior may very well occur in man-machine interactions. For example, after a while the human controller may optimize its control strategy, which is called the learning effect. In addition, psychological phenomena like tiredness, boredom, etc. may also occur if the measurements are taking too long. We think that a reasonable measurement time would be around $T = 180$ s, which corresponds to three minutes of active bike balancing.

In section 2-2 we stated that the parameters are a function of the forward velocity. We also know from section 2-1 that the bicycle dynamics change as a function of the forward velocity. The major changes in bicycle dynamics typically take place between 3 and 6 m/s. To safely encapsulate these interesting changes in dynamic behavior, the experiment should be performed at forward velocities between 2 and 7 m/s with a 1 m/s interval.

5-5 Input signal design

Next we will focus on designing a proper input signal. This signal should be designed such that an informative dataset is generated. The following points should be considered when designing an input signal:

1. Spectral excitation: the input frequency bandwidth should be chosen such that it excites the human controller action sufficiently.
2. Spatial excitation: the input should be placed such that it excites the interesting system dynamics.
3. The input power should be scaled such that a good signal to noise ratio is achieved, while maintaining reasonable safety margins.
4. The input signal should appear to be random to the human controller, in order to prevent possible feed forward control.

A particular signal type which fulfills these requirements is given by the crested multi sine. This signal may be constructed in the frequency domain by specifying input power as a function of frequency. An algorithm then optimizes the phase such that a minimal crest factor (peak to average power ratio) in the time domain is achieved. This frequency domain signal is then transformed to the time domain using an inverted Fourier transformation. This results in the desired input signal which can be used for simulations and experiments.

5-5-1 Random multi sine

According to R. Happee, a randomly appearing signal can be created by superimposing 5 or more sines at different frequencies. For this experiment a multi sine consisting of 10 sines will be used to excite the system. These frequencies should lie on the frequency grid, which is formed by an integer number times the frequency resolution $\Delta f = 1/T$. The multi sine should be crested, which that means that the phase is optimized such that the resulting peak to average ratio is low. More information about input signals in general and crested multi sine generation can be found in the appendix B.

5-5-2 Spatial excitation

Next we analyze the spatial placement of the input signal. From chapter 2 we know that the bicycle has two generalized inputs, namely generalized roll and steering torque. Therefore, in order to estimate the complete system, we should apply at least two inputs en perform two measurements. However, since we are particularly interested in roll stabilization, we will only focus on that part of the system which corresponds to the external roll torque response. In addition, the steering disturbance is less interesting, since it could be affected by applying co-contraction. By using co-contraction, the human controller is physically capable of creating an effective spring and damper acting on the relative steering angle, which makes the control rather trivial and less interesting. While steering torque input may trigger co-contraction, the roll torque input does not, because the human controller has no physical means to create an effective spring and damper acting on the roll angle. So the spatial excitation consist of one output $w(t)$, which exerts the bicycle equations according to:

$$\mathbf{f}_e = \mathbf{H}_{fw}w \quad , \quad \text{with:} \quad \mathbf{H}_{fw} = \begin{bmatrix} 1 \\ 0 \end{bmatrix} \quad (5-8)$$

In chapter 6 we will focus on how to generate a generalized roll torque, without exciting the steering torque.

5-5-3 Spectral excitation

According to Ljung (1987) the input bandwidth can be determined by analyzing the estimated parameter covariance. Here, the input signal should be chosen such that it results in a low parameter covariance, which means that the parameters can be estimated more accurately. It is preferable to excite those frequencies where the estimated parameters are the most sensitive.

To analyze the parameter sensitivity, the reduced parameteric model structures obtained in chapter 4 will be used to determine the model sensitivity in the frequency domain. The

model parameter sensitivities are calculated by using the Matlab symbolic toolbox. In order to achieve this a function called (sys2sym) is written, which can convert almost any transfer function object to a symbolic expression as a function of the symbolic Laplace operator. The rider model is also symbolically parameterized and together with the bicycle equations we can derive the symbolic closed loop transferfunction $G_\delta(s, \theta)$, which is stated in equation 2-34. Next we take the partial derivative of $G_\delta(s, \theta)$ with respect to the parameters, which results in the model parameter sensitivity function $G_{\delta,\theta}(s, \theta)$. The resulting parameter sensitivities for different forward velocities are obtained and shown in figure 5-2, 5-3 and 5-4.

From these figures we observe that the models are most sensitive around 0.2 to 4 Hz. Therefore the following input frequency (f_{bw}) bandwidth is chosen to encapsulate the observable controller dynamics:

$$\{0.2 < f_{bw} < 4\} \text{ [Hz]}. \quad (5-9)$$

The input signal will be applied at 10 equally spaced points on the frequency grid, which is stated in section 5-4. The resulting input frequencies f_w thus become:

$$f_w = \begin{bmatrix} 0.020 \\ 0.061 \\ 0.103 \\ 0.145 \\ 0.186 \\ 0.228 \\ 0.270 \\ 0.311 \\ 0.353 \\ 0.395 \end{bmatrix} \text{ Hz} . \quad (5-10)$$

Concludingly, we have determined the input frequencies by analyzing the model parameter sensitivities in the frequency domain.

5-5-4 Input power

The power of the perturbation signal should be scaled such that a good signal to noise ratio for the output is achieved, while keeping the geometric nonlinearities small and (e.g. small angles). These small angles also ensure safety, since large roll deviations may cause the system to fall over. At first we where thinking to design the excitation power such that it would correspond to a certain maximum roll angle deviation. For which a reasonable maximal roll angle approximation would be around 10 degrees or 0.1745 radians of roll angle. However, during the of the perturbator (chapter 6) we realized that the input power is limited by the perturbator design and not the maximum desired roll angle output. Therefore we decrease the input power, so the maximum roll angle deviation of 0.1745 is never reached. After a process of trial and error, the maximum input torque is set to 40N/m which corresponds roughly to a mass of 4kg with a lever arm of 1m. The corresponding auto spectral density of the input will be scaled such that this maximum input amplitude is not exceeded.

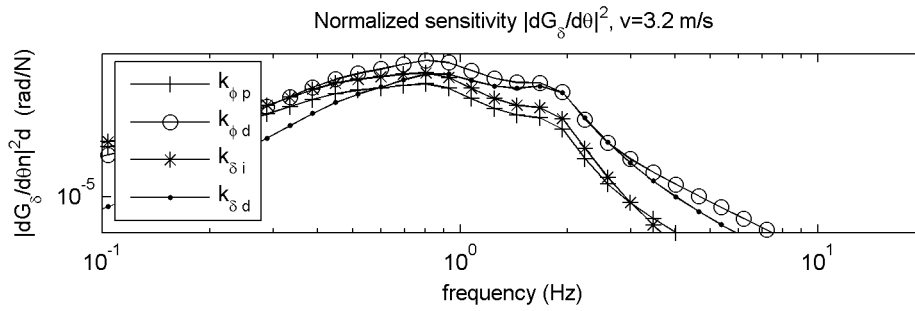


Figure 5-2: Squared sensitivity for the reduced parametric model at a forward velocity of $v = 3.2$ m/s for the steering angle $|\partial G_\delta/\partial \theta|^2$.

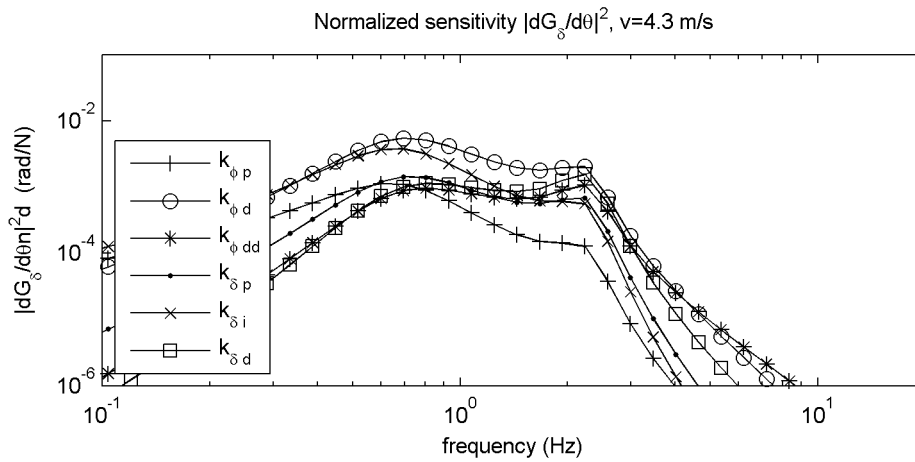


Figure 5-3: Squared sensitivity for the reduced parametric model at a forward velocity of $v = 4.3$ m/s for the steering angle $|\partial G_\delta/\partial \theta|^2$.

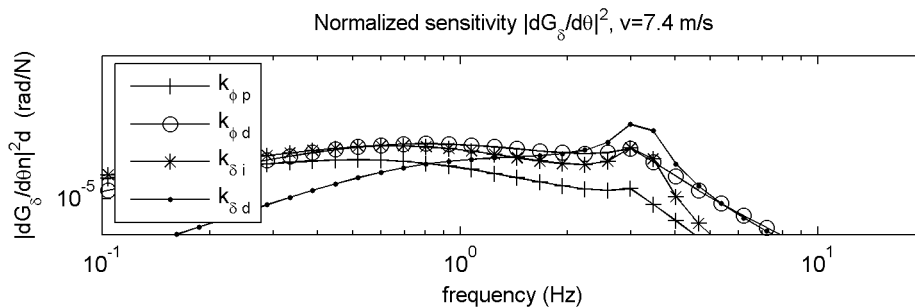


Figure 5-4: Squared sensitivity for the reduced parametric model at a forward velocity of $v = 7.4$ m/s for the steering angle $|\partial G_\delta/\partial \theta|^2$.

5-5-5 Input signal design

Finally, the measurement settings, 10 band multi sine cresting, desired frequency bandwidth and maximum input amplitude are combined into one input spectrum $\Phi_w(\omega)$. This spectrum will be the same for all forward velocities, since its input power is limited by the perturbator design, which independent of the forward velocity. The resulting spectrum is shown in figure 5-5 and will be used for future simulations, covariance estimation and during the design of a perturbator. The time domain representation is shown in figure 5-6, which shows that the input signal is scaled such that the maximum amplitude of 40Nm is not exceeded.

5-6 Measurement Considerations

Without going into to much detail, some aspects about future rider identification experiments are presented and discussed in this section. For example, a clear task instruction is believed to be of key importance, since it affects the control behavior. Non-linearities may also be present in the underlying system, which could be identified by experimenting with different levels of input power.

5-6-1 A priori measurements

Apart from the perturbation experiment, some additional information about the bicycle and subjects in particular should also be gathered. For example, it would be interesting to know the gender, age, bicycle experience for each subject. In addition, we also need to know the inertial properties of the subjects, so their weight and dimensions should also be measured. This should also be done for the bicycle, where we want to know the exact dimensions and inertial properties to derive a proper bicycle model.

5-6-2 Environment

The experimental data presented in chapter 3 was obtained from experiments performed on either a treadmill or at the pavillion floor. From the treadmill data we already observed control action on the heading, which is due to the rather narrow track. The pavillion floor was rather small, which forces the rider to ride in circles. From these experiments, it becomes clear that the enviroment may also affect the rider behavior. This is generally not desired, since we are actually interested in pure roll stabilization. So for these experiments it is recommended to perform the experiments on a rather large, flat and open surface. Perhaps an unfinished highway or old runway might serve for this. In addition, the measurements should be performed during good weather conditions, where the wind excitation is low.

5-6-3 Task instruction

The task instruction determines the goal of control. According to Mugge et al. (2007), the following task descriptions are identified in human control:

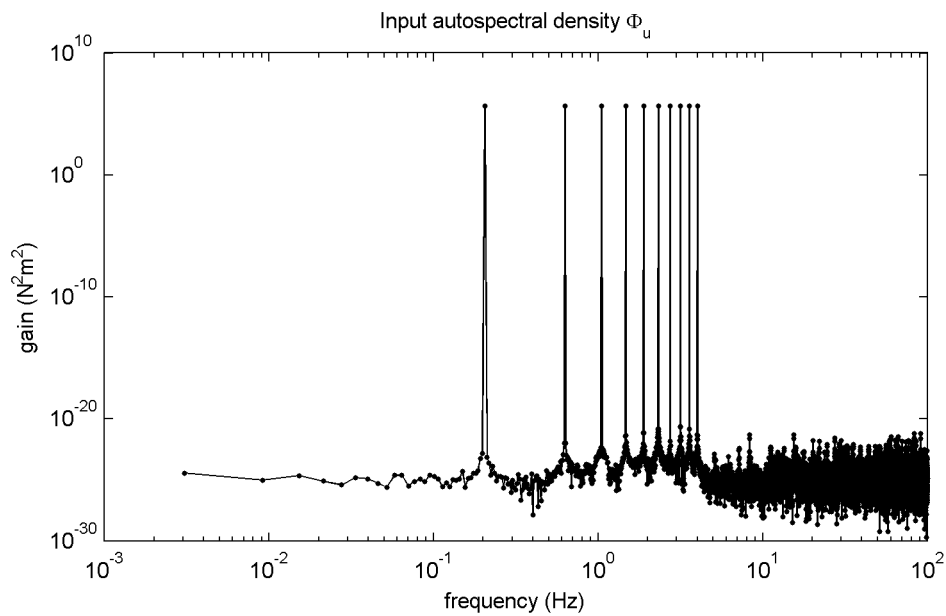


Figure 5-5: Auto spectral density of the input signal Φ_u as a function of frequency. The input power is equally divided between 10 sines between 0.2 and 4 Hz. The phases of the underlying signal $u(\omega)$ are randomized, such that the maximum output amplitude in the time domain of $u(t)$ is minimized.

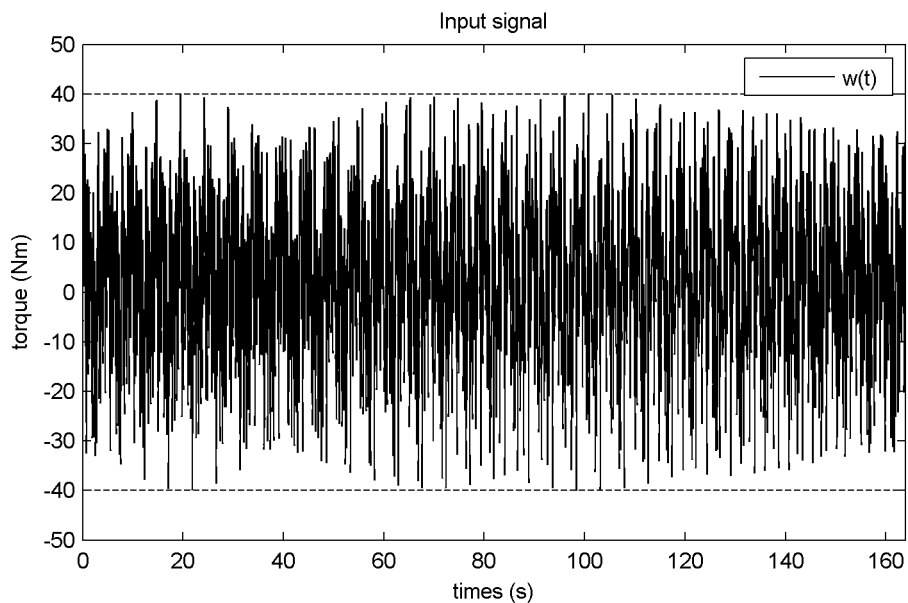


Figure 5-6: Time domain representation of the input signal $w(t)$. The signal is scaled such that the amplitude does not exceed the maximum stress threshold of 40Nm.

- Relax (do nothing)
- Maintain a constant force (or torque)
- Maintain a constant position (or angular rotation)
- Daily life task (e.g. walking)

In our case, we are interested in roll stabilization during force perturbation. This corresponds to a position task, where the subject should be instructed to maintain zero roll angle. In addition, since we are not interested in heading control, the subject should also be explicitly instructed not to control the heading.

5-6-4 Number of trials and subjects

Each subject should perform perturbation runs for forward velocities of $v = 2, 3, \dots, 7$ m/s. In addition some extra runs may be requested to identify non linearities, which is discussed in the next section. The number of subjects is yet to be decided, where more subjects may reveal clearer correlations.

5-6-5 Detection of non linearities

Although all of the described analysis is of linear nature, there still might be non-linearities present within the system. These non-linearities could be caused by geometrical non linearities and/or non linear rider control.

To identify whether scaling non linearities are present, it is recommended to repeat the measurements with different degrees of input power. These non linearities could be due to geometrical non linearities, but also due to non linear rider control. For example, Doyle (1988) describes an intermittent control mechanism on the roll angle, which only kicks in after a certain roll angle is exceeded.

From the previous chapter, we learned that the remnant noise model $v(t)$ describes the part which can not be correlated linearly to the input. This means that the remnant could either be due to stochastic properties of the system or may be caused by non linearities in the underlying system. However, it is hard to point from which source this remnant exactly originates from.

A possible solution would be to perform the measurements several times at different levels of input power. Here, the input could be scaled, such that input torque gradually build up to $\max |w(t)| = 20, 40$ and (if possible) 60 Nm. By doing so, we might be able to detect, which parts of the response scale up linear and which parts do not. Therefore, it is recommended to repeat at least some of the measurements with different levels of input power.

In addition, it would also be interesting to perform some zero input (non perturbation) experiments, which could be used to obtain the noise model. This noise model, could then be compared with the noise model obtained from the perturbation experiments, to check whether the noise is input dependent.

To check for input signal related non linearities, it would be interesting to experiment with various input signals, such as step inputs, impulses and multisines. However, for the moment we will only focus on the multisine case.

Model	$\bar{\sigma}_{k_{\phi p}}$	$\bar{\sigma}_{k_{\phi d}}$	$\bar{\sigma}_{k_{\phi dd}}$	$\bar{\sigma}_{k_{\delta p}}$	$\bar{\sigma}_{k_{\delta i}}$	$\bar{\sigma}_{k_{\delta d}}$
$\mathbf{K}(s, \boldsymbol{\theta}(v = 3.2))$	58.10e-6	6.64e-6			35.59e-6	9.55e-6
$\mathbf{K}(s, \boldsymbol{\theta}(v = 4.3))$	182.32e-6	42.81e-6	157.33e-6	88.23e-6	67.09e-6	79.85e-6
$\mathbf{K}(s, \boldsymbol{\theta}(v = 7.4))$	173.69e-6	15.51e-6			87.07e-6	20.43e-6

Table 5-1: Normalized SEM values $\bar{\sigma}_k$ for the reduced parametric models. The actual (non normalized) SEM σ_k can be calculated according to $\sigma_k = \bar{\sigma}_k$, where k represent the parameter values.

5-7 Expected parameter accuracy

To check whether the experiment design is informative enough, we will calculate the Standard Error of the Mean (SEM), which is defined as the square root of the diagonal indices of the covariance matrix. The SEM is not completely accurate, since it omits the off diagonal terms of the covariance matrix, but generally it does provides a usefull indication of the individual parameter accuracy. By combining the model sensitivity and input power described in section 5-5 and noise model obtained in section 4-2-1, we can substitute for the parameter covariance expression, which is stated in equation (5-5). The resulting SEM values are normalized with respect to the parameter, for which the resulting normalized SEM values are shown in table 5-1.

The resulting normalized SEM values are all around an order of $1e-5$, which corresponds to an accuracy of 0.001%. This is incredibly accurate, which makes these results hard to believe. As said before, the SEM is not completely accurate, since the off diagonal covariance terms are omitted. Since these off diagonal terms add extra uncertainty, the SEM provides an underestimated indication of the parameter covariance. In the next section, a simulation study is set up, where we will check whether these rather low SEM values are realistic.

5-8 Simulation

The designed input signal is tested by simulating the output response. Here, the deterministic contribution is generated by simulating the parametric model, using the designed input signal. The stochastic contribution is modeled according to the non-parametric noise model obtained in section 4-2-1. This results in a simulated dataset, consisting of input $w(t)$ and output $y(t)$, and allows for system identification. These signals are shown in figure 5-7 for a forward velocity of $v = 3.2\text{m/s}$. The deterministic contribution is generated by making use of the reduced parametric model for $v = 3.2\text{ m/s}$. This model will also be subject of identification, which is described later on within this section. From these results we observe that the maximum roll angle is around 0.05 rad, which corresponds to 3 degrees of rotation. The maximum steering angle response is around 0.2 rad, which is roughly 10 degrees. These angles are rather small, which ensures both linearity and safety at the cost of a decreased signal to noise ratio.

Using frequency domain identification techniques we can obtain the spectral estimates of the underlying closed loop models. Unlike the impulse response experiments, the system is only excited for 10 specific frequencies between 0.2 and 4 Hz. Therefore it is only possible

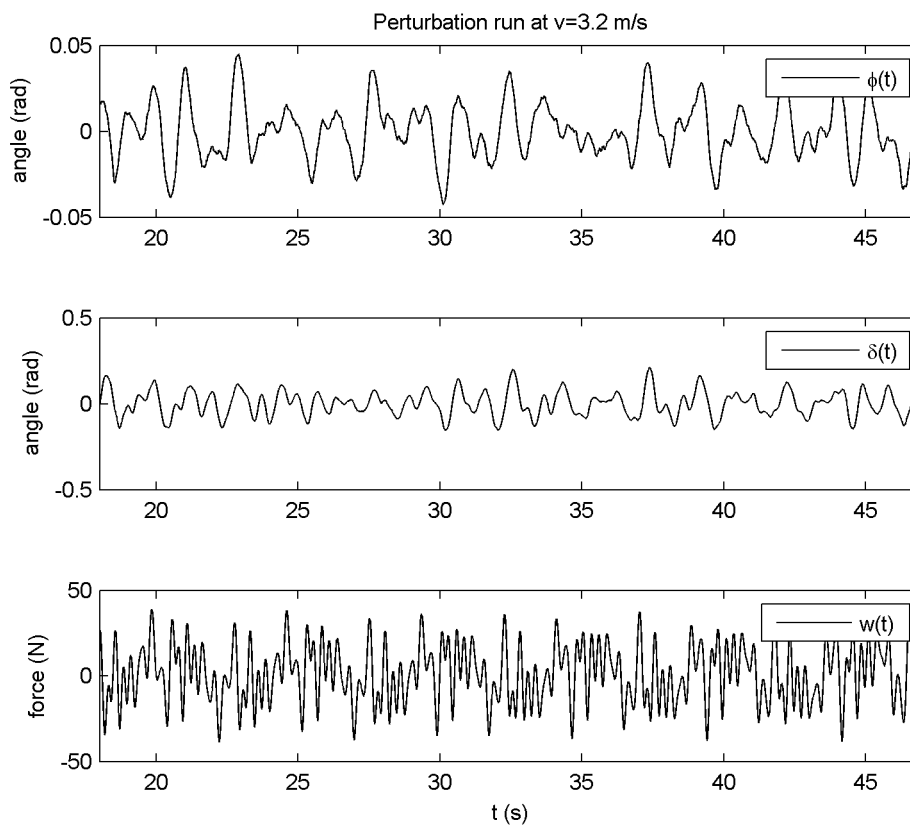


Figure 5-7: Simulation of the roll angle ϕ (top), steering angle δ (middle) using input w (bottom) for a forward velocity of 3.2 m/s.

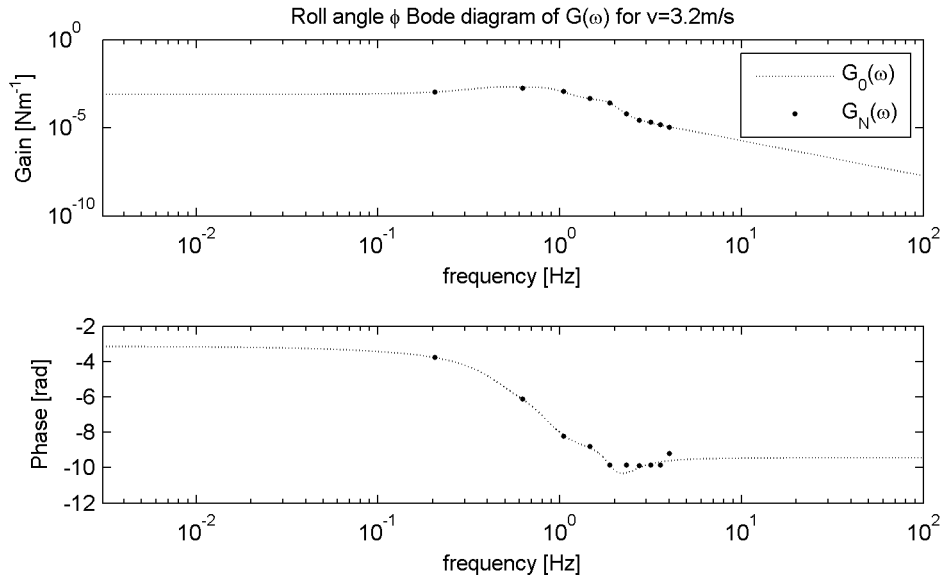


Figure 5-8: Bode plot for the true $G_0(\omega)$ and estimated $G_N(\omega)$ transfer function for the input w to roll angle ϕ response.

to derive the estimated transfer function for a limit number of frequencies and not for the complete bandwidth. The estimated transfer function can be compared to the 'true' system, which was used to generate the simulated output data. This can be useful for validating the method of identification, estimating the accuracy of the obtained data set and analysis of the By comparing the spectral estimates with the 'true' system, which we have obtained in the previous chapter, we can analyze the quality of the spectral estimates. The true and estimated closed loop transfer function for both the roll and steering angle are shown in figure 5-8 and 5-9 respectively. Here, we observe that the estimated transfer function matches the true transfer function almost perfectly. Only around the upper bound of the input frequencies we observe some minor differences, which is probably due to the reduced signal to noise ratio at higher frequencies.

The noise model can be obtained from those frequencies, where no excitation is applied. For these frequencies, the noise spectrum simply equals the output spectrum, so $\Phi_v = \Phi_y$, since $G(\omega)u(\omega)$ is zero at these frequencies. By averaging and interpolation we can also estimate the noise at the excitation frequencies. The obtained noise model can be used for parameter estimation procedure, where the signal to noise ratio is used to assign weighting factors to each frequency.

Next, the estimated transfer function is used for frequency domain parameter estimation. Here we would like determine the parameters of the reduced 4-parameter model for $v = 3.2$ m/s. This is achieved by using frequency domain parameter estimation techniques from chapter 4. The estimated set of parameters is shown in table 5-2, where they are compared with the true set of parameters. From these results we observe that the errors are all rather small, but considerably (± 100 times) larger than the SEM values predicted in the previous section. We already stated that the SEM underestimates the parameter variance, but a factor 100 is rather a lot. Still the simulation results are satisfactory, since the true parameters are

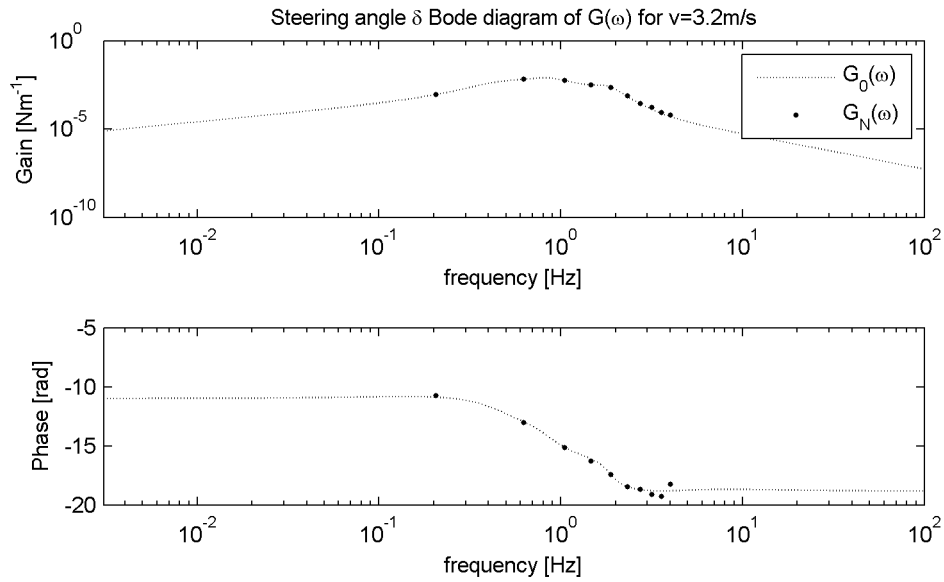


Figure 5-9: Bode plot for the true $G_0(\omega)$ and estimated $G_N(\omega)$ transfer function for the input w to steering angle δ response.

Symbol	θ_0	$\hat{\theta}_N$	$(\theta_0 - \hat{\theta}_N)/\theta_0$
$k_{\phi p}$	36.7135	36.6692	0.0012
$k_{\phi d}$	32.9633	32.5039	0.0139
$k_{\delta i}$	89.2661	86.7232	0.0285
$k_{\delta d}$	-3.2486	-3.2466	0.0006

Table 5-2: Comparison between 'true' parameters θ_0 and estimated parameters $\hat{\theta}_N$ for the reduced model where the forward velocity is set to $v = 3.2\text{m/s}$. The error is normalized with the true parameters and indicates the error. The maximum error for this simulation experiment is around 10%.

estimated with 0.6 to 2.8 % accuracy. However, this simulation study is purely linear, whereas in reality non linear and time varying effects will have a negative impact on the parameter accuracy.

5-9 Summary

The goal of the experiment will be to determine the parameters as accurately as possible. This can be achieved by designing the experiment, such that the estimated covariance is as low as possible. The covariance can be minimized by longer measurements, more input power and excitation at the parameter sensitive frequencies.

A number of closed loop identification methods are presented of which the indirect approach is chosen. Here \mathbf{y} and \mathbf{w} are obtained from experiment and \mathbf{G} should be determined a priori. The method is easy to implement, and allows for commonly used open loop identification methods.

The experiment should be recorded at a measurement frequency of 200 Hz, which corresponds to a time resolution of $\Delta T = 0.05$ s. The measurement length is set to $N = 2^{15}$ samples, which corresponds to a total measurement time of $T = N\Delta T = 163.84$ s. The experiment should be performed at forward velocities of $v = 2, 3, \dots, 7$ m/s, since the dynamic behavior is velocity dependent.

A disturbance input signal has also been designed, and should be applied as a generalized roll torque to the system. In order to prevent feed forward control, the input signal should appear to be random, which can be achieved by superimposing 5 multi sines or more. The input bandwidth ranges from 0.2 to 4 Hz, and the input power is scaled such that $\max |w(t)| = 40$ Nm. The resulting input signal is shown in figure 5-5 and 5-6.

It is important that the subject is properly instructed prior to the experiment, since task type affects the control action. In addition, the environment may also affect the rider control, which is observed in previous experiments. In our case, the subject should be instructed to maintain a zero roll angle, i.e. balancing in an upright position.

As final test, a simulation is performed for the case of 3.2 m/s, where the newly designed input signal is used for simulating the bicycle/rider model derived in chapter 4. The resulting response shows a maximum roll angle of 3 degrees and maximum steering angle of 10 degrees. Next, the simulation data is used for non parametric and parametric model estimation in the frequency domain. The estimated parameters were found to be in good agreement with the 'true' parameters, although the accuracy was poorer than the expected SEM.

Chapter 6

Perturbator Design

In this chapter we will focus on designing mechanisms that are capable of applying a pure roll torque to the combined bicycle/rider system. This is a challenge, since the roll torque is defined relatively to the external world, where is no physical connection, except for the rear and front wheel contact points. The goal is to design a perturbator which is able to generate a generalized roll torque T_ϕ , without exciting the steer torque T_δ , which is equal to the desired perturbation signal $w(t)$ described in chapter 5. In this chapter we will present and analyze a number of perturbator designs, for which one design will be chosen for further development.

All perturbator designs will be formulated in the perturbation plane, which is shown and defined in figure 6-1. By doing so, only a generalized roll torque is exerted, since any force applied within this plane is orthogonal to the generalized steering torque.

The general approach is to only model the perturbator dynamics, which will interact with the bicycle through the roll reaction torque $-T_\phi$. The steering angle is omitted here, since we assume that the perturbation takes place in the perturbation plane, which is orthogonal to the steering angle. The perturbator may introduce some degree of freedom x , which interacts with the rider/bicycle equations. In this case, we generally end up with a system of following kind:

$$\begin{bmatrix} m_{11} & m_{12} \\ m_{21} & m_{22} \end{bmatrix} \begin{bmatrix} \ddot{\phi} \\ \ddot{x} \end{bmatrix} + \begin{bmatrix} c_{11} & c_{12} \\ c_{21} & c_{22} \end{bmatrix} \begin{bmatrix} \dot{\phi} \\ \dot{x} \end{bmatrix} + \begin{bmatrix} k_{11} & k_{12} \\ k_{21} & k_{22} \end{bmatrix} \begin{bmatrix} \phi \\ x \end{bmatrix} = \begin{bmatrix} -T_\phi \\ f_x \end{bmatrix} \quad (6-1)$$

with roll angle ϕ , some perturbator related degree of freedom x , mass, damping and stiffness coefficients m_{ij} , c_{ij} , k_{ij} , roll torque T_ϕ and external input f_x corresponding to x . Here the roll torque is defined negatively with respect to ϕ since it describes a reaction torque.

From equation 6-1 we observe that the roll torque depends on both ϕ and x . The part that is related to the roll angle ϕ we call the passive system contribution, since this is the part that affects the bicycle dynamics when the perturbator is inactive $x(t) = 0$. The passive system contribution is given by the coefficients: m_{11} , c_{11} and k_{11} , which add up to the roll angle equation in chapter 2. The remaining part related to x , we call the active system

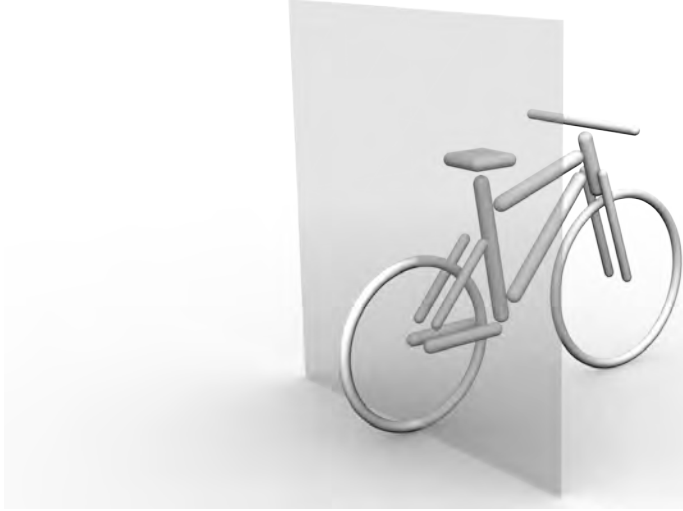


Figure 6-1: Perturbation plane; any force applied within this plane can only exert a generalized roll perturbation. The plane spans the lateral y and longitudinal z direction and intersects with the forward x direction at the rear wheel contact point. This is the plane in which the perturbator will be designed.

contribution, and is given by the coefficients: m_{12} , c_{12} and k_{12} . The active part will mainly be used to induce the desired perturbation signal $w(t)$.

As said, the goal of the perturbator is to apply a generalized roll torque T_ϕ , which should be equal to the required disturbance torque $w(t)$. However, we could also accept that the perturbator changes the bicycle dynamics in a passive way, by only setting the active system contribution equal to $w(t)$. This is preferable since $w(t)$ only depends on x , which means we can determine the desired perturbation configuration $x(t)$ a priori. In this case, the required frequency spectrum of x is obtained through:

$$x(\omega) = \frac{1}{-\omega^2 m_{12} + i\omega c_{12} + k_{12}} w(\omega) , \quad (6-2)$$

where $w(\omega)$ is input spectrum and for which $x(t)$ can be obtained by taking the inverse Fourier transform of $x(\omega)$.

Next we will analyze the second row of equation 6-1, which describes the perturbator dynamics. Here, the m_{21} , m_{22} , c_{21} , c_{22} , k_{21} and k_{22} coefficients describe the perturbator dynamics and how the perturbator should be activated through f_x . These coefficients can be used to determine the required perturbation torque and power. By setting $\phi = 0$, we obtain the the active system contribution f_x is determined by $x(t)$ and m_{22} , c_{22} and k_{22} , according to:

$$f_x(\omega) = -\omega^2 m_{22} + i\omega c_{22} + k_{22} x(\omega) , \quad (6-3)$$

And the required perturbation power P_x is defined as the force times velocity, resulting in:

$$P_x(t) = f_x(t) \dot{x}(t) , \quad (6-4)$$

where we make use of $\dot{x}(\omega) = i\omega x(\omega)$, which can be transformed to the time domain, by taking the inverse Fourier transformation of the corresponding signals. These time domain results

may be used to determine the requirements on the perturbator force, such as maximum force, power output, displacement amplitude, velocity requirements, etc.

In the succeeding sections, we will analyze a number of perturbator designs.

6-1 Design of a swing perturbator

The swing perturbator uses a mass unbalance which hinges above the rear wheel contact point. By doing so, it can be shown that the swing perturbator, only results in a generalized desired roll perturbation. The system is drawn in figure 6-2, for which the equations of motion will be derived using the TMT method.

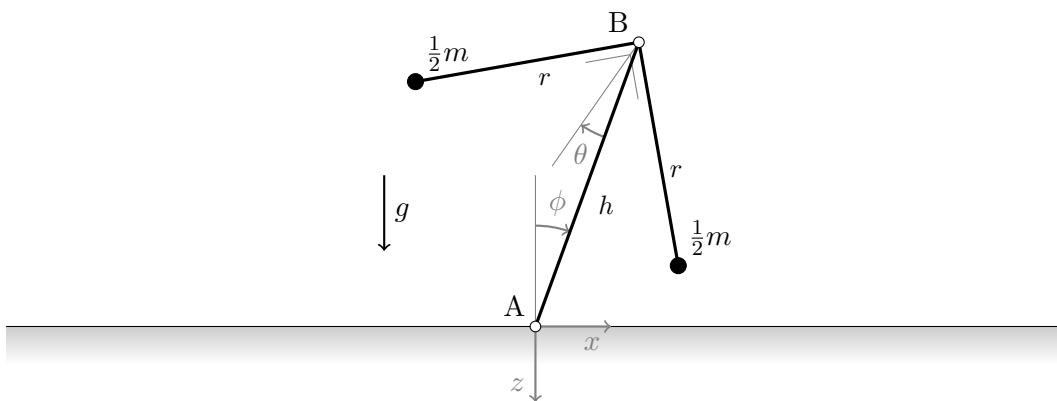


Figure 6-2: Simplified swing perturbator, with; A real wheel contact, B swinging hinge point, h distance between A and B , r distance between B and masses m_1 and m_2 and where g represents the acceleration caused by gravity. The two mass points are placed under a 90 degree angle, such that they allow for a swinging angle of almost 45 degrees back and forth. The connectors are all simplified to massless rods.

6-1-1 Equations of Motion

The generalized coordinates consist of the swing angle θ and roll angle ϕ , according to:

$$q_s = [\phi, \theta]^T \quad (6-5)$$

The xz coordinates and rotation of the combined center of mass (which lies exactly between the two masses) and its rotation expressed in terms of the generalized coordinates are given by:

$$x_i = \begin{bmatrix} h \sin(\phi) - \frac{1}{2}\sqrt{2}r \sin(\phi + \theta) \\ -h \cos(\phi) + \frac{1}{2}\sqrt{2}r \cos(\phi + \theta) \\ \phi + \theta \end{bmatrix}. \quad (6-6)$$

The corresponding inertia matrix and conservative force vector then become:

$$M_{ij} = \begin{bmatrix} m & 0 & 0 \\ 0 & m & 0 \\ 0 & 0 & \frac{1}{2}mr^2 \end{bmatrix}, \quad f_i = \begin{bmatrix} 0 \\ mg \\ 0 \end{bmatrix}. \quad (6-7)$$

which result in the following equations of motion:

$$M_{ij}\ddot{x}_j - f_i = 0 \quad (6-8)$$

By partial differentiation of x_i with respect to q_s we obtain the coordinate projection matrix $T_{i,s} = \partial T_i / \partial q_s$ which is used to derive the generalized equations of motion, according to:

$$M_{sr}\ddot{q}_r - f_s = 0, \quad (6-9)$$

where;

$$M_{sr} = T_{i,s}M_{ij}T_{j,r}, \quad f_s = T_{i,s}(f_i - M_{ij}g_j), \quad g_j = T_{j,p}q_p\dot{q}_q. \quad (6-10)$$

Next the equations are linearized around the upright position, so $\ddot{q}_s = \dot{q}_s = q_s = 0$, resulting in the following mass, damping and stiffness matrices:

$$\begin{aligned} \tilde{M}_{sr} &= \left. \frac{\partial(M_{sr}\ddot{q} - f_s)}{\partial \ddot{q}_r} \right|_{\ddot{q}_s=\dot{q}_s=q_s=0}, \\ \tilde{C}_{sr} &= \left. \frac{\partial(M_{sr}\ddot{q} - f_s)}{\partial \dot{q}_r} \right|_{\ddot{q}_s=\dot{q}_s=q_s=0}, \\ \tilde{K}_{sr} &= \left. \frac{\partial(M_{sr}\ddot{q} - f_s)}{\partial q_r} \right|_{\ddot{q}_s=\dot{q}_s=q_s=0}, \end{aligned}$$

with coefficients;

$$\tilde{M}_{sr} = \begin{bmatrix} m(h^2 - \sqrt{2}hr + r^2) & \frac{1}{2}mr(2r - \sqrt{2}h) \\ \frac{1}{2}mr(2r - \sqrt{2}h) & mr^2 \end{bmatrix}, \quad (6-11)$$

$$\tilde{C}_{sr} = \begin{bmatrix} 0 & 0 \\ 0 & 0 \end{bmatrix}, \quad (6-12)$$

$$\tilde{K}_{sr} = \begin{bmatrix} -\frac{1}{2}m(2gh - \sqrt{2}rg) & \frac{1}{2}\sqrt{2}rmg \\ \frac{1}{2}\sqrt{2}rmg & \frac{1}{2}\sqrt{2}rmg \end{bmatrix}. \quad (6-13)$$

which describe the equations of motion in terms of the generalized coordinates according to;

$$\tilde{M}_{sr}\ddot{\tilde{q}}_r + \tilde{C}_{sr}\dot{\tilde{q}}_r + \tilde{K}_{sr}\tilde{q}_r = f_{s,ext}, \quad (6-14)$$

where the external forces $f_{s,ext} = [-T_\phi, T_\theta]^T$ are simply added to the equations. For convenience, we will drop the tilde notation from now on and assume linearity throughout the rest of the analysis.

6-1-2 Analysis

The analysis is split up in a active and passive perturbator contribution.

Active system contribution

We start of by fixing the roll angle ϕ , so we can analyze the influence of the newly added coordinate θ on the roll excitation T_ϕ . By substituting $\phi = 0$ and take the roll angle equation, we can derive the following expression for the roll torque:

$$m_{12}\ddot{\theta} + c_{12}\dot{\theta} + k_{12}\theta = -T_\phi , \quad (6-15)$$

For which we can write out the mass, damping and stiffness coefficients, resulting in:

$$T_\phi = \underbrace{-\frac{1}{2}mr(2r - \sqrt{2}h)}_{\text{dynamic cont.}} \ddot{\theta} - \underbrace{\frac{1}{2}\sqrt{2}rmg}_{\text{static cont.}} \theta . \quad (6-16)$$

So the roll torque consists of a dynamic (inertial) and static (spring) contribution, which are both proportional to the mass. The static contribution is also proportional to r , which means that the static efficiency can be improved by simply increasing the mass hinge distance r .

Next, we will derive the frequency response function from θ to T_ϕ . By introducing the Laplace operator $s = i\omega$ and assuming the initial conditions to be zero, we derive:

$$\frac{T_\phi}{\theta} = \frac{1}{2}mr(2r - \sqrt{2}h)\omega^2 - \frac{1}{2}\sqrt{2}rmg , \quad (6-17)$$

This result shows two types of behavior. Dependent on whether r is greater or lower than $\frac{1}{2}\sqrt{2}h$, the dynamic and static may either add up or cancel out.

First, we focus on the case where $2r \leq \sqrt{2}h$, where the inertial and static force add up. From equation 6-17 we observe that the inertial contribution depends quadratically on r . This inertial contribution can be optimized by setting its partial derivative with respect to r to zero and solve for r , resulting in:

$$\frac{\partial}{\partial r} \left[\frac{1}{2}mr(2r - \sqrt{2}h) \right] = \frac{1}{2}m(2r - \sqrt{2}h) + mr = 0 \rightarrow r = \frac{1}{4}\sqrt{2}h , \quad (6-18)$$

which means that the height of the combined center of mass is equal to half the swinging hinge height h .

The stiffness component is proportional to r , which means a larger r is more beneficial. However, r is also bounded by the zero gain frequency constraint $r \leq \frac{1}{2}\sqrt{2}h$, which forms an upper bound of r . Therefore, the optimal stiffness is achieved when $r = \frac{1}{2}\sqrt{2}h$.

Combining the optimal inertial and static parameter configurations results in the optimal parameter space of r :

$$\frac{1}{4}\sqrt{2}h \leq r \leq \frac{1}{2}\sqrt{2}h . \quad (6-19)$$

where the lower represents the inertial optimum which is useful for high frequency excitation and the upper bound describes the static optimum which is useful for quasi static excitation. So given a certain excitation frequency; an optimal r can be found within these boundaries.

Next, we focus on the case where $2r > \sqrt{2}h$, where the inertial and static force may cancel out. The cancellation is frequency dependent, for which the zero gain frequency ω_0 is the frequency where $T_\phi/\theta = 0$.

$$\omega_0 = \sqrt{\frac{\sqrt{2}g}{2r - \sqrt{2}h}} , \text{ for } 2r > \sqrt{2}h . \quad (6-20)$$

At and round the zero gain frequency, the gain is very low, resulting in a small torque output for large swing angle input. Therefore, this zero gain frequency should not interfere with the input bandwidth, so $\omega_0/2\pi$ should either be way smaller than 0.2 Hz or larger than 4 Hz. Figure 6-3 shows the zero gain frequency as a function of the parameters r and h . Here, the feasible domain is bounded by the two following constraints:

1. Zero gain constraint: $2r > \sqrt{2}h$.
2. Geometrical constraint: $r < h$.

The first constraint follows from 6-20 and the second constraint is a geometrical constraint. Without the latter it would be possible for r to be longer than h , which means the swing will intersect with the ground level for $\theta = 45$ degrees. From figure 6-3 and equation 6-20

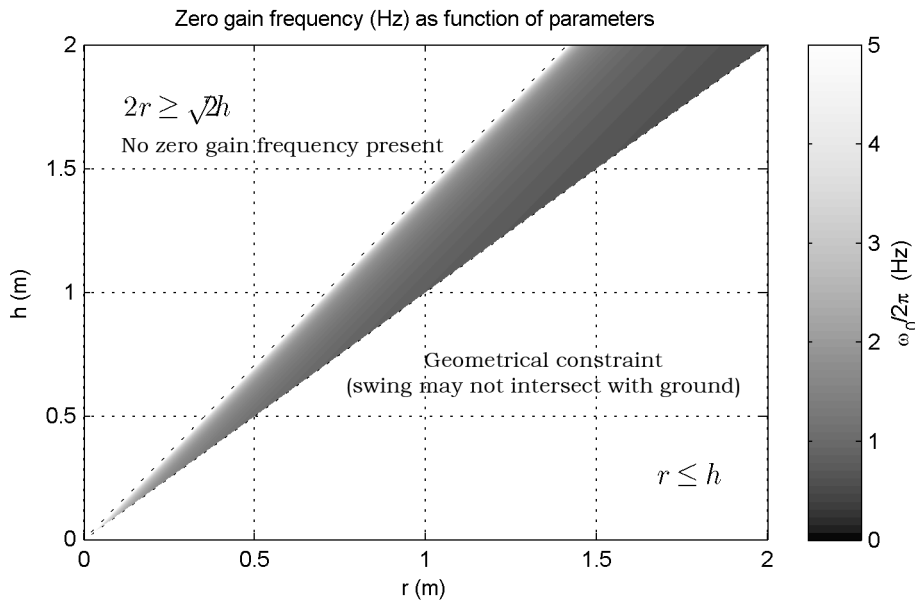


Figure 6-3: Zero gain frequency ω_0 as function of the swing arm length r and swing axis height h . The white top left triangle is infeasible by the stability constraint, the bottom right white triangle is due to the geometrical constraint. Even while both distances are plotted on a scale from 0 to 2 m, there is no feasible solution where the zero gain frequency is outside the input bandwidth of 0.2 to 4 Hz.

we observe that the eigenfrequency goes to infinity for $2r \rightarrow \sqrt{2}h$. However this region lies on the edge of instability, which makes it a challenge to design properly. On the other hand, the lowest eigenfrequency is reached at $r = h = 2\text{m}$, which results in a zero gain frequency of 0.54 Hz. In short, there is no feasible result for the case of $2r > \sqrt{2}h$.

Concludingly, the design is most efficient where $2r < \sqrt{2}h$, since no zero gain frequency is present and the static and dynamic contributions add up.

Passive system contribution

Next, we focus on the passive system contribution of the perturbator to the roll dynamics. This is achieved by fixing θ , and analyze the roll equation, which reduces to:

$$m_{11}\ddot{\phi} + c_{11}\dot{\phi} + k_{11}\theta = -T_{\phi} , \quad (6-21)$$

Where the mass, damping and stiffness terms result in a passive additive contribution to the bicycle roll equation. For which we can write out the mass, damping and stiffness coefficients, resulting in:

$$T_{\phi} = -m(h^2 - \sqrt{2}hr + r^2)\ddot{\theta} + mg(h - \frac{1}{2}\sqrt{2}r) . \quad (6-22)$$

The static contribution is similar to that of a simple pendulum, where $h - \frac{1}{2}\sqrt{2}r$ is the height of the center of mass. The inertial contribution depends also the same height squared, so: $m(h - \frac{1}{2}\sqrt{2}r)^2 = m(h^2 - \sqrt{2}rh + \frac{1}{2}r^2)$. The remaining inertia $m\frac{1}{2}r^2$ is due to the rotational inertia around the center of mass.

The both the inertial and passive system contribution are minimized for the case where $\frac{1}{2}\sqrt{2}r = h$, which means that the center of mass lies in the contact point. For this case the stiffness term completely diminishes, while the inertia reduces to $\frac{1}{2}r^2$. However this is not realistic, since the geometrical constraint ($r \leq h$) is violated.

Example

Let's assume a the perturbator is mounted on top of the luggage carrier, which corresponds roughly to a height $h = 0.7$ m. After some trial and error we set $r = \frac{1}{3}\sqrt{2}h$, which results in a good roll-torque/swing-angle ratio. The gravitational acceleration is fixed to $g = 9.81$ m/s² and the mass is set to $m = 20$ kg.

We then can calculate the required swing angle $\theta(t)$ as a function of the desired perturbation signal $w(t)$. The resulting time response is shown in figure 6-4, which shows a maximal swing angle of around 0.35 rad or 20 degrees.

The corresponding torque and power can be calculated by using equations 6-3 and 6-4 respectively. These results are shown in figure 6-5, where the maximum absolute torque and power are 65.27 Nm and 67.22 Watt.

By substituting the parameters into 6-21, we can also calculate the passive system contribution, which yields: $m_{11} = 5.44$ kg·m² and $k_{11} = -91.45$ Nm/rad. So this particular swing perturbator adds additional inertia and negative stiffness to the system.

6-1-3 Summary

A swing type perturbator has been modeled and analyzed. The transfer function from swing angle θ to roll torque output T_{ϕ} has been derived. To be effective, this mechanism should have a large gain, meaning low swing angle inputs should result in large torque outputs. However, the transfer function has an eigenfrequency, which should fall outside the input bandwidth of 0.2 to 4 Hz. This eigenfrequency depends on swing arm r and swing hinge height h design parameters. Figure 6-3 shows that there is a very limited set of parameter combinations possible to achieve this goal. In addition, the swing perturbator also passively adds addition inertia and negative stiffness to the system.

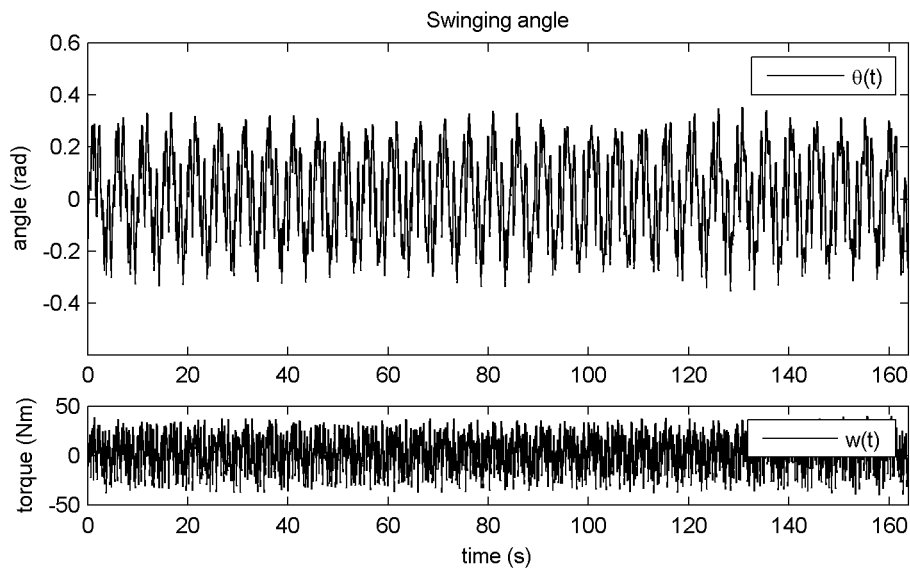


Figure 6-4: Required swing angle θ as a function of the desired roll perturbation w , with parameters: $h = 0.7$ m, $r = \frac{1}{3}\sqrt{2}h$ m, $g = 9.81$ m/s² and $m = 20$ kg.

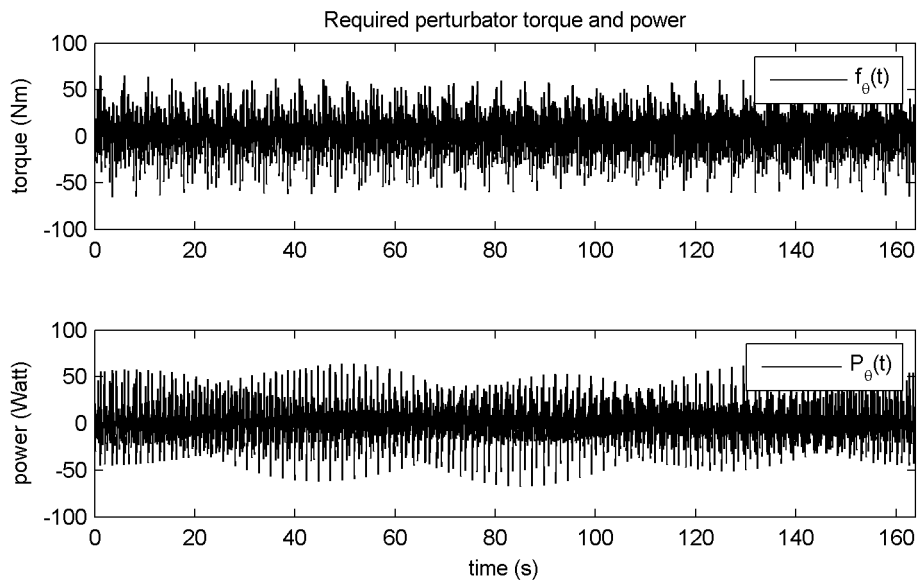


Figure 6-5: Perturbator torque f_θ and power P_θ as a function of time t , with parameters: $h = 0.7$ m, $r = \frac{1}{3}\sqrt{2}h$ m, $g = 9.81$ m/s² and $m = 20$ kg.

6-2 Design of a sliding mass perturbator

The sliding mass perturbator uses a mass which slides laterally above the rear wheel contact point. By doing so, it can be shown that the sliding mass perturbator, only results in a generalized roll perturbations. The system is drawn in figure 6-6, for which the equations of motion are derived using the TMT method. The analysis shows a lot of similarity with the swinging perturbator,

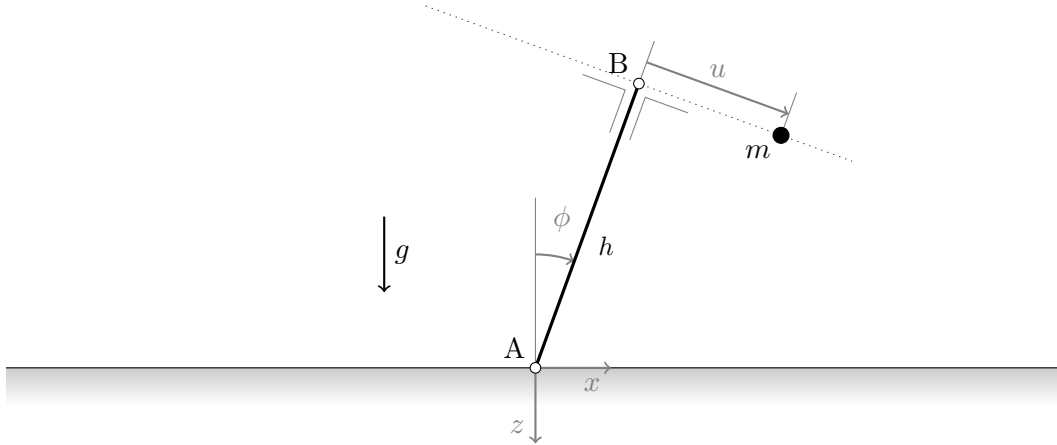


Figure 6-6: Simplified sliding mass perturbator, with; A real wheel contact, B zero sliding point, h distance between A and B , u slider displacement and where g represents the acceleration caused by gravity. The connectors are all simplified to massless rods.

6-2-1 Equations of Motion

The generalized coordinates consist of the roll angle ϕ and slider displacement u , according to:

$$q_s = [\phi, u]^T \quad (6-23)$$

The coordinates of the center of mass and is expressed in terms of the generalized coordinates and is given by:

$$x_i = \mathbf{R}_\phi \begin{bmatrix} u \\ -h \end{bmatrix}, \quad \mathbf{R}_\phi = \begin{bmatrix} \cos \phi & -\sin \phi \\ \sin \phi & \cos \phi \end{bmatrix}. \quad (6-24)$$

Notice that the mass is modelled as a point mass, so the rotational inertia around the mass center is zero. For this case, the corresponding inertia matrix and conservative force vector become:

$$M_{ij} = \begin{bmatrix} m & 0 \\ 0 & m \end{bmatrix}, \quad f_i = \begin{bmatrix} 0 \\ mg \end{bmatrix}. \quad (6-25)$$

which result in the following equations of motion:

$$M_{ij}\ddot{x}_j - f_i = 0 \quad (6-26)$$

Similar to the swinging perturbator, the information is inserted into the TMT machinery, resulting into a set of generalized non linear equations. These equations are linearized around the upright equilibrium position, so $\ddot{q}_s = \dot{q}_s = q_s = 0$, resulting in the following mass, damping and stiffness matrices:

$$\tilde{M}_{sr} = \begin{bmatrix} mh^2 & mh \\ mh & m \end{bmatrix} , \quad (6-27)$$

$$\tilde{C}_{sr} = \begin{bmatrix} 0 & 0 \\ 0 & 0 \end{bmatrix} , \quad (6-28)$$

$$\tilde{K}_{sr} = \begin{bmatrix} -mgh & -mg \\ -mg & 0 \end{bmatrix} . \quad (6-29)$$

Similar to the swinging perturbator, this results in the following set of linear equations:

$$\tilde{M}_{sr}\ddot{q}_r + \tilde{C}_{sr}\dot{q}_r + \tilde{K}_{sr}q_r = f_{s,ext} , \quad (6-30)$$

where the generalized external forces $f_{s,ext} = [T_\phi, T_u]^T$ are simply added to the equations. For convenience, we will drop the tilde notation from now on and assume linearity throughout the rest of the analysis.

6-2-2 Analysis

The analysis is divided in an active system contribution (where ϕ is fixed) and a passive system contribution (where u is fixed).

Active system contribution

We start of by fixing the roll angle ϕ , so we can analyze influence of the newly added coordinate u on the roll excitation T_ϕ . By substituting $\phi = 0$ and take the roll angle equation, we can derive the following expression for the roll torque:

$$m_{12}\ddot{u} + c_{12}\dot{u} + k_{12}u = T_\phi , \quad (6-31)$$

For which we can write out the mass, damping and stiffness coefficients, resulting in:

$$T_\phi = mh\ddot{u} - mgu . \quad (6-32)$$

So again the roll torque consists of a dynamic (inertial) and static (spring) contribution, which are both proportional to the mass. This is similar to the swinging perturbator, but here the rotational inertia is zero, due to the point mass model. Both contributions are proportional to m , which means a greater and more beneficial torque to sliding distance ratio.

Next, we will derive the transfer function of u over T_ϕ , which we can use to analyze the frequency response. By introducing the Laplace operator $s = i\omega$ and assuming the initial conditions to be zero, we derive:

$$\frac{T_\phi}{u} = -m(h\omega^2 + g) , \quad (6-33)$$

Contrary to the swing perturbator, the sliding mass perturbator does not have a zero gain frequency. Here, the dynamic and static component now always add up instead of canceling out, under the assumption that h is positive. This is a nice property, since it makes the design way more effective.

Passive system contribution

Next, we focus on the passive system contribution of the perturbator to the roll dynamics. This is achieved by fixing u , and analyze the roll equation, which reduces to:

$$m_{11}\ddot{\phi} + c_{11}\dot{\phi} + k_{11}\theta = T_{\phi} , \quad (6-34)$$

For which we can write out the mass, damping and stiffness coefficients, resulting in:

$$T_{\phi} = mh^2\ddot{\theta} - mgh\theta . \quad (6-35)$$

This is similar to the swing perturbator, where the passive system contribution also consists of additional inertia and negative stiffness. The stiffness is comparable to a simple inverted pendulum, where the stiffness is negatively proportional to the mass, gravity and moment arm around the origin. The inertia is simply proportional to the perturbator mass times the mass center height squared, which is a familiar expression.

In short; the sliding mass perturbator adds inertia and negative stiffness to the system.

Example

Let's assume a the perturbator is mounted on top of the luggage carrier, which corresponds roughly to a height $h = 0.7$ m. The gravitational acceleration is set to $g = 9.81$ m/s² and a mass of $m = 10$ kg is chosen.

We then can calculate the required lateral displacement $u(t)$ as a function of the desired roll torque $T_{\phi} = w(t)$. The resulting time response is shown in figure 6-7, which shows a maximal amplitude of around ± 0.12 m.

The corresponding force and power can be calculated by using equations 6-3 and 6-4 respectively. These results are shown in figure 6-8, where the maximum absolute force and power are 52.73 N and 12.25 Watt.

By substituting the parameters into 6-35, we can also calculate the passive system contribution, which yields: $m_{11} = 4.9$ kg·m² and $k_{11} = -68.67$ Nm/rad.

6-2-3 Summary

A sliding mass type perturbator has been modeled and analyzed. The transfer function from sliding distance u to roll torque output T_{ϕ} has been derived. To be effective, this mechanism should have a large gain, meaning that small sliding displacements should result in large torque outputs. Contrary to the swing perturbator, the dynamic and static contributions add up, which makes it a more effective mechanism. For example, setting the slider height to 0.7m and the mass to 10kg results in maximum displacement of $u = 0.12$ m, which is reasonable. In addition, the sliding mass perturbator also passively adds inertia and negative stiffness to the system.

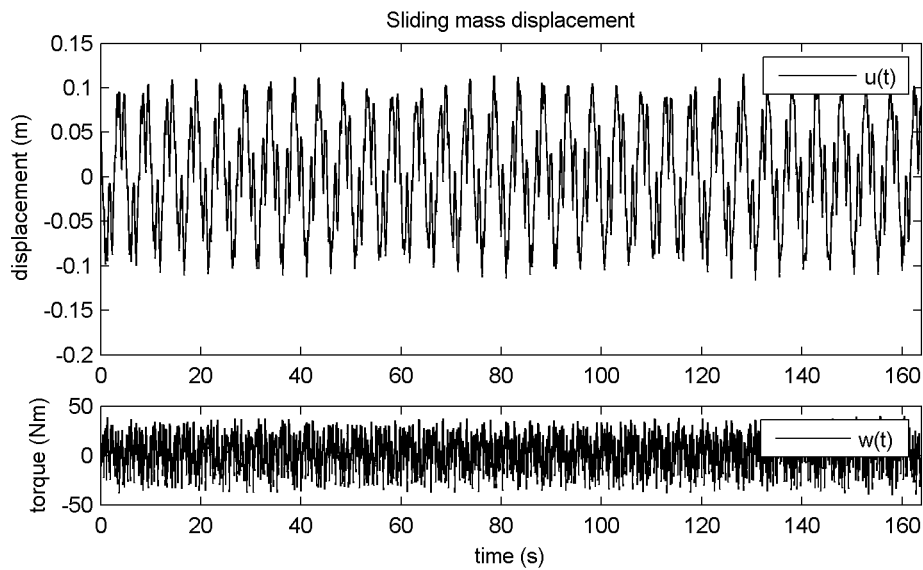


Figure 6-7: Required sliding displacement u as a function of the desired roll perturbation w , with parameters: $h = 0.7$ m, $g = 9.81$ m/s² and $m = 10$ kg.

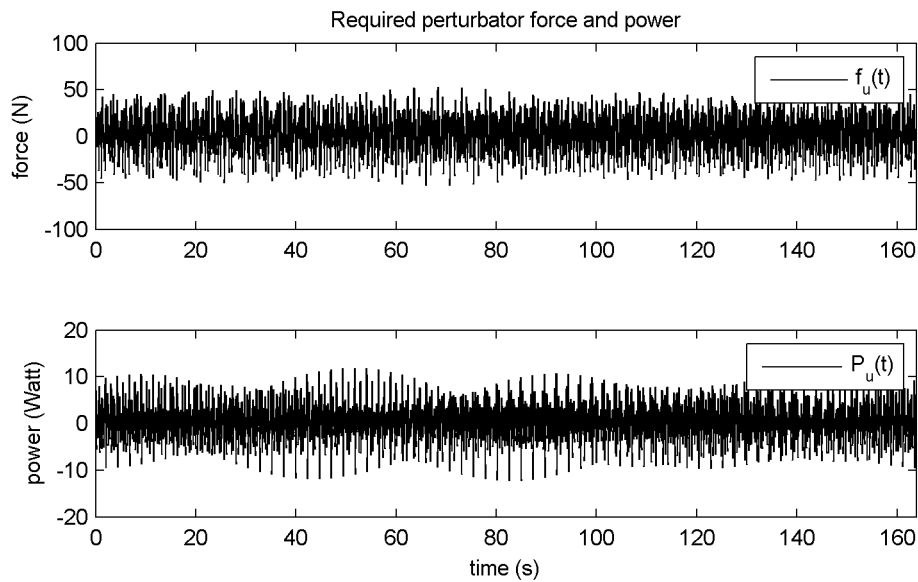


Figure 6-8: Perturbator torque f_u and power P_u as a function of time t , with parameters: $h = 0.7$ m, $g = 9.81$ m/s² and $m = 10$ kg.

6-3 Lateral accelerator

Another possibility would be to accelerate the environment laterally, which results in a lateral acceleration of the rear and front wheel contact points. This concept could be implemented by mounting a treadmill onto a lateral movable platform. By actuating the platform, the contact points are displaced laterally, which creates a falling moment, for which the rider should take appropriate action. By doing so, the mass of the combined bicycle/rider system is basically used for creating a roll perturbation. This won't result in a generalized roll torque, since the front wheel contact point is also excited. However, it is likely that the roll torque dominates the excitation, mass center lies near to the rear wheel contact. In addition, the lateral vestibular feedback of the rider will be biased through the added lateral acceleration.

The concept is shown in figure 6-9, where the analysis is simplified to the perturbation plane. Here, the rear wheel contact is introduced as a degree of freedom.

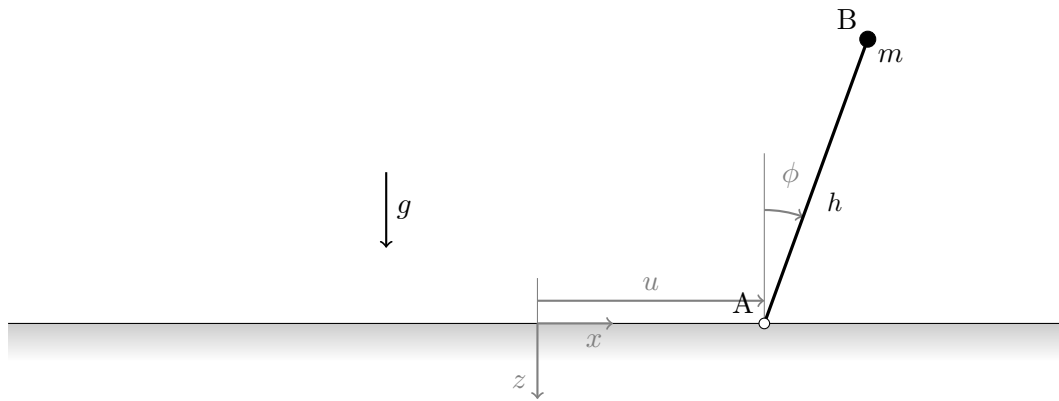


Figure 6-9: Simplified lateral contact point displacement perturbator, with roll angle ϕ , lateral displacement u , rear wheel contact point A , mass m , height of center of mass h and gravitational acceleration g .

6-3-1 Equations of Motion

The generalized coordinates consist of the roll angle ϕ and contact point displacement u , according to:

$$q_s = [\phi, u]^T \quad (6-36)$$

The xz coordinates of the center of mass are expressed in terms of the generalized coordinates and is given by:

$$x_i = \begin{bmatrix} u + h \sin \phi \\ -h \cos \phi \end{bmatrix}. \quad (6-37)$$

Here the mass is modeled as a point mass, so the rotational inertia around the mass center is zero. This is not realistic since the rider in fact has a large moment of inertia. However, since

we will constraint the roll angle later on in the subsequent analysis, this will not matter. The corresponding inertia matrix and conservative force vector become:

$$M_{ij} = \begin{bmatrix} m & 0 \\ 0 & m \end{bmatrix}, \quad f_i = \begin{bmatrix} 0 \\ mg \end{bmatrix}. \quad (6-38)$$

which result in the following equations of motion:

$$M_{ij}\ddot{x}_j - f_i = 0 \quad (6-39)$$

Similar to the swinging perturbator, the information is inserted into the TMT machinery, resulting into generalized non linear equations. These equations are linearized around the upright equilibrium position, so $\tilde{q}_s = \dot{\tilde{q}}_s = \tilde{q}_s = 0$, resulting in the following mass, damping and stiffness matrices:

$$\tilde{M}_{sr} = \begin{bmatrix} mh^2 & mh \\ mh & m \end{bmatrix}, \quad (6-40)$$

$$\tilde{C}_{sr} = \begin{bmatrix} 0 & 0 \\ 0 & 0 \end{bmatrix}, \quad (6-41)$$

$$\tilde{K}_{sr} = \begin{bmatrix} -mgh & 0 \\ 0 & 0 \end{bmatrix}. \quad (6-42)$$

Similar to the swinging and sliding mass perturbator, this results in the following set of linear equations:

$$\tilde{M}_{sr}\ddot{\tilde{q}}_r + \tilde{C}_{sr}\dot{\tilde{q}}_r + \tilde{K}_{sr}\tilde{q}_r = f_{s,ext}, \quad (6-43)$$

where the generalized external forces $f_{s,ext} = [-T_\phi, T_u]^T$ are simply added to the equations. For convenience, we will drop the tilde notation from now on and assume linearity throughout the rest of the analysis.

6-3-2 Analysis

The lateral accelerator uses inertia of the rider/bicycle system to perturb the system, where no passive system contribution is added to the system. Therefore, the analysis is limited to the active system contribution only. In addition the lateral accelerator has no real design parameters, since the height h and mass m are fixed and existing properties of the rider/bicycle system.

Again, we start of by fixing the roll angle ϕ , so we can analyze influence of the newly added coordinate u on the roll excitation T_ϕ . By substituting $\phi = 0$ and take the roll angle equation, we can derive the following expression for the roll torque:

$$m_{12}\ddot{\theta} + c_{12}\dot{\theta} + k_{12}\theta = -T_\phi, \quad (6-44)$$

For which we can write out the mass, damping and stiffness coefficients, resulting in:

$$T_\phi = -mh\ddot{u}. \quad (6-45)$$

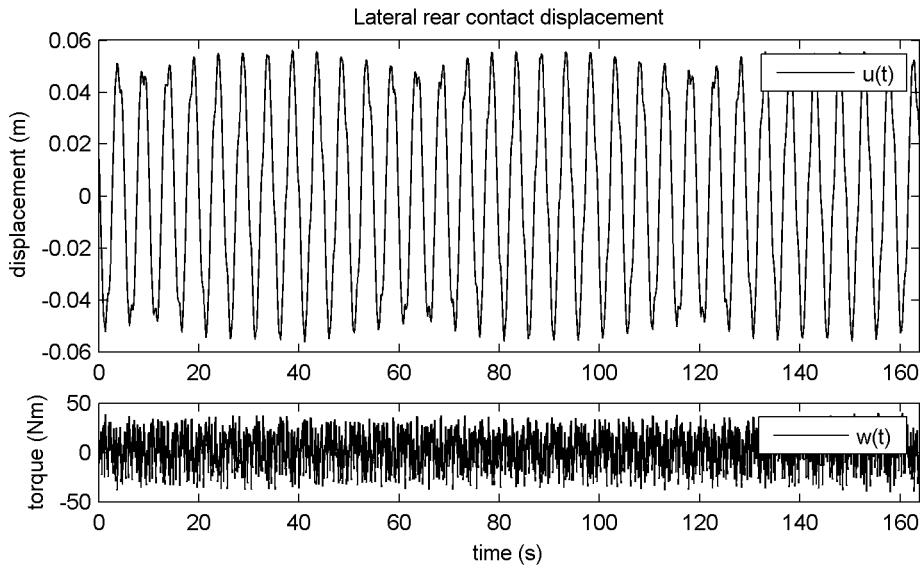


Figure 6-10: Required lateral displacement u as a function of the desired roll perturbation w , with parameters: $h = 1.2$ m, $g = 9.81$ m/s² and $m = 80$ kg.

Unlike the the swing and mass slider designs, since the roll torque no longer has a static contribution. The roll torque is now simply proportional to the combined bicycle/rider mass times the height of the mass center. Notice that for this case the parameters h and m are actually no design parameters, but merely properties of the rider and bicycle.

Next, we will derive the frequency response function from u to T_ϕ . By introducing the Laplace operator for the frequency domain $s = j\omega$ and by making use of equation 6-45 we derive:

$$\frac{T_\phi}{u} = mh\omega^2 . \quad (6-46)$$

The gain increases quadratically with ω , which makes the design most efficient for high frequency perturbation. We also observe that the mechanism has a zero gain frequency at $\omega = 0$, which means that the this particular design is unable to apply a constant torque. The transfer function is used to determine the required lateral displacement of the rear contact point u by using the desired perturbation spectrum $T_\phi = w(t)$. As a rough estimate, we set the combined bicycle/rider mass to $m = 80$ kg centered at a height of 1.2m. The resulting time response is shown in figure 6-10. From this figure we observe that a lateral displacement that a lateral displacement amplitude of ± 0.05 m is required, which is more than reasonable. We also observe that the lowest frequency (0.2 Hz) dominates the lateral displacement amplitude, since the perturbator is less efficient for lower frequencies.

The corresponding force and power can be calculated by using equations 6-3 and 6-4 respectively. However, these results will underestimated the actual required perturbation force and power, since we haven't included the mass of the treadmill. This treadmill might 5 or 10 times as heavy as the total rider/bicycle mass, therefore the obtained force and simulation are not realistic and could easily be a factor 5 higher. Nevertheless, these results are shown in figure 6-11, where the maximum absolute force and power are 33.33 N and 2.04 Watt.

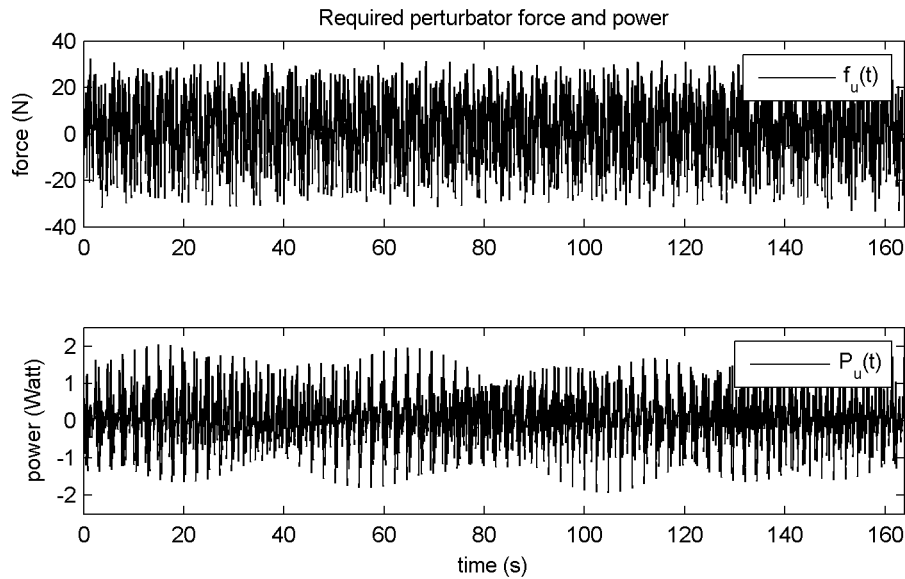


Figure 6-11: Perturbator torque f_u and power P_u as a function of time t , with parameters: $h = 1.2$ m, $g = 9.81$ m/s² and $m = 80$ kg.

6-3-3 Summary

A lateral rear contact point accelerator has been modeled and analyzed. This design uses the inertial properties of the rider/bicycle system to exert a roll torque. The transfer function from roll torque output T_ϕ to lateral contact displacement u has been derived. Here, the roll torque is now simply proportional to the combined bicycle/rider mass times the height of the mass center. The required lateral deviation is obtained, by simulating the desired input roll torque $T_\phi = w(t)$. This results in a required lateral deviation of ± 0.05 m, which is more than reasonable. No passive system contribution is added by the lateral accelerator, since it makes use of the rider/bicycle inertia. In short, the design shows a good performance, but might be hard to implement and may be expensive.

6-4 Design of a rope perturbator

Finally, the rope perturbation method, described in chapter 3, will be analyzed. Only in this case we will mount it in the perturbation plane, so it only results in a generalized roll torque. The rope perturbator uses a simple rope which is attached to the bicycle somewhere in the perturbation plane. By pulling laterally roll torque may be induced on the rider/bicycle system. To induce both positive and negative roll torque, either two ropes should be used for two way pulling, or a stick might be used for pushing and pulling. Since the pulling force is applied externally, the bicycle should either be placed on a treadmill or the pulling should be applied by walking along the forward moving bicycle/rider. The concept is drawn in figure 6-12, for which we skip the equations of motion and move straight on to the analysis.

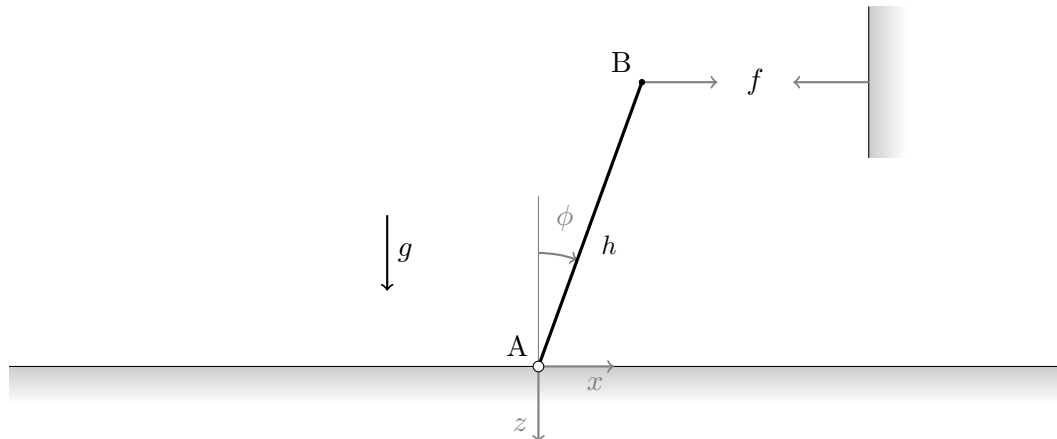


Figure 6-12: Simplified rope perturbator, with; A real wheel contact, B rope connection point, rope force f , moment arm h and where g represents the gravitational acceleration.

6-4-1 Analysis

It can be shown that the roll torque exerted by the pull force f for small angles of ϕ is given by:

$$T_{\phi} = -hf, \quad (6-47)$$

with moment arm h and pull force f , and where the mass of the rope is neglected. This expression is as simple as the mechanism is, since it only requires a treadmill, rope and force sensor.

Since the rope adds only little mass, the passive system contribution is expected to be neglectable.

6-4-2 Summary

A rope type perturbator has been modeled and analyzed. The transfer function from pull force f to roll torque output T_{ϕ} has been derived. The design is very simple and cheap, but requires a connection with the external environment. A simple solution would be a treadmill environment, where the force is manually applied through human power. However, this method seems to be more suited for impulse excitation than for multi sine excitation. The passive system contribution of the rope perturbator is very small and can probably be neglected.

6-5 Comparison

The mechanisms will be compared with each other on a number of criteria, such as performance, implementability, dynamic interaction, etc. Table 6-2 shows an overview of the different perturbator designs, where scores ranging from 1 to 10 (similar to our grading system) are assigned to each criteria. Each criteria will be weighted by its importance, such that all the weighted scores can be added up and reveal which is the best design.

6-5-1 Overview of example calculations

Table 6-1 shows an overview of the performances found for all the examples presented in the previous sections. Not all the results are comparable, since their dimensions do not agree.

	Swing		Slider		Lateral	
$\max x(t) $	0.35	rad	0.12	m	0.06	m
$\max \dot{x}(t) $	2.23	rad/s	0.44	m/s	0.10	m/s
$\max f_x(t) $	65.27	Nm	52.78	N	33.33	N
$\max P_x(t) $	67.22	Watt	12.25	Watt	2.04	Watt

Table 6-1: Overview of the perturbator examples treated in the previous sections. Here x denotes the perturbator degree of freedom, so for the swing example $x = \theta$ and for the slider and lateral accelerator $x = u$.

6-5-2 Design criteria

Each design will be evaluated along a number of design criteria. The criteria will be weighted to make them comparable with each other. For example, performance may be more important than cost. The following criteria are used for the evaluation; performance, dynamic interaction, rider interaction, implementability and cost. In this section, the various criteria will be introduced and described shortly, after which each of the designs will be discussed briefly.

Active system contribution

The performance criterium defines how well the design is capable of applying the desired roll torque disturbance $w(t)$. A perfect score means a perfectly applied roll perturbation signal using the active system contribution. Some designs may have a limited excitation amplitude or bandwidth, which reduces the performance. The active system contribution is the most important criterium, which contributes 40 percent of the overall score.

The example swing and sliding mass designs shows the best active system contribution, since they manage to produce the desired disturbance perfectly. Or at least for the linear case, since the swing example shows swinging angles of over 30 degrees, which probably introduces significant non linearities. The sliding mass is presumably less affected by non linearities, since the slider is truly linear and the deviation is only 0.23 m.

The lateral accelerator does not exert a generalized roll torque but generates some steering torque as well. However this is largely compensated by the great efficiency of the lateral deviation to roll torque transfer function. Here, the example shows that only ± 0.05 m of lateral displacement is required to generate the desired perturbation signal.

The simple rope solution, does not allow for simple allow for automated multi sine perturbation, which results in a poor score. Overall, the performance scores are generally good, except for the rope perturbator.

Passive system contribution

The dynamic interaction criterium defines how much the mechanism interacts with the rider/bicycle apart from the desired roll torque interaction. For example; the swing and sliding mass design, add a lot of inertia to the bicycle, which affects the original bicycle dynamics. A score of 10 is assigned to this criterium, if the design has no dynamic interaction other than the desired roll perturbation. The dynamic interaction is the second most important criterium, and contributes 20 percent of the total score.

Here the lateral accelerator shows a perfect score, since it does not add any Passive system contribution at all. The rope adds only little mass, so the Passive system contribution for this design is expected to be neglectable. The swing and sliding mass mechanism show the poorest scores, since they require an on board perturbator. This perturbator requires a reasonable amount of mass, which introduces addition roll inertia and negative roll stiffness to the system.

Rider Interaction

The rider interaction criterium defines how much the riding behavior of the rider may be affected by the experiment. For example; riding on a treadmill is considered to be stressful and will affect the riding behavior. A score of 10 will be assigned if the perturbator design does not affect the rider behavior at all. The rider interaction will contribute for 15 percent of the total score.

The swing and sliding mass perturbator show the best score for this criterium. This is because these designs allow for outdoor experiments, resulting in maximal freedom. The rope and lateral accelerator designs generally require a lab environment with treadmill. The rope solution might also be performed outside, by applying pull force while running/bicycling next to the subject. In addition lateral accelerator design also tricks the lateral vestibular organ of the rider, which may affect the rider action.

Implementability

The implementability criterium describes how well the design can be implemented. For example; a rope perturbator with force sensor is easy to manufacture, whereas a lateral movable treadmill would be a true design challenge. Obviously, a more easy implementable design gives a higher score. The implementability will contribute for 15 percent of the total score.

Here the rope design scores best, since it has already been implemented in the past and has proven to be an easy method. The swing and sliding mass mechanism are expected to be well implementable, although they probably require a reasonable amount of electronics. The lateral accelerator requires a lateral moving treadmill, which is a big thing to manufacture.

Cost

As with all projects, costs are always an issue. Therefore, we also include the cost criterium. A cheap solution results in a high cost grade, whereas more expensive solutions result in lower grades. The weight factor of the cost criterium is set to 10 percent of the overall score.

Criteria	Weight factor	Swing	Slider	Lateral	Rope
active system contribution	0.40	8	9	8	2
Passive system contribution	0.20	4	4	10	9
Rider interaction	0.15	8	8	4	6
Implementability	0.15	7	8	2	10
Cost	0.10	6	7	2	10
Total score		6.85	7.50	6.30	6.00

Table 6-2: Comparison table showing the criterium scores for each design.

Again, the simple rope solution shows the highest score, since it only requires a rope and force sensor. The lateral accelerator is expected to be the most expensive, since it requires a mechanism which actuates a complete tread mill laterally. The swing and sliding mass perturbator do require some actuating components, sensors, etc. which is assumed to be affordable.

6-5-3 Comparison table

Finally, the criterium scores are assigned for each design. The process of assigning scores to various criteriums is an arbitrary process, which involves a lot of engineering judgment. Therefore, the scores should not be taken to exactly, but they provide more of a rough quantitative estimate of the design performances. The resulting scores are shown in table 6-2. Here, the assigned score for each design/criterium ranges from 1 to 10 (similar to our grading system). From this table, we observe that the sliding mass perturbator shows the best overall score. Therefore, this mechanism is recommended for further development.

6-6 Summary

In this chapter we have introduced and analyzed a number of perturbator designs. The goal of these designs is to apply a desired perturbation signal $w(t)$ as a generalized roll torque T_ϕ to the rider/bicycle configuration. This generalized roll torque can be achieved by only perturbing in the perturbation plane, which is defined in figure 6-1.

4 perturbator designs are presented, namely; the swing, sliding mass, lateral accelerator and simple rope perturbator. The swing and sliding mass perturbator are similar and both introduce an additional degree of freedom and mass. The lateral accelerator uses the mass properties of the rider/bicycle itself by lateral acceleration of the ground contact points. The rope perturbator simply uses a rope mounted to the bicycle frame, which generates roll torque when pulled in a lateral direction.

The designs are evaluated by the following criteria; active system contribution, passive system contribution, rider interaction, implementability and cost. Here, the sliding mass perturbator shows the best overall score and is recommended for further development.

Chapter 7

Discussion

In this chapter an overall discussion is presented. This discussion is divided into two categories, namely; experimental results and experiment design. The first will focus on our obtained results, whereas the second will focus on future identification experiments.

7-1 General control description

First a discussion point about the general control description is given.

- *Rider model does not include co-contraction:* The rider model does not include co-contraction. This type of control was excluded, since it was not expected take during bicycling. However, when looking at the model sensitivity function shown in figure 5-2, we observe high frequency control action around 4 Hz. This is rather high, since the neuromuscular dynamics have a cut-off frequency of around 2 Hz. This kind of high frequency control might be due to co-contraction, which is not limited by the neuromuscular dynamics. Therefore it might be interesting to include co-contraction models in subsequent analysis.

7-2 Experimental Results

In this section the experimental results are discussed.

- *No pure roll excitation during the experiment:* During the experiments, the rope perturbator is mounted below the seat, which is not situated within the perturbation plane presented in chapter6. Therefore, the rope perturbator does not exert a pure roll torque, but also results in a small steering torque component. The succeeding system identification does take into account for this small steering torque component, but the experiment design does not. Here the perturbed steering torque component is simply

neglected. However, since the steering torque component $T_{\delta,w}/f = 0.014$ is rather small compared with the roll torque component $T_{\phi,w}/f = 0.91$, this could be neglectable. On the other side, the system is known to be much more sensitive for steering torque excitation than for roll exciton, which increases the effective influence.

- *Poor non parametric roll angle identification:* The estimated impulse response function for the roll angle was estimated poorly for most cases. These impulse responses are shown in figures 4-2, 4-3, 4-4, and 4-5. These poor results might caused by increased sensory noise for the roll angle, since the roll angle presumably is way more difficult to measure than steering angle. If the subject would be unable to sense the roll angle correctly, he will be unable to apply proper roll angle feedback, resulting in more stochastic roll response. Only for the case of $v = 3.2$, the roll angle response showed a reasonable signal to noise ratio. However, this measurement is performed with a different rider and task instruction, which could affect the outcome.
- *Poor experimental results at low velocities:* The experimental data obtained for a forward velocity of $v = 2.1$ m/s where of poor quality. Here, the impulse response function for both the roll and steering angle response where dominated by noise, rendering them useless for subsequent parametric modeling. An explanation for these poor results might be given by the increased bicycle instability for low forward velocities. This requires a lot more of active stabilization, which dominates the output, which results in a poor signal to noise ratio. This ration might be improved by using more excitation power and longer measurements.
- *Different riders and task instructions used:* Table 3-2 shows that one of the measurements (at $v = 3.2$ m/s) is performed with a different rider and task instruction. The task instruction for this trial was set to straight line tracking while being disturbed, whereas others tasks where about roll stabilization while being disturbed. However, since the measurements where all performed on a rather small horse treadmill, they all require some sort of heading control. This is also observed when looking at the parametric results, where heading control in terms of negative integrative steering feedback is observed for all cases. Still, since the task instructions differ, they might be hard to compare with each other.
- *Passive rider model used:* Despite the availability of complex passive rider models, a simple rigid rider model is used. Here, the inertial and stiffness contributions of the to the steering angle are neglected. Whereas the more complex passive riders models described in section 2-1 do include these properties. These more complicated rider models are also explained in more detail in Schwab et al. (2011).

7-3 Parameter Estimation

Here we present some discussion about the process of estimating the parameters.

- *Parameter interdependency:* The parameter covariance matrix reveals the interdependency between the obtained parameters. If the covariance matrix would only have diagonal entries, it means that the parameters are independent of each other. In our

case, there are off diagonal terms present which indicate parameter dependencies. This results in non-consistent results when reducing the set of parameters using parameter reduction techniques. If a parameter is removed, the dependent parameters may fill up the empty parameter space, which may explain for the parameter variations through the reduction steps. This might be solved by introducing a set of orthogonalized parameters, based on the eigenvectors of the Hessian covariance matrix stated in equation 4-24. By doing so, the least contributing parameters can be eliminated, without affecting the other.

- *Parameter uncertainty for identification results:* The parameter covariance matrices obtained during the system identification analysis are under estimated. Here, the underlying covariance theory assumes an error which is according to a white noise normal distribution. However, since we removed the noise at an early stage (non-parametric modeling) these assumptions do not hold and result in an underestimation of the true parameter covariance. This is not an issue for the parameter reduction, since only the relative covariance is of importance here and not the absolute (underestimated) covariance. Later on, the unbiased covariance for the frequency domain is derived by using a separate noise model and analytic parameter sensitivity expressions, which is recommended for future use.
- *Parameter reduction failed for $v = 4.3$ m/s:* The parametric model obtained for a forward velocity of 4.3 m/s could not be successfully reduced by more than 2 parameters, resulting in a 6 parameter model. This was unexpected, since the parametric models for $v = 3.2$ and $v = 7.4$ could both be reduced by 4 parameters, where the roll angle and rate, integral action on the steering angle and steering rate form the reduced parameter set. The same parameters were also present for $v = 4.3$ m/s case, but in addition we also have a positive roll acceleration and steering angle gain. The roll acceleration term was unexpected, which might be caused by modeling errors in the inertia matrix.

However, it can be shown that the system can be stabilized by only 4 parameters, using optimal control theory. Since the parameter estimation was constantly running into unstable parameter configurations, we might fix the optimization by including a constraint on the stability. By doing so, we might be able to successfully, reduce the parameter set by one or two parameters. Another possibility would be to orthogonalize the parameters set, by introducing a new set of parameters and then perform parameter reduction techniques.

- *Influence of time delay on parametric outcome:* During the parametric model estimation, there were some issues with the time delay. A pure time delay resulted in an unstable system, so therefore we either neglected or approximated (using Pade approximation) the time delay. Analysis of the parametric results for both cases shows only minor changes in VAF, but significant changes in the estimated parameters. When comparing the reduced set of parameters for $v = 3.2$ m/s (same experiment), shown in table 4-1 for both cases, we observe changes of up to 30% between similar parameters. Apparently the absence of time delay, is being compensated by adjusting the parameters.

7-4 Parametric Results

Next some parametric results are discussed.

- *Steer into the fall:* The steer into the fall principle is observable in the positive roll angle gain $k_{\phi p}$ and positive roll rate gain $k_{\phi d}$ for all measurements. From figure 4-15 we observe that the roll perturbation only results in a initial roll velocity. Therefore, the roll rate feedback dominates the initial response, which is key to stabilizing the system. At $t = 0.2s$ the roll angle reaches an initial peak, for which the roll feedback gain start to kick in. The combined roll angle and rate feedback result in the stabilizing steer into the fall mechanism, which is also described in section 2-1-3.
- *Heading control:* The heading control is already discussed in section 4-3-2, from which we demonstrated that the integrative steering action acts as an controller on the heading. Here the heading is controlled by applying counter steering, where the turn is removed by applying a steering torque in the same direction, resulting in a turn in the other direction. Concludingly, the steering integral action acts as controller on the heading angle. This heading control is necessary, since the experiment was performed on a rather narrow horse treadmill, allowing for only little changes in heading an lateral displacement.
- *Key contributors:* The roll angle $k_{\phi p}$, roll rate $k_{\phi d}$, steering rate $k_{\delta d}$ and steering angle integral $k_{\delta i}$ gains are the key contributors and cannot be removed without causing a major drop of the VAF value for any case. Removal of any of these parameters results in instability, which is no feasible result, since the measured bicycle/rider configuration is observed to be stable. Parameter reduction affects the parameter values relatively to the unreduced parameters, but all the signs remain conserved. This is probably due to the off-diagonal terms observed in the parameter covariance matrices, which indicate parameter dependency. If a parameter is removed, the dependent parameters fill up the empty parameter space, which explains for the parameter variations through the reduction steps. This might be solved by introducing an orthogonal parameters set, for which the least contributing parameters can be eliminated, without affecting the other parameters due to orthogonality.
- *Derivative feedback on the steering angle:* As stated before, we have identified 4 key contributors, roll angle and rate feedback and integrative and derivative steering angle feedback. The roll angle and rate can be explained by the steer into the fall principle, whereas the integrative action on the steering angle effectively acts as a controller on the heading angle. However, the derivative action on the steering angle remains less understood. Effectively it acts as a low pass (due to neuromuscular dynamcis) damper on the steering angle, so it could remove oscillatory steering motion. However, it might also be due to co-contraction, which is omitted in the parametric model. Co-contraction may result in added stiffness and damping onto the steering angle, for which the damping may be modeled as derivative action on the steering angle. Therefore it is recommended that the co-contraction mechanism should modeled separately in the parametric model.

7-5 Experiment Design

In this section some issues about the experiment design are discussed.

- *Input amplitude:* The maximum input amplitude is set to 40 Nm, which corresponds to a maximum roll angle deviation of around 3 degrees and steering angle deviation of 10 degrees. These deviations are rather small, which ensures both safety and geometrical linearity, but it also results in a relatively poor signal to noise ratio. However, it would be nice if we would be able to apply more intense perturbations, of around 60 or 80 Nm. This could be helpful in detecting non-linearities and will help to create a better signal to noise ratio. However, this might also increase the passive contribution to the system, but still it would be interesting. Concludingly, it would be nice if the perturbation design, allows for optional perturbation power. For example, this could be achieved by adding some additional mass to the perturbator.
- *Estimation of individual parameter variance:* It would be nice to estimate the individual parameter variance prior to the identification experiment. Here we already have all the ingredients to do so, namely; noise spectrum, input spectrum and parameter sensitivity of the model. This can be combined to form the covariance matrix, which is stated in chapter 5. However, this matrix yields information of the interdependent parameter covariance, where we like to know the individual covariance. We could circumvent this problem by introducing a new set of orthogonal parameters, such that the covariance matrix only consists of diagonal terms. For this case, the diagonal terms are equal to individual parameter variance. It would be interesting to project these variances onto the original set of parameters to get an idea about the individual parameter variance.

7-6 Perturbator Design

In this section some discussion about the design of an perturbator is presented.

- *Comparing designs:* The 4 different perturbation designs are compared with each other based on a number of criteria. These criteria include; active and passive contribution, rider interaction, implementability and cost. Different weighting factors are assigned to these criteria to make them comparable with each other. However, the assigning of weighting factors and criteria scores is a bit arbitrary. Therefore, the overall scores should not be taken to explicitly.
- *Cresting of the sliding displacement:* The example calculation for the sliding mass perturbation discussed in section 6-3-2 shows a required lateral displacement of ± 0.10 m. However, by cresting the signal, we can reduce this displacement to ± 0.12 m, while maintaining the same input spectrum. This is an maximum amplitude reduction of around 15%, while maintaining the same input power. Since slider displacement is considered the restricting factor, the input signal should be crested onto the sliding displacement u .

Conclusions and Recommendations

In this chapter we present a number of conclusions and recommendations.

8-1 Conclusions

In section we present a number of conclusions that can be drawn from this MSc research project. The goal of this research was to estimate the human controller in bicycling. Using experimental data from our colleagues of the UC Davis, California, we indeed have identified the human controller.

8-1-1 Literature analysis

Prior to the experimental data analysis, a number of rider models obtained from literature where used for simulation studies, which is described in appendix A. Interestingly, the models presented by van Lunteren and Stassen (1970) and Stassen and Lunteren (1973) where found to contain some sign errors.

- *Sign error in roll equation:* The steering related bicycle terms the roll equation, described in (van Lunteren and Stassen, 1970), contains a sign error. The Stassen and Lunteren roll and steering angle definitions are in accordance with the benchmark convention, where steering to the right and rolling to the right are both defined positively. However, when analyzing the roll angle equation, we observe that a positive steering angle will result in a positive roll moment. This is incorrect, since the roll moment should be of opposite sign, due to the centripetal force generated by the turn. Closer inspection reveals a sign error in the roll angle equation, where the steering angle related terms should be of opposite sign. This error is fixed, after which the simulation study (section A-1) is continued.

- *Stability issues (Stassen and Lunteren, 1973; van Lunteren and Stassen, 1970)*: The corrected bicycle model and proposed rider model, described in van Lunteren and Stassen (1970), were both implemented in Matlab, but were found to be unstable. First, we omitted the time delays, since these generally have a negative impact on stability. The corresponding eigenvalue analysis of the combined rider/bicycle system indicated that the system was still unstable. After playing around with the undelayed rider model, it was found that the combined bicycle/rider system could simply be stabilized by changing the sign of the upperbody lean controller.

In addition, the 'unbiased' rider model, described in Stassen and Lunteren (1973), is also analyzed and implemented. This model has exactly the same stability issues as the previous rider model (van Lunteren and Stassen, 1970). Again this rider/bicycle model could simply be stabilized by changing the sign of the upper body lean controller. These issues might be due to sign errors, since changing the sign stabilizes the undelayed rider/bicycle models.

Finally the time delays were reimplemented to the fixed rider models, but again this resulted in unstable behavior. Even when replacing the time delays by a second order Padé approximation resulted in unstable dynamics. Concludingly, it appears that the Lunteren and Stassen model is inherently unstable.

8-1-2 System description

- *System description*: The system description shown in figure 2-6 proved to be a useful tool for describing the combined rider/bicycle system. This description separates the known bicycle and passive rider properties from the unknown active rider contribution. In addition the model also allows for easy implementation of an external disturbance signal. This description proved to be a useful tool and is recommended for future rider/bicycle research.

8-1-3 Rider control

In this section the most important conclusions about the actual rider control are presented.

- *Stabilizing the bicycle*: The rider makes use of the steer in to the fall principle for stabilizing the bicycle. From the experimental dataset, we have obtained a number of parametric models for forward velocities of $v = 3.2$, $v = 4.3$ and $v = 7.4$ m/s. These parametric models all show positive roll angle and rate feedback onto the steering torque output. This effectively results into a steering action in the direction of falling.
- *Controlling the heading*: The integrative steering action controls the heading by applying counter steering. In section 4-3 it is shown that the integral action is roughly proportional to the heading angle. Since the integral action is positive, this means that the rider exerts steering torque into the direction of the turn. By doing so, the rider effectively applies a counter steering action mechanism, resulting in a turn in the other direction. Concludingly, the steering integral action effectively acts as a controller on the heading angle. This heading control is necessary, since the experiment was performed on a rather narrow horse treadmill.

8-1-4 Experiment Design

In this section the most important conclusions about the design of an frequency domain experiment are presented.

- *Measurement settings:* The measurements settings are determined in section 5-4 The experiment should be recorded at a sampling frequency of 200 Hz, which is high enough to encapsulate the human controller dynamics. This corresponds to a time resolution of $\Delta T = 0.05$ s. The measurement length is set to $N = 2^{15}$ samples, which corresponds to a total measurement time of $T = N\Delta T = 163.84$ s. The experiment should be performed at forward velocities of $v = 2, 3, \dots, 7$ m/s, since the dynamic behavior is velocity dependent.
- *Input signal design:* A disturbance input signal has also been designed, and should be applied as a generalized roll torque to the system. In order to prevent feed forward control, the input signal should be appear to be random, which can be achieved by superimposing 5 multi sines or more. The input bandwidth ranges from 0.2 to 4 Hz, where the human controller is most sensitive in the parameters. The input power is scaled such that $\max |w(t)| = 40$ Nm, which corresponds to a maximum absolute roll angle deviation of 3 degrees and steering angle deviation of 10 degrees for a forward velocity of 3.2 m/s. The resulting input signal is shown in figure 5-5 and 5-6.

8-1-5 Perturbator design

In this section some conclusions about the recommended perturbator are presented.

- *Recommended perturbator:* The sliding mass perturbator, described in section 6-2, is recommended for future frequency domain identification experiments. This perturbator should be well capable of applying the desired input signal $w(t)$, defined in section 5-5. The perturbator does add some roll inertia and negative roll stiffness, but these contributions are relatively small compared with the original roll inertia and stiffness. The implementation might give some difficulties, since it requires a linear actuator. Another option would be the swing type perturbator, which is described in section 6-1. This design shows a lot of similarity with the sliding mass perturbator, since it also uses an additional mass for perturbation. The performance however is slightly poorer, but the design might me easier to implement since it requires an angular actuator

8-2 Recommendations

Finally we present a number of recommendations, which might be useful for future research.

- *Orthogonalize parameters:* The parameter covariance matrix reveals an interdependency between the obtained parameters. This interdependency makes the parameter reduction non-consistent, where the elimination of one parameter may affect the value of the other parameters. The results in parameter variations through-out the reduction steps,

as can be seen in table 4-1. Therefore, it is recommended to introduce an orthogonal parameter set, which is a linear combination of the old parameters. This will result in a more consistent parameter reduction sequence. In addition, the parameter variance estimation becomes trivial, since the parameter variances are now simply defined as the diagonal terms of the covariance matrix.

Next, we will show that it is possible to reparameterize the system by choosing some arbitrary set of parameters $\boldsymbol{\theta}'$, which is a linear combination of the parameters $\boldsymbol{\theta}$, such that:

$$\boldsymbol{\theta}' = \left[\frac{\partial \boldsymbol{\theta}'}{\partial \boldsymbol{\theta}} \right] \boldsymbol{\theta}, \quad (8-1)$$

where $\partial \boldsymbol{\theta}' / \partial \boldsymbol{\theta}$ should be invertible. This result may be substituted in equation 5-5, which yields:

$$\begin{aligned} \text{cov } \boldsymbol{\theta} &= \frac{1}{N} \left[\sum_{k=1}^N \left[\frac{\partial G}{\partial \boldsymbol{\theta}} \right]^T \frac{\hat{\Phi}_w^N}{\hat{\Phi}_v^N} \left[\frac{\partial G}{\partial \boldsymbol{\theta}} \right] \right]^{-1}, \\ &= \frac{1}{N} \left[\sum_{k=1}^N \left[\frac{\partial G}{\partial \boldsymbol{\theta}'} \frac{\partial \boldsymbol{\theta}'}{\partial \boldsymbol{\theta}} \right]^T \frac{\hat{\Phi}_w^N}{\hat{\Phi}_v^N} \left[\frac{\partial G}{\partial \boldsymbol{\theta}'} \frac{\partial \boldsymbol{\theta}'}{\partial \boldsymbol{\theta}} \right] \right]^{-1}, \end{aligned} \quad (8-2)$$

where $G = G_N(e^{i\omega_k})$, $\hat{\Phi}_v^N = \hat{\Phi}_v^N(\omega_k)$ and $\hat{\Phi}_w^N = \hat{\Phi}_w^N(\omega_k)$. Since the linear parameter transformers $\partial \boldsymbol{\theta}' / \partial \boldsymbol{\theta}$ are independent of the summation, we can move them to the left hand side, resulting in the parameter covariance expressed in the new set of coordinates:

$$\text{cov } \boldsymbol{\theta}' = \left[\frac{\partial \boldsymbol{\theta}'}{\partial \boldsymbol{\theta}} \right]^T \text{cov } \boldsymbol{\theta} \left[\frac{\partial \boldsymbol{\theta}'}{\partial \boldsymbol{\theta}} \right] = \frac{1}{N} \left[\sum_{k=1}^N \left[\frac{\partial G}{\partial \boldsymbol{\theta}'} \right] \frac{\hat{\Phi}_w^N}{\hat{\Phi}_v^N} \left[\frac{\partial G}{\partial \boldsymbol{\theta}'} \right]^T \right]^{-1}. \quad (8-3)$$

Since $\boldsymbol{\theta}'$ represents an arbitrary linear combination of $\boldsymbol{\theta}$, we are still free to choose this parameterization. One particularly interesting parameterization would be to define a linear combination of parameters, such that $\text{cov } \boldsymbol{\theta}'$ is orthogonal. This can be achieved by performing an eigenvalue decomposition of $\text{cov } \boldsymbol{\theta}$, which results in a set of eigenvalues and eigenvectors. The eigenvectors define the linear transformation $\partial \boldsymbol{\theta}' / \partial \boldsymbol{\theta}$ and the eigenvalues define the orthogonalized covariance matrix $\text{cov } \boldsymbol{\theta}'$.

- *Co-contraction*: The rider model does not include co-contraction. This type of control was excluded, since it was not expected to occur during bicycling. However, when looking at the model sensitivity function shown in figure 5-2, we observe high frequency control action around 4 Hz. This is rather high, since the neuromuscular dynamics have a cut-off frequency of around 2 Hz. This kind of high frequency control might be due to co-contraction, which is not limited by the neuromuscular dynamics. Therefore, it would be interesting to reexamine the possibility of implementing co-contraction models in subsequent analysis.
- *Analyze closed loop eigensolutions*: In section 4-3 we already analyzed the closed loop parametric system stability in terms of the eigenvalues. However, it would be interesting to also analyze the corresponding eigenvectors to gain a better understanding of the motions involved. This analysis is omitted due to time limitations, but it would be interesting to see these eigenmotions visualized in future research.

- *Optimal Control Objectives:* According to Kleinman et al. (1970) human controllers show some form of optimal control. A simple example of an optimal control solution is given in appendix A-2. In stead of specifying the gains of the controller directly, optimal control theory only requires specification of the control objectives. These objectives may be translated into a criterium function, which consists both a performance \mathbf{Q} and control effort \mathbf{R} weightning matrix. This criterium can be minimized analytically which results into an optimal gain matrix \mathbf{K} . Since we already estimated the rider gains directly, it would be interesting to find out what the underlying objectives are. For example; does the rider applies tight control (high control effort, good performance) or loose control (low control effort, poor performance). Or when analyzing the performance matrix \mathbf{Q} ; does the human controller tries to minimize the roll angle or rate and is heading control also part of the control objectives? By answering these questions, we may obtain a deeper understanding of the underlying objectives of the human controller.
- *Identifying non-linearities:* The performed analysis is performed almost exculsively in the linear regime, where non linearities are omitted. For future research it would be interesting to identify and analyze the non linearities present in the system. A number of non-linearities may be present in the system, for example:
 1. non linear scaling
 2. intermittent control
 3. input type dependent control (e.g. multisine, impulse, step response, etc.)

The first type may be easily identified by experimenting with different input amplitudes and check wether the output response scales linearly. The second may be harder to identify and may require non linear model estimation, where a non linear parametric model is directly fitted onto the data. THE third type of non linearity may be due to the adaptive behavior of the human controller as a function of the input type. Here, it would be interesting to perform a linear identification for various input signals and compare these results with each other.

In addition there also might be other non linearities, which are not stated in this list such such as time varying behavior due to the learning effect or external causes which may affect rider control, such as drug and alcohol use.

- *Identifying non-linearities:* According to Andy Ruina of Cornell University it would also be interesting to design a tricycle which mimics the dynamic behavior of a bicycle. Here, the front fork and wheel configuration are be similar to an ordinary bicycle, but the rear wheel are replaced by two parallel wheels. These rear wheels should not be connected rigidly to the frame, since that would constrain the roll motion. In stead the rear wheels and frame should be connected by a four bar mechanism, where the four bar mechanism is placed such that the fear frame rotates right between the two rear contact points. By doing so, the rear frame will rotate around the rear wheel contact point of an ordinary bicycle, which corresponds to roll motion. However, the mechanism will also introduce more negative stifnesss and less roll inertia, since the location of the center of rotation changes as an function of the roll angle. This design may be used for perturbation experiments, by simply adding an perturbator between the rear wheel axis and rear frame, which allows for roll torque excitation.

Appendix A

Additional rider model analysis

In this appendix some additional analysis concerning rider models is presented. This done for the PID controller according to Stassen and Lunteren (1973) and for the optimal controller according to Schwab et al. (2008). For various reasons, both controllers turned out to be of limited use for combined rider/bicycle simulations. However, analysis of these models revealed some interesting observations concerning stability, sign errors in literature, etc. Therefore it is decided to include this analysis as an appendix in this report.

A-1 Lunteren and Stassen controller

This section describes the implementation of the Lunteren and Stassen controller according to van Lunteren and Stassen (1970); Stassen and Lunteren (1973). The controller by van Stassen and Lunteren describes experimentally based rider control in bicycling. The experiments are all performed at a fixed forward velocity of 15 km/h. This model will serve as an first estimate of rider control action and will help us in designing a proper perturbation input signal.

A-1-1 Control model

The block diagram in figure A-1 shows the man machine interaction by Lunteren and Stassen. The controller \mathbf{C} outputs the steering angle δ and rider lean angle θ as a function of the roll angle ϕ . By doing so, the controller acts as a constraint on both the steer and lean angle, reducing the degrees of freedom by two. As a result, the roll angle remains the only degree of freedom. Therefore the equations of motion of the bicycle are reduced to:

$$m_{11}\ddot{\phi}(t) + c_{11}\dot{\phi}(t) + k_{11}\phi(t) = T_{\phi}(t) - \underbrace{\left(m_{12}\ddot{\delta}(t) + c_{12}\dot{\delta}(t) + k_{12}\delta(t)\right)}_{\text{Steering interaction}} - \underbrace{\left(m_{13}\ddot{\theta}(t) + c_{13}\dot{\theta}(t) + k_{13}\theta(t)\right)}_{\text{Rider lean interaction}}, \quad (\text{A-1})$$

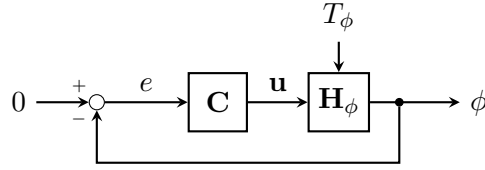


Figure A-1: Block diagram of the man machine interaction adapted to Lunteren and Stassen, with human controller \mathbf{C} , roll dynamics \mathbf{H}_ϕ , error e , system input $\mathbf{u} = [\delta, \theta]^T$, roll torque T_ϕ and roll angle output ϕ .

where m_{ii} , c_{ii} , k_{ii} represent the system coefficients corresponding to roll angle ($i = 1$), steering angle ($i = 2$) and rider lean ($i = 3$). Since the lean and steer interaction is moved to the right hand side, since these variables are prescribed by the controller. The roll torque is represented by T_ϕ , which acts as an external torque onto the system. For control purposes the system is converted to the Laplace domain, which yields:

$$\mathbf{H}_\phi(s) = \begin{bmatrix} \frac{1}{m_{11}s^2 + c_{11}s + k_{11}}, & \frac{m_{12}s^2 + c_{12}s + k_{12}}{m_{11}s^2 + c_{11}s + k_{11}}, & \frac{m_{13}s^2 + c_{13}s + k_{13}}{m_{11}s^2 + c_{11}s + k_{11}} \end{bmatrix}, \quad (\text{A-2})$$

where zero initial conditions are assumed. This transfer function is defined such that

$$\phi(s) = \mathbf{H}_\phi(s) \begin{bmatrix} T_\phi(s) \\ \mathbf{u}(s) \end{bmatrix}, \quad (\text{A-3})$$

where $\mathbf{u}_\phi = [\delta, \theta]^T$. Next, the controller is given by;

$$\mathbf{C}(s) = - \begin{bmatrix} H_1(s) \\ H_2(s) \end{bmatrix}, \quad (\text{A-4})$$

where H_1 and H_2 represent the steer and rider lean transfer functions provided by Lunteren and Stassen (see next section). This controller \mathbf{C} is defined according to the following input/output relation;

$$\mathbf{u}(s) = \mathbf{C}(s)e(s), \quad (\text{A-5})$$

where $e = -\phi$ represents the roll angle error. Next, the two rider and bicycle models are evaluated by analyzing the closed loop poles of the combined system. A suitable rider/bicycle combination is chosen, which is subjected to further analysis.

Rider model

The two rider models subject to stability analysis are given by Stassen and Lunteren (1973) are shown in table A-1. The steering related bicycle parameters of the simulator (c_{12} and k_{12}) are found to contain a sign flaw, which is corrected for the simulation model. It can be shown that these signs are incorrect, because a positive steering angle should give negative roll moment. This is due to the centripetal force generated by the turn, when using the benchmark sign convention.

n	year	$H_{\delta n}(s)$	$H_{\theta n}(s)$
1	1969	$1.07(1 + 0.15s)e^{-0.16s}$	$0.13(1 + 1.6s)e^{-0.09s}$
2	1972	$3.6e^{-0.074s}$	$3(1 + 0.052s)e^{-0.026s}$

Table A-1: Corrected results for the rider models according to Stassen and Lunteren (1973). De signs of the H_{θ} controllers are changed, since their action was destabilizing the system. This is probably due to a sign error in the original articles.

Symbol	van Lunteren and Stassen (1970)	Batavus Stratos
$[m_{11}, c_{11}, k_{11}]$	[109, 0, -940]	[87.92, 0, -806.9]
$[m_{12}, c_{12}, k_{12}]$	[0, 104.2, 998.3]	[2.4, 164.6, 1306]
$[m_{13}, c_{13}, k_{13}]$	[23.9, 0, -162]	[15.74, 0, -117.5]

Table A-2: Corrected coefficients of the roll dynamics equation (eq. A-2). The terms proportional to the steering angle given by Lunteren and Stassen are corrected by changing the sign

Bicycle model

The bicycle parameters of the roll angle dynamics (equation A-2) of the two bikes are given in table A-2. The rider model also appears to contain a flaw, since the proposed controllers are both found to be unstable. This stability issue can be solved by changing the sign of the H_{θ} controller, resulting in a stable combined rider/bicycle system .

Closed loop analysis

A closed loop pole analysis is performed to analyze the stability of the system. Next we want to check the stability of the closed loop system with respect to roll torque perturbation T_{ϕ} . Since all analysis is done in the Laplace domain, the complex argument will be omitted from now on. Starting of with equation A-3 and making use of equation A-5 we derive;

$$\begin{aligned}
 \phi &= \mathbf{H}_{\phi} \begin{bmatrix} T_{\phi} \\ \mathbf{u} \end{bmatrix} \\
 &= \mathbf{H}_{\phi} \begin{bmatrix} T_{\phi} \\ \mathbf{C}e \end{bmatrix} \\
 &= \mathbf{H}_{\phi} \begin{bmatrix} T_{\phi} \\ -\mathbf{C}\phi \end{bmatrix}.
 \end{aligned} \tag{A-6}$$

In order to solve for ϕ we need to separate the system matrix \mathbf{H} in terms of $H_{T_{\phi}}$ and $\mathbf{H}_{\mathbf{u}}$, which are corresponding to T_{ϕ} and \mathbf{u} respectively;

$$\mathbf{H}_{\phi} = [H_{T_{\phi}}, \mathbf{H}_{\mathbf{u}}]. \tag{A-7}$$

	\mathbf{C}_1	\mathbf{C}_2
$\mathbf{H}_{\phi 1}$	-23.9534	-46.7246
	-1.2298	-0.8706 + 3.4184i
	-0.7312	-0.8706 - 3.4184i
$\mathbf{H}_{\phi 2}$	-29.3204	-54.7641
	-1.5918 + 1.6804i	-1.8941 + 4.7689i
	-1.5918 - 1.6804i	-1.8941 - 4.7689i

Table A-3: Poles for the different rider/bicycle combinations. With rider models \mathbf{C}_1 (1969) and \mathbf{C}_2 (1973) according to Stassen and Lunteren (1973). These rider models are combined with the Lunteren and Stassen bicycle $\mathbf{H}_{\phi 1}$ and Batavus Stratos bicycle $\mathbf{H}_{\phi 2}$. The rider time delays are omitted, resulting in a stable set of poles for all combinations.

Now we can continue solving for ϕ ;

$$\begin{aligned}
\phi &= [H_{T_\phi}, \mathbf{H}_u] \begin{bmatrix} T_\phi \\ -\mathbf{C}\phi \end{bmatrix} \\
&= H_{T_\phi} T_\phi - \mathbf{H}_u \mathbf{C} \phi \\
&= \frac{H_{T_\phi}}{1 + \mathbf{H}_u \mathbf{C}} T_\phi.
\end{aligned} \tag{A-8}$$

So the closed loop transfer function of ϕ with respect to T_ϕ becomes:

$$\frac{\phi}{T_\phi} = \frac{H_{T_\phi}}{1 + \mathbf{H}_u \mathbf{C}}. \tag{A-9}$$

The roll angle will be stable with respect to a roll torque perturbation if the real part of the poles of this transfer functions are all negative. Unfortunately our human controller contains time delays (see next section), which prevents us from doing a relatively simple pole analysis. The presence of time delays complicates the stability analysis, since the system effectively has infinite poles due to the time delays. However to get an first estimate for the stability the time delays are first neglected and a simple pole analysis is performed. After correcting both the Lunteren and Stassen bicycle and rider models, the resulting closed loop poles are given in table A-3.

Model selection

Next a suitable rider and bicycle model will be selected for future analysis. According to Stassen and Lunteren (1973) the rider model from 1969 is derived using an biased methods, thereby introducing errors in the estimation procedure. Later on Lunteren and Stassen improved their estimation methods, resulting in the unbiased human controller \mathbf{C}_2 . This controller provides a more realistic estimate and therefore will be used for future analysis. The rider model will be used in combination with the Batavus Stratos bicycle model, because this bicycle will be used for future experiments. This combination is shown to be stable, making it suitable for future simulations. So in short, the following choices are made:

$$\mathbf{C} = \mathbf{C}_2 \tag{A-10}$$

$$\mathbf{H}_\phi = \mathbf{H}_{\phi 2} \tag{A-11}$$

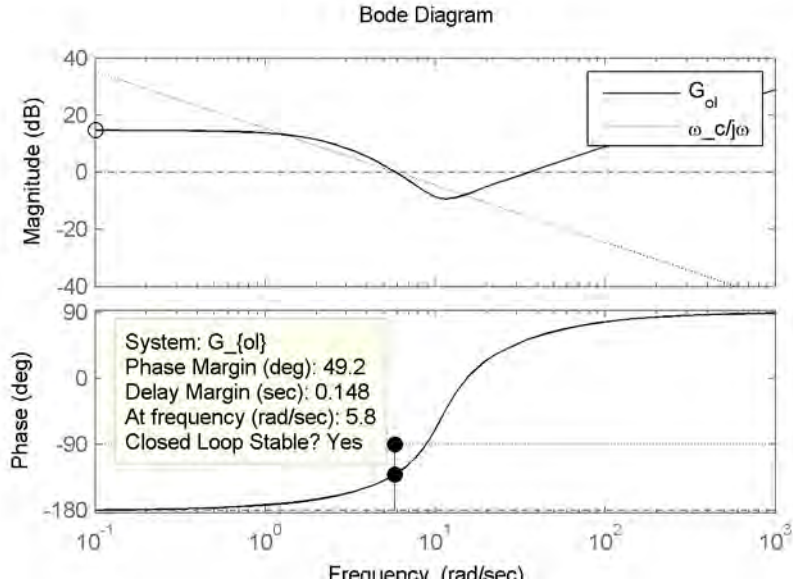


Figure A-2: Bode diagram of the openloop transferfunction G_{ol} and crossover function $\omega_c/j\omega$. The crossover frequency is identified to be 5.8 rad/s. The -2 slope of the open loop transferfunction does not match the prescribed -1 slope by McRuer. At higher frequencies the magnitude keeps on rising, leading to unrealistic feedback gains.

Open loop analysis

Next the selected rider/bicycle combination is subjected to an open loop analysis. This is interesting since McRuer states that the openloop transferfunction of the combined man machine system should act as an integrator around the cross over frequency ω_c :

$$\tilde{L} \approx \frac{\omega_c}{j\omega} : \text{near } \omega_c, \quad (\text{A-12})$$

where \tilde{L} is the expected loop transferfunction of the man machine system. The open loop transferfunction L of the combined system is given by:

$$L = \mathbf{CH}_\phi, \quad (\text{A-13})$$

with input e and output ϕ . The expected and resulting open loop and transfer functions are shown in figure A-2. This figure shows that the resulting loop transfer function has a -2 slope, whereas a -1 slope was expected according to McRuer theory. The crossover frequency is $\omega_c = 5.8$ [rad/s], which is a plausible frequency according to McRuer and Jex (1967).

Impulse analysis of lean torque

The lean action is investigated by analyzing the lean impulse reaction of the Batavus Stratos bicycle. At t_0 the system is in a static upright position, resulting in initial configuration $\mathbf{q} = [0, 0, 0]^T$ and velocities before the impulse $\dot{\mathbf{q}}^- = [0, 0, 0]^T$. Next a relative lean impulse

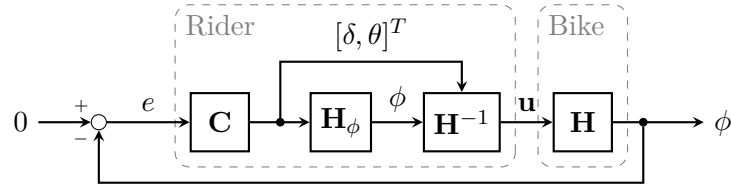


Figure A-3: Block diagram of the man machine interaction adapted to Lunteren and Stassen, with human controller \mathbf{C} , roll dynamics \mathbf{H}_ϕ , bicycle dynamics \mathbf{H} , error e , disturbance torque w , bicycle input $\mathbf{u} = [T_\phi, T_\delta, T_\theta]^T$ and roll angle output ϕ .

moment is applied, resulting in a change in velocity according to

$$\dot{\mathbf{q}}^+ = \dot{\mathbf{q}}^- + \mathbf{M}^{-1}\mathbf{s} = \begin{bmatrix} -0.0980 \\ -0.0875 \\ 0.5606 \end{bmatrix} \text{ [rad/s]} \quad (\text{A-14})$$

where $\dot{\mathbf{q}}$ are the generalized velocities after the applied impulse, \mathbf{M} is the generalized mass matrix and $\mathbf{s} = [0, 0, 1]^T$ is a unit lean impulse vector. From this result we see that an unit lean torque impulse results in an negative steer rate. Since steering into the direction of fall is the dominant method for stabilization, the lean pulse should be applied counteracting to the direction of falling. In short; falling to the left can be counteracted by leaning to the right and vice versa.

A-1-2 Reformulation of the rider model

Next the rider model will be reformulated into a more general form, where the desired configuration error is the input and steering and lean torque are the outputs. The block shown in figure A-1 is modified such that it outputs rider torques. This block diagram and corresponding definitions are shown in figure A-3. From this block diagram we derive the rider input output relation is given by:

$$\mathbf{u} = \mathbf{H}^{-1} \begin{bmatrix} \mathbf{H}_\phi \\ \mathbf{I} \end{bmatrix} \mathbf{C}e, \quad (\text{A-15})$$

with $\mathbf{H}_\phi = \mathbf{H}_\mathbf{u}$, since there is no external roll torque present withing the human controller. In figure A-3 a bode diagram of the rider action is shown. At $\omega = 0$ [rad/s] the steering torque output returns $T_\delta/e|_{\omega=0} = -30.5432$ [N/rad] and for the lean torque output this is $T_\phi/e|_{\omega=0} = 267.5570$ [Nm/rad]. When looking at the amplitudes we conclude that the steering torque input is roughly 9 times more efficient than lean torque output. When checking the signs, we notice that the steering torque input acts into the direction of falling and lean torque output acts in the opposite way. At higher frequencies both control outputs gradually increase in magnitude, eventually resulting in unrealistic high feedback from $f > 10$ rad/s. The identification of the rider model is only performed up to 5 Hz, thereby limiting reliable estimation of higher frequency content. So the model should only be evaluated in the range of $0 < \omega < 5 \cdot 2\pi$ [rad/s].

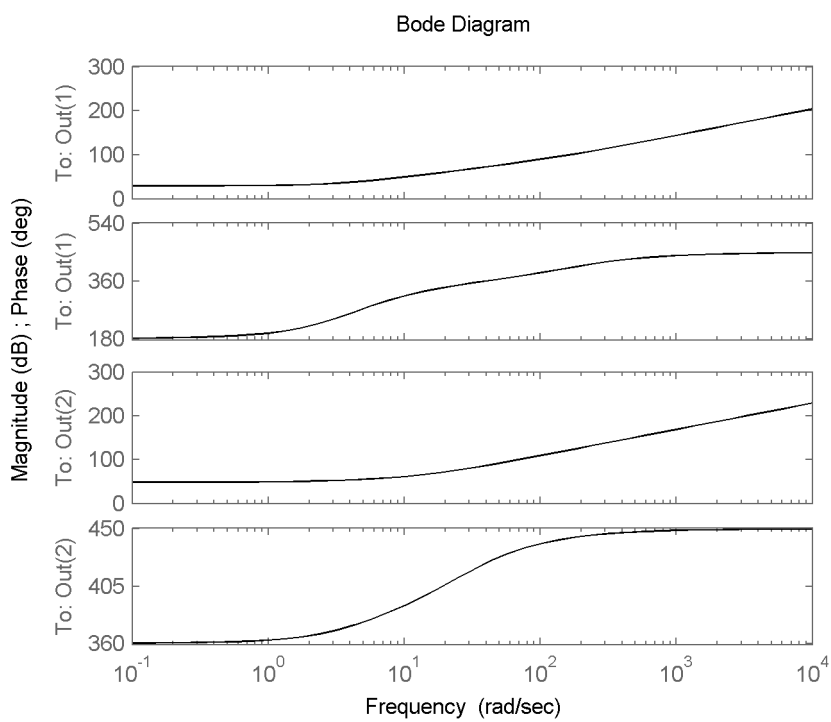


Figure A-4: Bode diagram of the human controller \mathbf{u}/e . The controller is a SIMO controller with 1 input; roll angle error and 2 outputs; (1) steering torque T_δ and (2) lean torque T_θ .

A-1-3 Conclusions

The controller described by Stassen and van Lunteren is implemented in Matlab, with the aim of creating a simulatable bicycle/rider configuration. However during this process we encountered several difficulties. After taking over the results from literature, it turned out that the controller was unstable. This was because the controller did not fulfill the steer into the fall principle, which is probably due to sign errors. After correcting for these sign errors, the controller appeared to be stable when omitting the time delay. However, when including the proposed time delays, simulations showed that the controller becomes unstable. In short; the Stassen and Lunteren controllers have stability issues.

In addition the Stassen and Lunteren controller predescribes steer and rider lean angle as an function of roll angle. By doing so, the controller basically acts as an constraint, reducing the degrees of freedom by one. This position type of control, results in unrealistic high feedback gains at higher frequencies. A more natural kind of controller would be torque driven control, where the human controller outputs torque in stead of position. This torque output control is more commonly found in literature, making it a more logical choice.

Finally, we remark that the rider identification is only performed at one forward velocity, namely $v = 15$ km/h. Therefore the model is of limited use, since it most likely is only valid around this forward velocity, while we are interested in a whole range of velocities.

Concludingly, the Stassen and Lunteren controller will not be used throughout future analysis of the combined bicycle/rider system.

A-2 LQR controller

In this section the LQR (Linear Quadratic Regulator) solution is given for the continuous infinite horizon case. We are interested in controlling the Batavos Stratos with passive rider model, which is described by the following coefficient matrices:

$$\mathbf{M}_0 = \begin{bmatrix} 87.92 & 2.40 & 15.74 \\ 2.40 & 0.72 & 0.53 \\ 15.74 & 0.53 & 4.62 \end{bmatrix},$$

$$\mathbf{K}_0 = \begin{bmatrix} -82.25 & -2.72 & -11.98 \\ -2.72 & -0.99 & 1.52 \\ -11.98 & 1.52 & -12.87 \end{bmatrix},$$

$$\mathbf{K}_2 = \begin{bmatrix} -0.00 & 76.74 & 0.00 \\ -0.00 & 2.63 & 0.00 \\ -0.00 & 11.06 & 0.00 \end{bmatrix},$$

$$\mathbf{C}_1 = \begin{bmatrix} -0.00 & 39.50 & 0.00 \\ -0.49 & 2.41 & 0.00 \\ -0.00 & 6.18 & 0.00 \end{bmatrix}.$$

A-2-1 Implementation

In this section the optimal control problem will be solved, resulting in a set of optimal control gains. We start with defining the system, subject to control. Using the state space definitions of equation 2-9, we derive the following state space system.

$$\dot{\mathbf{x}}(t) = \mathbf{A}\mathbf{x}(t) + \mathbf{B}\mathbf{u}(t) + \mathbf{w}(t), \quad (\text{A-16})$$

with state vector $\mathbf{x} = [\dot{\phi}, \dot{\delta}, \dot{\theta}, \phi, \delta, \theta]^T$, input vector $\mathbf{u} = [T_\delta, T_\theta]^T$, noise vector \mathbf{w} , system dynamics matrix \mathbf{A} and input gain matrix \mathbf{B} . This system is observed by the human controller according to;

$$\mathbf{y}(t) = \mathbf{C}\mathbf{x}(t) + \mathbf{v}_y(t), \quad (\text{A-17})$$

with output vector $\mathbf{y} = [\phi, \delta, \theta]^T$, observation noise vector \mathbf{v} and observer matrix \mathbf{C} . Next, the following objective function to be minimized is defined:

$$J(\mathbf{u}) = \int_0^\infty (\mathbf{x}^T \mathbf{Q} \mathbf{x} + \mathbf{u}^T \mathbf{R} \mathbf{u}) dt, \quad (\text{A-18})$$

with state object \mathbf{Q} represent the state weighting matrix (performance) and \mathbf{R} represents the input weighting matrix (control effort). Since we are interested in controlling the roll angle with minimum control effort, we set these matrices to;

$$\mathbf{Q} = Q_{ij} = \begin{cases} 0 & \text{for } i, j \neq 4 \\ \phi_{\max}^{-2} & \text{for } i, j = 4 \end{cases}, \text{ where } i, j = \{1, 2, \dots, 6\}, \quad (\text{A-19})$$

and

$$\mathbf{R} = \begin{bmatrix} T_{\delta_{\max}}^{-2} & 0 \\ 0 & T_{\theta_{\max}}^{-2} \end{bmatrix}, \quad (\text{A-20})$$

where $\phi_{\max} = 0.1$ rad and $T_{\delta_{\max}} = T_{\theta_{\max}} = 2$ Nm. Next, we are looking for a linear control law of the form:

$$\mathbf{u} = -\mathbf{K}\mathbf{x}, \quad (\text{A-21})$$

where $\mathbf{K} = \mathbf{R}\mathbf{B}^T\mathbf{P}$. Then it can be shown that the objective function is minimized by solving the following algebraic Ricatti equation;

$$\mathbf{A}^T\mathbf{P} + \mathbf{P}\mathbf{A} - \mathbf{P}\mathbf{B}\mathbf{R}^{-1}\mathbf{B}^T\mathbf{P} + \mathbf{Q} = \mathbf{0}. \quad (\text{A-22})$$

This equation is automatically solved by Matlab for $v = \{2..7\}$ m/s. This controller shows stable behavior for all the evaluated velocities. However the control gains show unrealistic high gains, even for the case where the performance/control-effort ratio is reduced. Therefore it is questionable how well this controller describes human rider action. Fortunately we obtained an experimental dataset, on which a number of rider models is tested.

A-2-2 Experimental Results

In addition, this controller was also subjected to experimental validation. The experimental data set, introduced in the next chapter, is used to validate a number of parametric models. Among other rider models, the optimal controller described above is validated using this data set. The entries of the weighting matrices form the parameters of the model, which are optimized by reducing the errors between the measured and simulated output. Without going into too much detail, the optimal control model performed poorly compared with various PID controllers (see next section). Because of this, we will focus on another branch of controllers, which will be presented in the next section.

Appendix B

Input signal design

In this appendix, some commonly used perturbation signals will be discussed. An overview is given at the end of this section.

B-1 White noise

A continuous white noise input $u(t)$ is characterized by the following properties;

$$\mu_u = E\{u(t)\} = 0 \quad (\text{B-1})$$

$$R_{uu} = E\{u(t_1)u(t_2)\} = \frac{1}{2}N\delta(t_1 - t_2) \quad (\text{B-2})$$

Which basically means that the input \mathbf{u} has zero mean (μ_u) and each of the input indices are uncorrelated (R_{uu}) with each other. N represents the number of samples and is infinite in a continuous signal. Notice that the Fourier transformation of a delta Dirac function $\delta(t_1 - t_2)$ gives simply one, the expected autospectral density of the white noise signal thus simply becomes;

$$E\{S_{uu}\} = \frac{1}{2}N \quad (\text{B-3})$$

This is a very nice but strange property. It is nice because the average spectral density stays constant for all frequencies, allowing for infinite bandwidth identification. It also is a strange property, because this signal appears to have infinite power. However in practice we use discrete signals, which results in a finite bandwidth and thus finite power. In addition, we also may choose to apply a low pass filter to limit the frequency content to a certain range of interest. White noise is a random process, which makes it impossible to predict future values. This is a nice property when identifying the human controller, since humans are capable of adapting their control strategy. Using random variables thus eliminates the possibility of using feedforward control. This assumption can be checked afterwards by analyzing the input (y) and output (y) covariance C_{yu} as a function of the time difference τ between the two signals.

$$C_{yu}(\tau) = 0 \quad , \quad \tau < 0 \quad (\text{B-4})$$

This means that the output only depends on previous inputs, i.e. there exists a causal relationship between input (cause) and output (causality).

B-2 Sine sweep

The sine sweep is often used for structural vibration analysis. Here the model subject to identification, is excited using a sine sweep, which most of the time starts at a low frequency and gradually builds up to higher frequencies. A typical definition of the swept sine is given by;

$$u(t) = 2A \sin \left(\left[\pi(f_{\max} - f_{\min}) \frac{t}{T} + 2\pi f_{\min} \right] t \right) \quad (\text{B-5})$$

The autospectral density of this signal is constant between f_{\min} and f_{\max} and gradually decreases at $f > f_{\max}$. Unfortunately the swept sine is a highly predictive signal, allowing a human controller to make use of feed forward control.

B-3 Random phase multisine

Finally we introduce the random phase multisine. Here we start by constructing the signal in the frequency domain and then convert the signal back to the time domain using an inverse Fourier transformation. The random multisine can be defined as follows:

$$|U(\omega)| = \begin{cases} 1 & \text{for } \omega_{\min} \leq \omega \leq \omega_{\max}, \\ 0 & \text{for } \omega > \omega_{\max} \end{cases} \quad (\text{B-6})$$

$$\angle U(\omega) = \begin{cases} \theta & \text{for } \omega_{\min} \leq \omega \leq \omega_{\max}, \\ 0 & \text{for } \omega > \omega_{\max} \end{cases} \quad (\text{B-7})$$

Where θ is randomly distributed for each frequency ω according to a uniform probability density function. Setting up signals in the frequency domain allows for easy autospectral density shaping. This is a nice feature, because we are generally interested in the frequency content of the input signal. Using this method allows the user to select one or multiple desired frequency bands. Unfortunately this kind of signal modelling in the frequency domain may result in unwanted peaks in the time domain.

B-4 Crested multisine

To reduce peak amplitudes while maintaining the desired average power density, the phase can be optimized to fulfill these properties. The crest factor C forms a useful definition when optimizing the signal;

$$C = \frac{u_{\max}}{u_{\text{rms}}} = \frac{\max(\mathbf{u})}{\sqrt{N^{-1} \mathbf{u}^T \mathbf{u}}}, \quad (\text{B-8})$$

	White noise	Swept sine	Multisine	Crested
Mean (μ_u):	0	0	0	0
Correlation (R_{uu}):	1	1	1	1
Spectral density (S_{uu}):	1.0145	2.4912	2.5000	2.5000
Crest factor (C):	3.6129	1.4026	3.2857	2.3943
Predictable:	no	yes	no	no

Table B-1: Comparison of various input signals. Notice that the spectral density is defined as the average spectral density over the desired frequency band.

where; N represents the number of samples and \mathbf{u} represents the input signal vector. The objective function will be to reduce the crest factor, the parameters subject to optimization will be the phase indices. It is beyond the scope of this report to explain the optimization algorithm in detail. What is important is that the resulting signal indeed has a significant lower crest factor.

B-5 Comparison

A short overview of the various input signals is given in table B-1.

B-6 Results

The multisine offers the best results, but is predicatable, therefore the crested random phase multisine is advised when identifying the human controller.

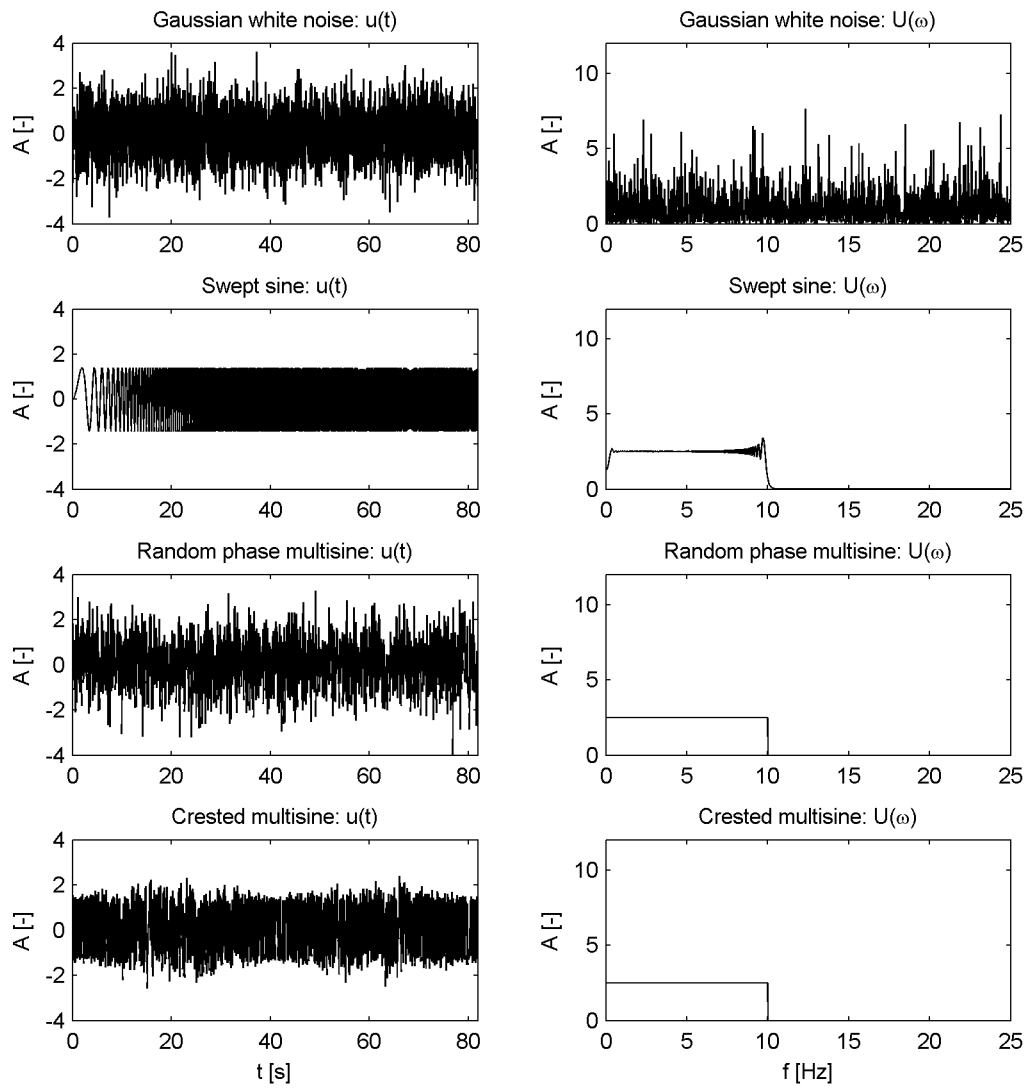


Figure B-1: 4 different input signals: Gaussian white noise, swept sine, random phase multisine, crested random phase multisine

Appendix C

Analysis of a Double Inverted Pendulum on a Cart

In this chapter the dynamic behavior of the inverted double pendulum on a cart will be investigated. This system shows a lot of similarities with the bicycle, but it is easier to understand since it simplifies the problem to a 2 dimensional case. The following analogies are made:

- The base pendulum corresponds to the bicycle frame.
- The top pendulum corresponds to the rider on top of the bicycle.
- The lateral movement of the system corresponds to lateral movement of the bicycle when making turns.

The system and corresponding definitions are shown in figure C-1. The locations for the center of masses are set up as function of the generalized coordinates $q = [u, \phi, \theta]^T$ and yield:

$$\begin{aligned}x_1 &= \frac{1}{2}l_1 \sin \phi + u , \\y_1 &= \frac{1}{2}l_1 \cos \phi , \\x_2 &= \frac{1}{2}l_1 \sin \theta + l_1 \sin \phi + u , \\y_2 &= \frac{1}{2}l_1 \cos \theta + l_1 \cos \phi .\end{aligned}$$

These coordinates and their derivatives are used to set up the systems kinetic energy T and potential energy V :

$$T = \frac{1}{2}m_1(\dot{x}_1^2 + \dot{y}_1^2) + \frac{1}{2}m_2(\dot{x}_2^2 + \dot{y}_2^2) + \frac{1}{2}J_1\dot{\phi}^2 + \frac{1}{2}J_2(\dot{\phi} + \dot{\theta})^2 , \quad (\text{C-1})$$

$$V = m_1gy_1 + m_2gy_2 , \quad (\text{C-2})$$

with $J_i = \frac{1}{12}m_i l_i^2$. The energies are inserted into the Lagrange machinery and linearized around $\phi = \theta = 0$, resulting in the following mass, damping and stiffness matrices;

$$\mathbf{M} = \begin{bmatrix} m_1 + m_2 & \frac{1}{2}l_1 m_1 + l_1 m_2 + \frac{1}{2}l_2 m_2 & \frac{1}{2}l_2 m_2 \\ \frac{1}{2}l_1 m_1 + l_1 m_2 + \frac{1}{2}l_2 m_2 & \frac{1}{3}l_1^2 m_1 + l_1^2 m_2 + \frac{1}{3}l_2^2 m_2 + l_1 l_2 m_2 & \frac{1}{6}l_2 m_2 (3l_1 + 2l_2) \\ \frac{1}{2}l_2 m_2 & \frac{1}{6}l_2 m_2 (3l_1 + 2l_2) & \frac{1}{3}l_2^2 m_2 \end{bmatrix},$$

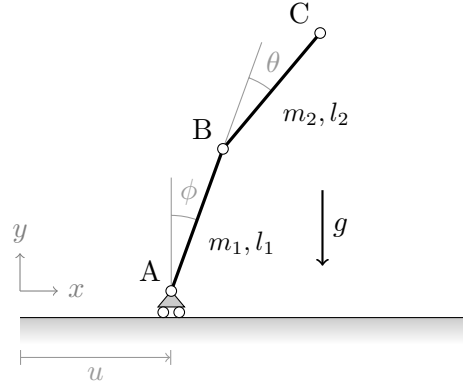


Figure C-1: Schematic drawing of the inverted double pendulum on a cart, with lateral displacement u , base pendulum angle ϕ , relative angle θ . The mass and length of the base pendulum is indicated by l_1 and m_1 and for the upper pendulum by l_2 and m_2 . The gravitational acceleration is indicated by g .

$$\mathbf{C} = \begin{bmatrix} 0 & 0 & 0 \\ 0 & 0 & 0 \\ 0 & 0 & 0 \end{bmatrix}, \quad (\text{C-3})$$

$$\mathbf{K} = \begin{bmatrix} 0 & 0 & 0 \\ 0 & -\frac{1}{2}l_1gm_1 - \frac{1}{2}gm_2(2l_1 + l_2) & -\frac{1}{2}l_2gm_2 \\ 0 & -\frac{1}{2}l_2gm_2 & -\frac{1}{2}l_2gm_2 \end{bmatrix}, \quad (\text{C-4})$$

Which results in the following set of linear equations:

$$\mathbf{M}\ddot{\mathbf{q}} + \mathbf{C}\dot{\mathbf{q}} + \mathbf{K}\mathbf{q} = \mathbf{f}, \quad (\text{C-5})$$

where $\mathbf{f} = [T_u, T_\phi, T_\theta]$ represent the forcing vector, which contains the generalized forces.

Controlling a bicycle shows a lot of similarity with controlling an double inverted pendulum on a cart. Lateral acceleration into the direction of falling results in a counteracting torque and the rider lean action can simply modelled as an extra pendulum on top. Therefore by understanding the inverted double pendulum problem, we can learn more about controlling the bicycle. First the accelerating in the fall will be analyzed and secondly the lean action for the double inverted pendulum.

C-1 Accelerating in the fall

By accelerating into the direction of fall, the ground support can be moved back under the center of mass. For simplicity we assume that the rider is rigidly attached to the bicycle frame, resulting in the following constraint: $\theta = 0$. This constraint can be projected onto the equations of motion, making it effectively an single inverted pendulum on a cart. From the bicycle equations, we know that the lateral acceleration can be controlled by applying proper steering. T_u . Next we reduce the equations by introducing:

$$\tilde{\mathbf{q}} = \mathbf{T}\mathbf{q}, \quad (\text{C-6})$$

where $\tilde{\mathbf{q}} = [u, \phi]$ and \mathbf{T} is the reduction matrix, such that:

$$\begin{aligned}\tilde{\mathbf{M}} &= \mathbf{T}^T \mathbf{M} \mathbf{T} , \\ \tilde{\mathbf{C}} &= \mathbf{T}^T \mathbf{C} \mathbf{T} , \\ \tilde{\mathbf{K}} &= \mathbf{T}^T \mathbf{K} \mathbf{T} ,\end{aligned}\tag{C-7}$$

Here, we allow the lateral acceleration of the cart be controlled by applying lateral torque control, so $\tilde{\mathbf{f}} = [T_u, 0]^T$. The controllability is tested using the Matlab `ctrb` function, which stated the system is controllable. To analyze what control means will be necessary, an optimal controller is implemented. Here the roll angle is defined as the main control objective. The resulting gains, showed that the system is mainly controlled by applying positive roll angle and rate feedback. In other words; a fall to the left, requires the cart to accelerate in the same direction.

For the case of the bicycle this lateral acceleration (denoted by \ddot{y}') is achieved by proper steering action.

$$\ddot{y}_p' = \frac{v^2}{w} \delta \cos \lambda + \frac{vc}{w} \dot{\delta} \cos \lambda.\tag{C-8}$$

So acceleration to the left, requires steering in the same direction as the fall. This is known as; 'steer into the fall'.

C-2 Lean action analysis

To analyze the roll and lean angle observed by Stassen and van Lunteren, a simple double pendulum model simulated. Next we will analyze how the lean action could be used for controlling the upright position of the double pendulum. First we again reduce the original double pendulum on a cart equations to exclude the lateral movement:

$$\tilde{\mathbf{q}} = \mathbf{T} \mathbf{q} ,\tag{C-9}$$

where $\tilde{\mathbf{q}} = [\phi, \theta]$ and \mathbf{T} is the reduction matrix, such that:

$$\begin{aligned}\tilde{\mathbf{M}} &= \mathbf{T}^T \mathbf{M} \mathbf{T} , \\ \tilde{\mathbf{C}} &= \mathbf{T}^T \mathbf{C} \mathbf{T} , \\ \tilde{\mathbf{K}} &= \mathbf{T}^T \mathbf{K} \mathbf{T} ,\end{aligned}\tag{C-10}$$

Next we only allow for a relative steer torque between the two pendula, so the force vector reduces to: $\tilde{\mathbf{f}} = [0, T_\theta]$, which corresponds to pure leaning action. Next we introduce an LQR controller for controlling the upright position of the pendulum. The following weighting matrices are chosen:

$$\mathbf{Q} = \begin{bmatrix} 0 & 0 & 0 & 0 \\ 0 & 0 & 0 & 0 \\ 0 & 0 & 1 & 0 \\ 0 & 0 & 0 & 0 \end{bmatrix}, \mathbf{R} = [1]$$

Figure C-2: Top; absolute angle ϕ of the base pendulum and relative angle θ of the upper pendulum versus time t . Bottom; applied relative torque T_θ versus time t . The top graph is showing that θ is roughly positively proportional to ϕ . The lower graph shows the applied relative roll torque T_θ . The system is disturbed by applying a randomly distributed roll torque T_ϕ to the bottom pendulum.

Resulting in the following state feedback controller:

$$\mathbf{u} = -\mathbf{K}\mathbf{x}, \quad (\text{C-11})$$

with controller gains:

$$\mathbf{K} = \begin{bmatrix} -723.16 & -328.71 & -1680.4 & -720.17 \end{bmatrix}, \quad (\text{C-12})$$

Which implies positive roll and lean angle and rate feedback. A white noise torque disturbance is applied onto the lower pendulum, to analyze the coupling between the upper and lower pendulum angles. The results are shown in figure C-2. A proportional negative coupling between ϕ and θ is observed.

C-3 Conclusions

From the double pendulum analysis, the following observations are made:

- A single inverted pendulum on a cart can be stabilized by accelerating into the direction of fall. For the case of the bicycle, the lateral acceleration can be accomplished by steering into the same direction. This stabilization principle is known as 'steer into the fall'.
- The double inverted pendulum (not on a cart) can be stabilized by applying a relative torque between the two pendula. This corresponds to balancing a bike at zero velocity, using upper body movement.

Appendix D

Parameter covariance

This section describes how the parameter uncertainty can be calculated using Matlab output.

D-1 Defintions

Suppose we have a measured signal $y(t)$ and modelled signal $\hat{y}(t, \theta)$, which is a function of the parameter vector θ . The error becomes

$$e(t, \theta) = y(t) - \hat{y}(t, \theta) , \quad (\text{D-1})$$

which is used to define the following commonly used sum of the error squared error criterium:

$$V(\theta) = \frac{1}{2} \sum_{t=1}^n [e(t, \theta)]^2 . \quad (\text{D-2})$$

For which we find the following parameter vector that minimizes the criterium according to:

$$\hat{\theta}_n = \arg \min_{\theta} V(\theta) \quad (\text{D-3})$$

D-2 Covariance definition

Next we introduce the parameter covariance function. According to Ljung 1999, the covariance function is given by:

$$P_{\theta} = \hat{\lambda}_n \left[\frac{1}{n} \sum_{t=1}^n \psi(t, \hat{\theta}_n) \psi^T(t, \hat{\theta}_n) \right]^{-1} , \quad (\text{D-4})$$

where

$$\hat{\lambda}_n = \frac{1}{n} \sum_{t=1}^n [e(t, \hat{\theta}_n)]^2 , \quad (\text{D-5})$$

$$\psi(t, \hat{\theta}_n) = -\frac{d}{d\theta} e(t, \hat{\theta}_n) = \frac{d}{d\theta} \hat{y}(t | \hat{\theta}_n) \quad (\text{D-6})$$

D-3 Matlab output defintions

The Matlab algorithms may either output the gradient (`grad`) and Hessian (`hessian`) of the criterium with respect to the parameter vector, which is the case for the `fmincon` function. These outputs are defined as follows:

$$\text{grad} = \left. \frac{dV(\theta)}{d\theta} \right|_{\theta=\hat{\theta}_n} = 0 \quad (\text{D-7})$$

$$\text{hessian} = \left. \frac{d^2V(\theta)}{d\theta^2} \right|_{\theta=\hat{\theta}_n} \quad (\text{D-8})$$

Other algorithms like the `lsqnonlin` may output the Jacobian (`jacobian`) of the error vector with respect to the parameters:

$$\text{jacobian} = \left. \frac{de(t, \theta)}{d\theta} \right|_{\theta=\hat{\theta}_n} \quad (\text{D-9})$$

$$(\text{D-10})$$

D-4 Expressing covariance in terms of Matlab output

Finally we analyze how to use the matlab output in order to derive the parameter covariance. We basically want to derive $\hat{\lambda}_n$ and $\psi(t, \hat{\theta}_n)$. Here $\hat{\lambda}_n$ can be directly obtained by simply calculate the error vector $e(t, \hat{\theta}_n)$ according to equation D-1 and sum the squares. The latter, $\psi(t, \hat{\theta}_n)$ is more tricky and also depends on the kind of optimization algorithm you use.

We start of by linearizing our model \hat{y} around the optimum parameter configuration $\hat{\theta}_n$. Lets assume our model is continous and differentiable around the found optimum, so that the following linearization holds for small deviations of θ around $\hat{\theta}_n$.

$$\hat{y}(t, \theta) \approx \hat{y}(t, \hat{\theta}_n) + \frac{d\hat{y}(t, \hat{\theta}_n)}{d\theta}(\theta - \hat{\theta}_n) \quad , \text{ for } \theta \rightarrow \hat{\theta}_n . \quad (\text{D-11})$$

This result can be used to analyze the meaning of the `grad`, `hessian` and `jacobian` output, since they are all computed numerically near $\hat{\theta}_n$.

D-4-1 Hessian method

Lets start of by writing out the criterium function $V(\theta)$, which is used for the **grad** and **hessian** output.

$$\begin{aligned}
 V(\theta) &= \frac{1}{2} \sum_{t=1}^n [e(t, \theta)]^2 , \\
 &= \frac{1}{2} \sum_{t=1}^n \left[y(t) - \hat{y}(t, \hat{\theta}_n) - \frac{d\hat{y}(t, \hat{\theta}_n)}{d\theta} (\theta - \hat{\theta}_n) \right]^2 , \\
 &= \frac{1}{2} \sum_{t=1}^n \left[[y(t)]^2 + [\hat{y}(t, \hat{\theta}_n)]^2 + \left[\frac{d\hat{y}(t, \hat{\theta}_n)}{d\theta} \right]^2 (\theta - \hat{\theta}_n)^2 \right] \dots \\
 &\quad \dots + \sum_{t=1}^n \left[-y(t)\hat{y}(t, \hat{\theta}_n) - y(t) \frac{d\hat{y}(t, \hat{\theta}_n)}{d\theta} (\theta - \hat{\theta}_n) + \hat{y}(t, \hat{\theta}_n) \frac{d\hat{y}(t, \hat{\theta}_n)}{d\theta} (\theta - \hat{\theta}_n) \right] .
 \end{aligned}$$

Next we take the first derivative with respect to the parameters, which yields:

$$\frac{dV(\theta)}{d\theta} = \sum_{t=1}^n \left[\left[\frac{d\hat{y}(t, \hat{\theta}_n)}{d\theta} \right]^2 (\theta - \hat{\theta}_n) \right] \dots \quad (\text{D-12})$$

$$\dots + \sum_{t=1}^n \left[-y(t) \frac{d\hat{y}(t, \hat{\theta}_n)}{d\theta} + \hat{y}(t, \hat{\theta}_n) \frac{d\hat{y}(t, \hat{\theta}_n)}{d\theta} \right] , \quad (\text{D-13})$$

which corresponds to the **grad** function and is zero at the optimum. The second derivative corresponding to the **hessian** yields:

$$\frac{d^2V(\theta)}{d\theta^2} = \sum_{t=1}^n \left[\frac{d\hat{y}(t, \hat{\theta}_n)}{d\theta} \right]^2 . \quad (\text{D-14})$$

Now we are getting somewhere, since $dy(t, \hat{\theta}_n)/d\theta = \psi(t, \hat{\theta}_n)$. So substituting $\theta = \hat{\theta}_n$, which corresponds to the Hessian found at the optimum we find:

$$\text{hessian} = \left. \frac{d^2V(\theta)}{d\theta^2} \right|_{\theta=\hat{\theta}_n} , \quad (\text{D-15})$$

$$= \sum_{t=1}^n [\psi(t, \hat{\theta}_n)]^2 , \quad (\text{D-16})$$

$$= \sum_{t=1}^n \psi(t, \hat{\theta}_n) \psi^T(t, \hat{\theta}_n) . \quad (\text{D-17})$$

So the parameter covariance in terms of the Hessian becomes:

$$P_\theta = \hat{\lambda}_n \left[\frac{1}{n} \text{hessian} \right]^{-1} . \quad (\text{D-18})$$

D-4-2 Jacobian method

Starting of with equations 2-3 and D-10 we derive:

$$\psi(t, \hat{\theta}_n) = -\text{jacobian} \quad (\text{D-19})$$

So the parameter covariance in terms of the Jacobian becomes:

$$P_\theta = \hat{\lambda}_n \left[\frac{1}{n} \text{jacobian} \cdot \text{jacobian}^T \right]^{-1} . \quad (\text{D-20})$$

Appendix E

The Human Controller

In this appendix some of the more general properties of the human controller will be discussed. The human can act as an closed loop controller; perceiving information through the sensory system, processing the information through in the central nervous system (CNS) and interact with the environment through the muscular system. This combined system is known as the neuromuscular system. Different levels of human control are identified; compensatory control, pursuit and precognitive control. The properties of the human controller are described according to Herman van der Kooij (2008), van der Kooij et al. (1999), van der Kooij et al. (2001) and McRuer (1980).

E-1 Neuromuscular system

The neuromuscular system represents the active part of the human controller contribution to the combined man machine system. Figure E-2 gives an overview of the neuromuscular control loop. The objective state is compared with the current state observed through the sensory system. This information is then processed in the central nervous system, which outputs neural stimuli destined to the muscular system. The system contains time delays which are represented by τ . Also the activation dynamics of the muscular system is not instantanius but show muscular lag. Finally, the admittance of the combined system has its effect on the eventual movement caused by muscular contraction.

E-1-1 Sensory system

The sensory system provides information about the external world allowing for feedback control. Without sensory feedback the human controller could only act as an open loop feed forward controller, allowing errors to accumulate. The human body has many sensory systems; visual, vestibular, proprioceptive, smell, taste, etc. The analysis of these systems will be limited only to the systems involved with human movement control.

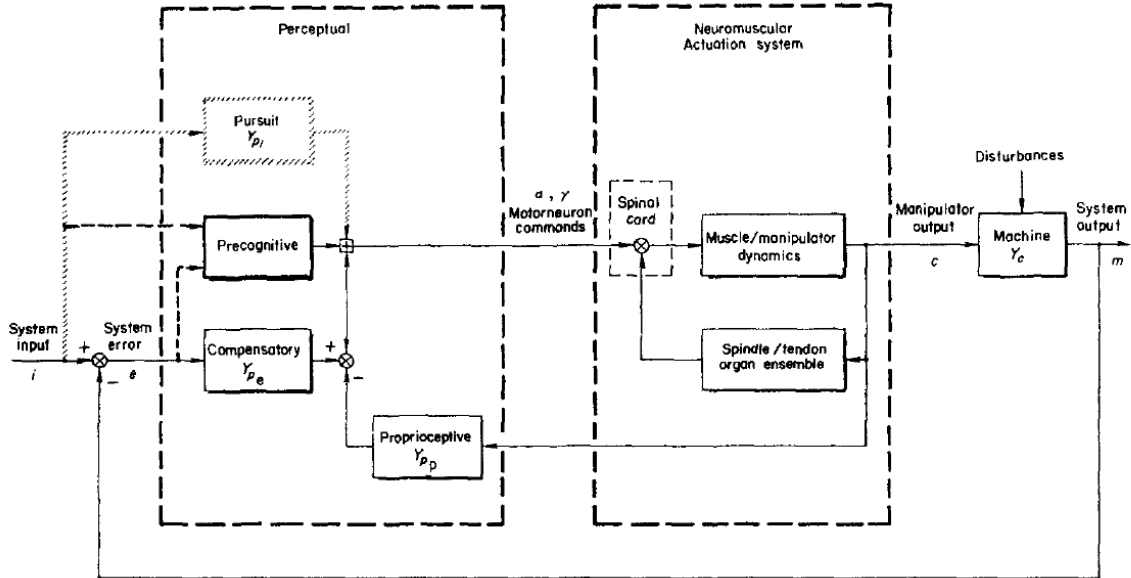


Figure E-1: Human control during man machine interaction. The perceptual block converts system input i , system output m and proprioceptive feedback y_{pp} into motor neuron commands. Three levels of control are identified in the perceptual block; compensatory control, pursuit, and precognitive control. The neuromuscular actuation system converts the motor commands to manipulator output c , allowing for interaction with the system subject to control y_c . The human observer dynamics are omitted in this block scheme. Taken over from McRuer (1980).

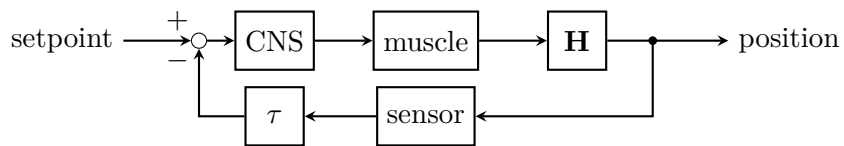


Figure E-2: Simplified block scheme of the neuromuscular system. The CNS acts as the actual controller of the human body. It outputs motor commands which are translated into actual motor output through the muscle block. The system dynamics are contained in H . The output position of the system is then observed by the human controller through the observer block. The transport delays are all represented by the τ block. The error which is defined as the difference between the position and the set-point is finally fed back to the CNS to complete the loop. Based on Herman van der Kooij (2008).

Visual system

The visual systems allows for measuring light intensity and color coming from the environment. This information is sensed by the eyes, which form the sensors of the visual system. This information is processed by the visual cortex of the brain, resulting in a continuous 'picture' in time or 'movie' of the external world. Using sophisticated image processing techniques the brain is then capable of deriving relevant information from this picture. In the case of bicycling the visual system could give information about the horizon, forward velocity of the bicycle, future curvature of the road, etc.

Vestibular system

The vestibular system basically acts as the accelerometer of the human body. The vestibular organs are located in the head behind the ear. They are also known as the 'organ of equilibrium' because they can measure if the human is in balance. In practice this is achieved by measuring the angle relatively to the vertical axis by making use of the acceleration caused by the gravitational field g . In addition they are also well suited for measuring changes in the velocity, i.e. if a person is falling the velocity is increasing, which is then sensed by the vestibular organ. Among other parts, the vestibular organ consists of three semicircular shaped canals and the otoliths. The canals are sensitive to rotational (yaw, pitch, roll) acceleration, whereas the otoliths are sensitive to transversal (xyz) acceleration.

Proprioceptive system

The proprioceptive system is concerned with self sensing of the human body. For human movement control, the two most important sensors are the Golgi tendon organs (GTO) and muscle spindles. The Golgi tendon organs are located in the muscle tendons and are able to measure tension. The muscle spindles are located in the muscle fibers and are capable of measuring both muscle length and stretch velocity. The information of the proprioceptive system is transported using the afferent sensory nerves. This transportation of information leads to time delays, since the transmission speed is limited. Table E-1 shows some of the properties of the proprioceptive system.

Nerve type	Diameter (μm)	Transmission speed (m/s)	Type of sensor	Stimulus
Ia	12-20	70-100	muscle spindle	length & velocity
Ib	12-20	70-100	GTO	force
II	6-12	35-70	muscle spindle	length

Table E-1: Some properties of the proprioceptive system (taken over from HMC reader, WB2407)

Sensor dynamics

The sensor dynamics can be modeled according to the appendix found in van der Kooij et al. (1999), which is based on Borah et al. (1988).

Muscle spindle model:	$\frac{\text{afferent fire rate}}{\text{position}}$	=	$\frac{5(s+4)}{s+20}$
Semicircular model:	$\frac{\text{afferent fire rate}}{\text{angular acceleration}}$	=	$\frac{0.574s(s+100)}{(s+0.1)(s+0.033)}$
Otolith model:	$\frac{\text{afferent fire rate}}{\text{specific force}}$	=	$\frac{90(s+0.1)}{s+0.2}$
Vision mode:	$\frac{\text{afferent fire rate}}{\text{distance head-visual scene}}$	=	1
Tactile model:	$\frac{\text{afferent fire rate}}{\text{force}}$	=	$\frac{s+0.01}{s+0.1}$

The total neural time delay τ is estimated to be 100 ms.

Human observer models

Human observer models describe how sensory input can be integrated to form an optimized observation of the human and the environment. A popular branch of these human observer models is given by an application of the Kalman filter according to (Kleinman et al., 1970). This filter combines noisy measurements (sensory information) and knowledge of the system (human body dynamics) into an optimal state estimate of the system. It is beyond the scope of this report to treat these models in detail. However, a detailed application of the Kalman filter for human stance control can be found in van der Kooij et al. (1999). In addition, a similar model which incorporates sensor adaptability is given by van der Kooij et al. (2001).

E-1-2 Central nervous system

The central nervous system (CNS) processes desired position and sensory feedback and generates motor commands (α -activation) to the muscles. The CNS therefore forms the heart of human movement control. In a sense; the CNS is the human controller. The workings of the CNS are highly complex and little is known about the way the CNS stores and processes information. The CNS consists of the brain and spinal cord, which are connected by nerves to the sensory and motory system.

E-1-3 Muscular system

The muscular system is the actuator of the human body. It uses muscular force to generate joint torques, which allows the human body to move and interact mechanically with the environment. The muscles are the means of actuation, they transform neural signals into actual force. There are three kinds of muscles, but we will only focus on skeletal muscles, which are interesting concerning human motion control. These muscles are activated by neural stimuli and the amount of contraction is determined by the rate of firing stimuli, e.g. the higher the rate the stronger the contraction.

Muscle dynamics

Muscle force is not able to act instantaneous similar to a bang bang controller, but needs some activation time to build up in strength. A simple model of these activation dynamics, also known as muscular lag, is given by;

$$q(s) = \frac{1}{1 + \tau_{ac}s} e(s), \quad (\text{E-1})$$

where $q(s)$ represents the muscle activation, $e(s)$ the muscle excitation and τ_{ac} the activation time constant. Equation E-1 acts as an low pas filter, which filters out fast transitions, e.g. it smoothens changes in muscular torques.

E-2 Control methods

According to McRuer (1980), the human controller can be separated into three subsystems; compensatory, pursuit and precognitive control, which will be explained in more detail in this section. An overview of the complete control system is giving in figure E-1.

E-2-1 Compensatory control

The compensatory control system is there to minimize errors caused by random commands and disturbances. It is a continues closed loop controller acting only on the observed errors between the desired state and actual state. The compensatory system is often described as a they inner loop low level controller. The compensatory system forms the base for higher level controllers such as the pursuit and precognitive control system. The compensatory control system can be identified by using random perturbations applied at either the objective function or as an external disturbance.

E-2-2 Pursuit

The pursuit control system is being used when the human controller has access to future inputs and disturbances. For example, in the case of curved path following; the rider might have access to future curvature through the visual system. This information is used by the pursuit system to generate a optimized desired control sequence. This in combination with the compensatory system gives a superior result compared with only using the compensatory control.

E-2-3 Precognitive control

Precognitive control is the highest level of control. The rider executes a learned maneuver in an open-loop way. In order to achieve this, the rider needs complete knowledge of the system and perceptual information. This information is then combined to generate a series of optimal neuromuscular pulses, resulting in a perfectly desired machine output. Learning these movements is similar as training a neural network. In practice uncertainty and noise are always presented, so compensatory control is still required.

E-3 Summary

The human controller is capable of sensing (sensory system), processing (CNS) and actuating (muscular system). Among other information, the sensory system is capable of observing; image (eyes), accelerations (vestibular system), muscle length and velocity (muscle spindles) and muscular force (Golgi tendon organs). The CNS consists of the brain and spinal cord and is in itself the human controller. The muscular system forms the actuator of the human body. The human controller has complex sensor dynamics and is limited by neuromuscular lag and transport delays.

Three different human control subsystems are identified; compensatory, pursuit and precognitive control. The compensatory system tends to minimize the errors between the desired state and actual state. The pursuit subsystem uses feed forward techniques to generate optimized desired state configuration. The precognitive system forms the highest level of control and can be seen as a trained neural network.

Appendix F

Bicycle Simulator

To gain more insight in human rider control, a computer bicycle simulator is created. The user controls the velocity and steering torque using a controller and receives visual feedback of the 3D bicycle visualization. In addition, visual displays for the roll angle and rate, applied torque and forward velocity are also added. The bicycle simulator is created using Matlab and Simulink. Playing around with the simulator shows intermittent control and the necessity of roll rate feedback when it comes to controlling the unstable weave mode. The unstable capsize mode can simply be controlled using roll angle feedback only. It is possible to stabilize the bicycle from velocities of roughly 3.5 m/s and higher, whereas stabilization in real world bicycling is possible a way lower velocities. The simulator is somewhat limited since it only gives visual feedback, important proprioceptive feedback is omitted.

F-1 Setup

The following hardware components are used for the simulator: Laptop (Compaq HP 8510w: 2500ghz, 2GD DDR2 RAM, Quadro FX570M) and gamepad (Logitech Rumble Gamepad F510). The laptop is is running Matlab R2009b. The gamepad is simply connected to the laptop using the USB port. The gamepad and the corresponding button functionality are shown in figure F-1. The analog left paddle and triggers are uses to control the steering torque and forward velocity. The simulation can be stopped using the back button.

F-2 Software

The simulator is written in Matlab and Simulink. The actual ODE solving of the equations of motion is done in Simulink. A 3D model of the bicycle and the environment are created using 3D Studio Max. The Simulink model is then compiled to C-code which allows for faster real time running. Finally a Matlab GUI is written to provide additional feedback components.



Figure F-1: Button functionality of the gamepad

F-2-1 Setting up the Simulink model

First the data acquisition for the game pad is set up. This is achieved fairly simple using the 'analog input' from the Simulink real time toolbox. The input signals are then rescaled and applied to the bicycle equations as torque (left paddle) and change in forward velocity (triggers). The back button is used to stop the simulation. The benchmark bicycle equations (both linear and non-linear) are inserted in ODE form, by expressing the state derivatives as a function of the state and input ($\dot{\mathbf{x}} = \mathbf{f}(\mathbf{x}, \mathbf{u}, t)$). A fixed step (0.02s, 50Hz) Dormand-Prince solver is used.

F-2-2 3D bicycle visualization

A 3D model of the bicycle and environment is set up using 3D Studio Max. This model and environment is then exported as a VRML97 world, which is supported by the Simulink 3D animation toolbox. The coordinates of the bicycle are then coupled to the state and global orientation variables of the bicycle, which are computed using the Simulink solver.

F-2-3 Compilation to real time C-code

The Simulink real time toolbox is used for creating fast running real time simulations. In order to achieve this the real time windows target (RTW) is applied. The RTW does a number of things, required to speed up the simulations and making it real time. First, the Simulink model is compiled to faster running C-code. Secondly, the RTW reserves a small

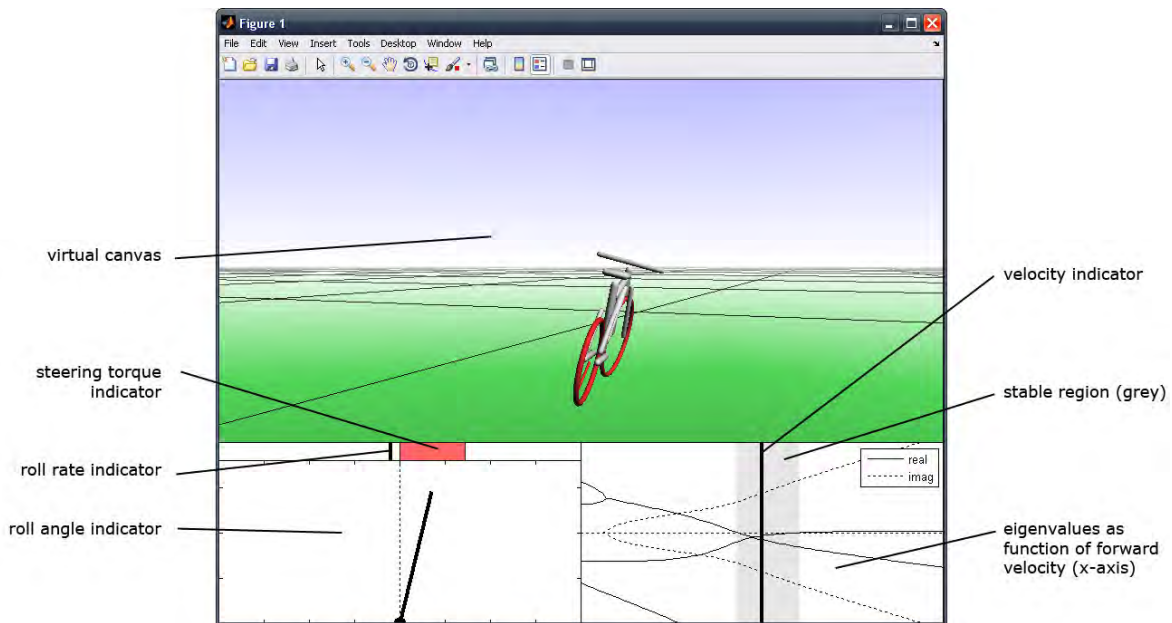


Figure F-2: Graphical User Interface of the bicycle simulator.

piece of memory with top (0 level) priority on the windows kernel allowing for super fast processing. Thirdly, the RTW couples the simulation directly to the PC clock resulting in real time simulations.

F-2-4 Matlab GUI

Finally a graphical user interface (GUI) is designed to incorporate additional feedback (figure F-2). The 3D visualisation is added to the GUI as a virtual canvas. The steering torque, roll angle, roll rate and forward velocity are plotted using regular plot commands, which are updated during each simulation step.

F-3 Results

The following observations are made from playing around with the linear bicycle model simulator.

- Control seems to be done intermittently.
- The dynamic behavior of the bicycle changes as function of the forward velocity.
- The unstable capsizing mode is easy to control using roll angle feedback.
- The unstable weave mode is way harder to control and requires well timed pulses of steering torque.
- Adding visual roll rate feedback makes control of the unstable weave mode possible.

- At forward velocities way below the weave speed, the system becomes uncontrollable.
- In general; controlling the simulated bicycle is way harder than real world bicycling.
- It is hard to control the steering torque precisely using thumb control of the game pad.

F-4 Discussion

The bicycle simulator gives some interesting yet limited results. For example, the observed intermittent control is also described in literature by Doyle. In addition, the unstable capsize and weave mode can be controlled by roll angle and rate feedback respectively, which is similar to intuitive controller. However, the bicycle simulator is also limited, making it way harder to control than a real bicycle. In particular the simulator misses the feel like real bike; the proprioceptive feedback and vestibular feedback paths are missing and the thumb control input feels less precise than a real bicycle steer. These limitations especially become apparent when one tries to control the bicycle at velocities way below the weave speed, which is virtually impossible.

F-5 Conclusion

The bicycle simulator provides a playful way of exploring the equations of motion of the bicycle. It also is interesting yet limited when it comes to analyzing the human controller. The simulator only gives visual feedback, whereas vestibular and proprioceptive feedback are present in real world bicycling. For future bicycle simulators it is recommended to include these feedback paths making it a more realistic experience.

Bibliography

- Borah, J., Young, L., and Curry, R. (1988). Optimal estimator model for human spatial orientation. *Annals of the New York Academy of Sciences*, 545(1):51–73.
- Carvallo, E. (1899). *Théorie du mouvement du monocycle et de la bicyclette*. Gauthier-Villars, Paris, France. (Submitted in 1897 for the Prix Fourneyron, awarded shared second place in 1898.).
- de Vlugt, E., Schouten, A., and van der Helm, F. (2003). Closed-loop multivariable system identification for the characterization of the dynamic arm compliance using continuous force disturbances: a model study. *Journal of neuroscience methods*, 122(2):123–140.
- Doyle, A. (1988). The essential human contribution to bicycle riding. In Patrick, J. and Duncan, K. D., editors, *Training, Human Decision Making Control*. Elsevier Science Publishers BV.
- Happee, R., De Vlugt, E., and Schouten, A. (2009). Posture maintenance of the human upper extremity; identification of intrinsic and reflex based contributions. *SAE International Journal of Passenger Cars-Mechanical Systems*, 1(1):1125.
- Herman van der Kooij, Bart Koopman, F. C. v. d. H. (2008). Human movement control reader.
- Kleinman, D. L., Baron, S., and Levison, W. H. (1970). An optimal control model of human response part i: Theory and validation. *Automatica*, 6(3):357 – 369.
- Kooijman, J. D. G., Meijaard, J. P., Papadopoulos, J. M., Ruina, A., and Schwab, A. L. (2011). A bicycle can be self-stable without gyroscopic or caster effects. *Science*, 332(6027):339–342.
- Kooijman, J. D. G. and Schwab, A. L. (2008). Some observations on human control of a bicycle. In Zobory, I., editor, *11th mini Conference on Vehicle System Dynamics, Identification and Anomalies (VSDIA2008), Budapest, Hungary*, page 8. Budapest University of Technology and Economics.

- Kooijman, J. D. G., Schwab, A. L., and Meijaard, J. P. (2008). Experimental validation of a model of an uncontrolled bicycle. *Multibody System Dynamics*, 19:115–132.
- Ljung, L. (1987). *System identification: theory for the user*, volume 11. Prentice-Hall Englewood Cliffs, NJ.
- McRuer, D. (1980). Human dynamics in man-machine systems. *Automatica*, 16(3):237–253.
- McRuer, D. and Jex, H. (1967). A review of quasi-linear pilot models. *Human Factors in Electronics, IEEE Transactions on*, HFE-8(3):231–249.
- Meijaard, J., Papadopoulos, J. M., Ruina, A., and Schwab, A. (2007). Linearized dynamics equations for the balance and steer of a bicycle: a benchmark and review. *Proceedings of the Royal Society A*, 463:1955–1982.
- Moore, J. K., Hubbard, M., Schwab, A. L., and Kooijman, J. D. G. (2010). Accurate measurement of bicycle parameters. In *Proceedings, Bicycle and Motorcycle Dynamics 2010 Symposium on the Dynamics and Control of Single Track Vehicles, 20–22 October 2010, Delft, The Netherlands*.
- Mugge, W., Abbink, D., and Van der Helm, F. (2007). Reduced power method: how to evoke low-bandwidth behaviour while estimating full-bandwidth dynamics. In *Rehabilitation Robotics, 2007. ICORR 2007. IEEE 10th International Conference on*, pages 575–581. IEEE.
- Papalambros, P. and Wilde, D. (2000). *Principles of optimal design: modeling and computation*. Cambridge Univ Pr.
- Schwab, A. L., Kooijman, J. D. G., and Meijaard, J. P. (2008). Some recent developments in bicycle dynamics and control. In Belyaev, A. K. and Indeitsev, D. A., editors, *Fourth European Conference on Structural Control (4ECSC)*, pages 695–702. Institute of Problems in Mechanical Engineering, Russian Academy of Sciences.
- Schwab, A. L., Meijaard, J. P., and Kooijman, J. D. (2011). Lateral dynamics of a bicycle with a passive rider model: stability and controllability. *Vehicle System Dynamics*.
- Skogestad, S. and Postlethwaite, I. (2005). *Multivariable feedback control analysis and design*. New York.
- Stassen, H. G. and Lunteren, A. v. (1973). Progress report january 1970 until january 1973 of the man-machine systems group. Technical report, Technische Hogeschool Delft.
- van den Ouden, J. (2011). Inventory of bicycle motion for the design of a bicycle simulator. Master’s thesis, TU Delft.
- van der Kooij, H., Jacobs, R., Koopman, B., and Grootenboer, H. (1999). A multisensory integration model of human stance control. *Biological cybernetics*, 80(5):299–308.
- van der Kooij, H., Jacobs, R., Koopman, B., and van der Helm, F. (2001). An adaptive model of sensory integration in a dynamic environment applied to human stance control. *Biological Cybernetics*, 84(2):103–115.

- van Lunteren, A. and Stassen, H. G. (1970). Investigations on the bicycle simulator, chapter iii of annual report 1969 of the man-machine systems group. Annual report 1969 of the man-machine systems group WTHD21, Delft University of Technology, Laboratory for Measurement and Control.
- Weir, D. H. (1972). *Motorcycle Handling Dynamics and Rider Control and the Effect of Design Configuration on Response and Performance*. PhD thesis, University of California, LA.
- Whipple, F. J. W. (1899). The stability of the motion of a bicycle. *Quarterly Journal of Pure and Applied Mathematics*, 30:312–348.
- Yeadon, M. and Morlock, M. (1989). The appropriate use of regression equations for the estimation of segmental inertia parameters. *Journal of Biomechanics*, 22(6-7):683–689.

